Elucidating the role of the InGaN UL in the efficiency of InGaN based light-emitting diodes

Thèse N° 9455

Présentée le 1^er^ novembre 2019

à la Faculté des sciences de base
Laboratoire en semiconducteurs avancés pour la photonique et l’électronique
Programme doctoral en photonique

pour l’obtention du grade de Docteur ès Sciences

par

Camille HALLER

Acceptée sur proposition du jury

Prof. U. A. Hagfeldt, président du jury
Prof. N. Grandjean, directeur de thèse
Dr A. Avramescu, rapporteur
Prof. H. Amano , rapporteur
Prof. A. Fontcuberta i Morral, rapporteuse

2019

ÉCOLE POLYTECHNIQUE
FÉDÉRALE DE LAUSANNE

A scientist in his laboratory is not only a technician:
he is also a child confronting natural phenomena
that impress him as though they were fairy tales.
— Marie Curie

To my husband…

Acknowledgements

A Ph. D work cannot be done alone, and it will be hard to thanks every one how helped me during these past years. First, I would like to thanks my director Professor Nicolas Grandjean for offering me the opportunity to work in his lab. He guided my thesis work and shared his enthusiasm for physics and unsolved problems, which was a great motivation source. I will not have managed this work without the help of my "unofficial" co-director, Jean-François Carlin. MOVPE has no secrets for him, and I am grateful for all the nice and useful discussions we had. I would also thank Prof. Anders Ulf Hagfeldt, Prof. Anna Fontcuberta i Morral, Prof. Hiroshi Amano, and Dr. Adrian Avramescu, who accepted to review this work.
I would like to thanks Dr. Raphaël Butté for his support and his patience with the correction of the papers and the thesis, Dr. Gwénolé Jacopin and Wei Liu for the TRPL measurements, Dr. Gordon Callsen, which show me how to do consistent PL measurements, Denis Martin, which introduce me to MOVPE growth, and Damien Trolliet for the help with the MOVPE technical issues. The ambiance in the lab helps a lot, especially when things were not working. For all the coffee break and the pleasant evening, I want to thanks Sebastian, Pirouz, Ian, Wei, Joachim, Thomas, Yao, Annina, Danxuan, Kanako, Hezhi, Marco, and Gordon.
I also want to say a special thanks to my parents, my sister and my brother how always believed in me. Finally, I will never have managed this work without the support of my husband, Antoine, how has been on my side every day, especially during these last nine months. I also want to say thank you to the little one which was always with me during the thesis writing and has patiently waited for the right moment.

This thesis was supported by the CTI-KTI Project “High power GaN-lasers for white light generation” 17519.1 PFEN-NM.

Lausanne, 30 Mai 2019

C. H.

Abstract

Blue III-nitride light-emitting diodes (LEDs) are widely used nowadays in solid-state lighting, as white light can be produced by combining yellow phosphors and blue LEDs. This technology has the advantage to have a higher luminous efficiency than incandescent light bulbs and fluorescent tubes. This high efficiency is attributed to InGaN quantum wells (QWs), which exhibit an internal quantum efficiency (IQE) higher than 90 % at 300 K. However, even if blue LEDs are industrially produced, the high IQE of InGaN QWs is still barely understood.

In InGaN/GaN-based LEDs, an InGaN layer grown before the InGaN/GaN QW is often found. This InGaN layer named an underlayer (UL) is used in all commercial devices and is known to increase drastically the efficiency of LEDs. However, the physical mechanism behind the efficiency improvement is debated in the literature.

In the first part of this work, a study of the different existing hypotheses proposed is conducted. The conclusion is that the role of the InGaN UL is to capture point defects before they reach the InGaN QWs. Indeed, points defects react with InGaN and are transformed into non-radiative centers when they are buried in the InGaN alloy. We call such point defects reacting with indium "surface defects" (SDs).

To explore the SD capture by the InGaN UL, we studied different kinds of UL: InGaN UL, InAlN UL, and low-temperature GaN UL. We found that indium atoms play a key role in the capture of SDs. Indeed, the number of SDs buried in the UL depends on its thickness and indium composition. As a consequence, GaN layers are not able to bury SDs as efficiently. A model based on segregation of SDs was proposed based on our observations. As InGaN UL are present in all LEDs, we concluded that SDs are problematic for all LEDs independently of the type of reactor. The growth temperature of GaN was identified as the parameter which generates SDs. Indeed, for temperatures higher than 820 °C in MOVPE, SDs are created. Different impurities were searched by secondary ion mass spectrometry measurements, but no correlation was found between the sample efficiency and the impurity concentration. Our hypothesis is that the stability of the GaN surface is affected by the temperature and therefore leads to the formation of SDs, which could be intrinsic defects such as nitrogen vacancies. However, we do not have any experimental proof about the actual nature of SDs yet.

In the last part of this work, near UV LEDs with InAlN UL were designed and characterized. Single QW (SQW) LEDs emitting around 405 nm with an InAlN/GaN superlattice UL exhibit an IQE around ~70 %, which is higher than for a SQW LED without UL (~10 %). The I-V characteristic is similar for both samples thanks to a highly doped region placed at the interface between the InAlN/GaN superlattice UL and the GaN spacer.

Résumé

Les LED bleues fabriquées à partir de nitrures d'élements III sont largement utilisées de nos jours, car elles permettent de produire de la lumière blanche en les combinant avec un luminophore jaune. Cette technologie présente l'avantage d'avoir un rendement lumineux supérieur à celui des ampoules à incandescence et des tubes fluorescents. Cette haute efficacité est attribuée aux puits quantiques InGaN qui présentent un rendement quantique interne supérieur à 90 %. Cependant, même si les LED bleues sont produites industriellement depuis de nombeuses années, l'efficacité élevée des puits quantiques InGaN n'est encore que partiellement comprise.

Dans la plupart des structures LED commerciales basées sur les puits quantiques InGaN / GaN, une sous-couche d'InGaN est déposée avant le puits quantique. Cette sous-couche est connue depuis longtemps pour augmenter considérablement l'efficacité des LED. Le mécanisme physique derrière cette augmentation est encore débattu dans la littérature. Dans la première partie de cette thèse, une étude des différentes hypothèses proposées a été conduite. Nous en avons conclu que le rôle de la sous-couche d'InGaN est de capturer des défauts ponctuels avant qu'ils atteignent les puits quantiques InGaN. En effet, les défauts ponctuels réagissent avec l'InGaN et deviennent des centres de recombinaison non-radiatifs lorsqu'ils sont incorporés dans l'alliage InGaN. Nous avons choisi d'appeler ces défauts ponctuels qui réagissent spécifiquement avec l'indium : défauts de surface (DS).

Pour explorer la capture des DS par la sous-couche d'InGaN, nous avons étudié différents types de sous-couches à base d'InGaN, d'InAlN et de GaN que nous avons crues à basse température. Nous constatons que les atomes d'indium jouent un rôle clé dans la capture des DS. Le nombre de DS enterrés dans la sous-couche dépend de son épaisseur et de sa composition en indium. Par conséquent, les couches dépourvues d'indium ne peuvent pas enterrer les DS de manière efficace. Un modèle basé sur la ségrégation des DS est proposé à partir de nos observations.

Les sous-couches d'InGaN étant largement utilisées dans l'industrie, nous pouvons supposer que les DS ne dépendent pas du type de réacteur utilisé pour la fabrication des LEDs. En effet, nous n'avons pas pu lier leur provenance aux précurseurs organo-métalliques ou aux différents gaz porteurs utilisés dans nos réacteurs. La température de croissance du GaN s'avère être un paramètre critique pour la génération des DS. Il faut qu'elle soit supérieure à 820°C pour les créer dans le cas de la MOVPE. Différentes impuretés ont ensuite été recherchées par spectrométrie de masse d'ions secondaires, mais aucune corrélation n'a été trouvée entre l'efficacité du puits quantique et la concentration d'impuretés. Nous en concluons que la stabilité

de la surface de GaN est affectée par la température et génère des DS à haute temperature qui pourraient être des défauts intrinsèques tels que des lacunes d'azote. Nous n'avons cependant pas pu le démontrer expérimentalement.
Dans la dernière partie de ce travail, des LED dans l'UV proche basée sur des sous-couches InAlN ont été conçues et caracterisées. Ces LED à puits quantique unique incorporent un super-réseau InAlN/GaN et présentent une efficacité quantique interne élevée de ~70% , ce qui est largement supérieur à l'efficacité quantique interne d'une LED sans sous-couche (~10%). De plus, en ajoutant une région de dopage élevé placée à l'interface entre le super réseau InAlN/GaN et le GaN, les caractéristiques I-V demeurent excellentes.

List of acronyms

CW	continuous wave
EL	electroluminescence
HRXRD	high-resolution x-ray diffraction
HT	high temperature
LM	lattice-matched
LT	low temperature
MOVPE	metalorganic vapor phase epitaxy
MBE	molecular beam epitaxy
MQW	multiple quantum well
ML	monolayer
NR	non radiative
NRC	non radiative center
PL	photoluminescence
UL	underlayer
QCSE	quantum confined Stark effect
QW	quantum well
SD	surface defect
SL	superlattice
SQW	single quantum well
SRH	Shockley-Read-Hall

TEGa	triethylgallium
TMAl	trimethylaluminum
TMIn	trimethylindium
TMGa	trimethylgallium
TRPL	time-resolved photoluminescence
YB	yellow band

Contents

Acknowledgements **v**

Abstract (English/Français) **vii**

List of acronyms **xi**

Introduction **1**

1 III-nitrides and experimental techniques **5**

1.1 Structural properties 5

1.1.1 Crystal structure 5

1.1.2 Polarization 7

1.2 Optical properties 8

1.2.1 Bandgap 8

1.2.2 InGaN/GaN quantum wells 10

1.3 Light-emitting diodes 14

1.3.1 The *p*-*n* junction 14

1.3.2 ABC model 16

1.3.3 Shockley-Read-Hall recombination 17

1.4 Experimental techniques 18

1.4.1 Growth 19

1.4.2 Photoluminescence 21

1.4.3 Electroluminescence 22

2 Role of the InGaN underlayer **25**

2.1 Introduction 26

2.2 Injection efficiency 27

2.3 Threading dislocation 29

2.4 Formation of V-pits 31

2.5 Impact on the step edge morphology 32

2.6 Reduction of the electric field 33

2.7 Strain management 35

2.8 Reducing the density of non radiative centers 37

3 Capture of surface defects by indium 41
3.1 Experimental evidence of the capture mechanism 41
3.1.1 InGaN underlayer thickness 42
3.1.2 InGaN underlayer composition 45
3.1.3 Low temperature GaN underlayer 47
3.1.4 InAlN underlayer 48
3.2 Modeling of the interaction of surface defects with In atoms 49
3.3 Discussion on the role of multiple quantum wells 53

4 Creation and nature of the surface defects 57
4.1 Creation of surface defects 57
4.1.1 Metalorganic precursors and carrier gases 58
4.1.2 Temperature 61
4.2 Nature of the surface defects 66
4.2.1 Impurities 66
4.2.2 Intrinsic defects 70
4.3 Surface defect density 73

5 Devices: InAlN underlayer for near ultraviolet light-emitting diodes 77
5.1 InAlN material 77
5.2 InAlN bulk underlayer 78
5.2.1 LED structures and properties 78
5.2.2 Doping at the interface 80
5.3 InAlN/GaN superlattice underlayer 81
5.4 EQE vs IQE 84

Conclusion 86

A Additional experiments 89
A.1 Effect of the InGaN UL on InGaN/AlGaN QWs 89
A.2 Effect of the InGaN UL on GaN/AlGaN QWs 90
A.3 Effect of growth interruption on the creation of SDs 91
A.4 Effective lifetime behavior with temperature 92

B Structure and sample name 95

Bibliography 111

Curriculum Vitae 113

Introduction

Since the beginning of civilization, human beings have always searched for an efficient way to get light in the night, with fire first, then with candles and oil lamps. When electricity was discovered, the idea emerged that we might use its power to provide light instead of using combustion. In 1880, Thomas Edison deposited a patent on the incandescent light bulb and how to produce it in an industrial way [1]. During the 20^{th} century, new developments came up with gas discharge lamps (fluorescent light sources) with luminous efficacy approaching 100 lm/W, which is far better than the efficiency of incandescent light bulbs (15 lm/W) [2]. At the beginning of the 20^{th} century, higher luminous efficacy was reached thanks to III-nitride white light-emitting diodes (LEDs), which consist of a high-efficiency blue LED covered by a yellow phosphor [3].

Blue LEDs are based on III-nitride semiconductor materials (AlN, GaN, InN and their alloy). There were several challenges to overcome before the realization of a highly efficient III-nitride LED. The first one was the lack of native substrate, which results in poor material quality. A breakthrough was reported by Amano *et al.* in 1986 with a technique to grow GaN on a sapphire substrate by metalorganic vapor phase epitaxy (MOVPE) [4]. Before the growth of the GaN buffer, a thin layer of AlN was deposited directly on the sapphire substrate. This nucleation layer promotes the 3D growth and a GaN layer with good crystalline and optical quality was achieved for the first time.

The second challenge for the fabrication of the LED itself was to find a suitable acceptor for obtaining *p*-type material. Mg was proposed as an impurity as it can be introduced in GaN. However, Mg was not acting as a dopant. Amano *et al.* showed that GaN layers doped with Mg can be activated if the layer is irradiated by an electron beam [5]. In 1992, Nakamura *et al.* demonstrated that GaN doped with Mg can be activated by thermal annealing [6], which makes *p*-type doping easily accessible. This opened promising perspectives for mass production of III-nitride devices. Two years later, blue candela class LEDs were fabricated by the Japanese manufacturer, Nichia Inc. [7]. They also developed the first commercial blue laser diodes [8].

III-nitride based white LEDs are now present everywhere as they have the big advantage to be more efficient than fluorescent tubes and incandescent lamps. Indeed, III-nitride-based LEDs can exhibit a peak luminous efficiency exceeding 300 lm/W [9]. To reach this impressive value, several key points were optimized: the injection efficiency, the extraction efficiency, and the IQE. The injection of carriers in the active region of an LED can be problematic as holes have a lower mobility than electrons. To improve the injection in the active regions, an electron blocking layer on the *p*-side of the junction is introduced to force the electrons to stay in the active region and recombine with the holes. When emitted by a semiconductor, light is often guided in the material due to the difference of refractive index between the air and the semiconductor. Therefore the extraction can be improved with different techniques such as the shape of the LED or the roughening of the surface [10]. Finally, the last part which was optimized is the IQE. It is governed by the active region of the LEDs which is made of InGaN/GaN QWs.

Nowadays, InGaN/GaN QWs exhibit a high IQE, which can exceed 90 % [11]. This high efficiency is often achieved thanks to a layer placed on the *n*-type side of the LED structure. This layer is made of InGaN and is called "underlayer" (UL). InGaN ULs can be found in all III-nitride LEDs emitting in the visible, even in LEDs produced by manufacturers [12]. However, despite the massive adoption of the InGaN UL, the physical mechanisms behind this layer are still unclear.

The objective of this thesis is to understand the role of the InGaN UL in blue LEDs. This work is organized as follows:

- **Chapter 1: III-nitrides and experimental techniques** We introduce the main properties of III-nitrides with a focus on their optical features. The role of the Shockley-Read-Hall recombination in LEDs is discussed. A presentation of the different experimental techniques used in this work is also given.
- **Chapter 2: Role of the InGaN underlayer** The different hypotheses present in the literature on the role of the InGaN UL are carefully reviewed. We carry out a series of MOVPE growths and different measurements to study each of the hypotheses. Finally, we conclude that the InGaN UL buries surface defects (SDs) before they reach the QWs, where they create non-radiative centers (NRCs).
- **Chapter 3: Capture of surface defects by indium** We perform a systematic study of In-containing ULs. Their thickness and composition are explored to understand how the UL captures SDs, reducing thereby the number of NRCs in the QW active region.
- **Chapter 4: Creation and nature of surface defects** SDs are present in all samples whatever the type of reactor and growth technique. We first study how they are created. This is done by changing the growth conditions in a GaN spacer located between the InGaN UL and the InGaN QW. In the second part, a discussion is opened on the nature of those SDs, which can be either impurities or intrinsic defects.
- **Chapter 5: Devices: InAlN underlayer for near ultraviolet light emitting diodes** Knowing that any indium-containing layer could act as an UL, LEDs with an InAlN UL were grown. We discuss how to improve the overall characteristics of the devices by intro-

ducing an InAlN/GaN superlattice and a high doping region at the last InAlN/GaN interface.

Finally, we conclude this work and present some perspectives.

The results of this thesis were partially published in:
C. Haller, J.-F. Carlin, G. Jacopin, D. Martin, R. Butté, and N. Grandjean, "Burying non-radiative defects in InGaN underlayer to increase InGaN/GaN quantum well efficiency", Appl. Phys. Lett. **111**, 262101 (2017).
C. Haller, J.-F. Carlin, G. Jacopin, W. Liu, D. Martin, R. Butté, and N. Grandjean, "GaN surface as the source of non-radiative defects in InGaN/GaN quantum wells", Appl. Phys. Lett. **113**, 111106 (2018).
C. Haller, J.-F. Carlin, M. Mosca, M. D. Rossell, R. Erni, and N. Grandjean, "InAlN underlayer for near ultraviolet InGaN based light emitting diodes", Appl. Phys. Express **12**, 034002 (2019).

1 III-nitrides and experimental techniques

In this chapter, an overview of the properties of III-nitride semiconductors is given. Structural and optical properties will be discussed first with a focus on InGaN material. We will then speak about one of the main applications of nitrides which are LEDs. In the second part, the experimental techniques used in this work will be described.

1.1 Structural properties

1.1.1 Crystal structure

III-nitride materials are composed of three binary compounds: AlN, GaN, InN. From them, their ternary alloys ($In_xGa_{1-x}N$, $Al_xGa_{1-x}N$, $In_xAl_{1-x}N$) and quaternary alloy ($Al_xIn_yGa_{1-x-y}N$) can be synthesized. Two crystal structures are possible for these materials: the zincblende structure or the wurtzite structure. These two structures can be obtained with III-nitrides depending on the growth conditions. However, the zincblende phase is metastable and will tend, during the growth, to change to the more stable wurtzite phase [13]. For III-nitrides, the common crystal structure is, therefore, the wurtzite one which presents a direct band-gap. This is important to highlight, as it is the contrary for other common semiconductor materials such as GaSb, GaAs or GaP whose stable phase is the zincblende one. Notice that all the samples in this work possess the wurtzite structure.

The wurtzite structure is made of two hexagonal close-packed structures (one for the anion (N) and one for the cation (Al, Ga, In)) which are shifted from each other by a fraction u of the c parameter. This shift lies along the c-axis, i.e., the [0001] direction, see Fig. 1.1. The a lattice parameter is the distance between two cations in the c plane, see Fig. 1.1. The fraction, u, represents the length of the bond between the anion and the cation along the c-axis. It will depend on the difference in electronegativity for each anion-cation pair. AlN, GaN, and InN lattice parameters are displayed in Tab. 1.1. When the wurtzite structure is ideal, the ratio c/a should be equal to $\sqrt{8/3} = 1.633$, and hence u should be equal to 0.375. However, as displayed in Tab. 1.1, we can see that the u parameter is not ideal for all the III-nitrides, especially for

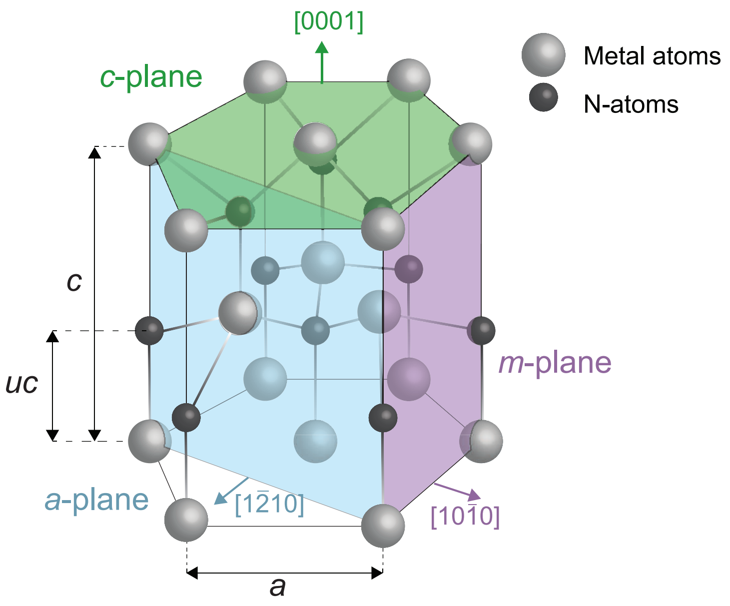

Figure 1.1 – Schematic view of the wurtzite unit cell. The metal atoms can be Al, Ga or In. The different planes are indicated in color. The *c*-plane is indicated in green, which is the polar plane. The *a*-plane and *m*-plane, which are the non-polar planes, are indicated in blue and violet, respectively.

	AlN	GaN	InN
c (Å)	4.982	5.185	5.703
a (Å)	3.112	3.189	3.545
u	0.3814	0.3769	0.3787

Table 1.1 – Lattice parameters for each III-nitride binary compounds. All parameters are taken from Ref. [14].

AlN. As the difference in electronegativity between each couple of atoms is large, the atomic layers tend to attract each other and to deviate from the ideal case ($u = 0.375$). For ternary alloys, the crystal structure remains the same, but the lattice parameters will change. They can be computed using Vegard's law, which will give the new lattice parameters. Therefore, the Vegard's law for a lattice constant t of a ternary alloy, $A_xB_{1-x}N$, is given by :

$$t_{A_xB_{1-x}N} = x \cdot t_{AN} + (1-x) \cdot t_{BN}, \tag{1.1}$$

with x the composition of the A material.

III-nitrides are usually grown by MOVPE or MBE. During the growth, several layers of different materials are deposited on top of each other (heteroepitaxy). Most of the time, we are in a regime where the growth is pseudomorphic, the lattice parameter of the top layer will adapt

Binary compound	AlN	GaN	InN
P_{sp} (C/m^2)	-0.090	-0.034	-0.042
Ternary alloy	InGaN	AlGaN	InAlN
b (C/m^2)	0.037	0.021	0.070

Table 1.2 – Spontaneous polarization for each III-N binary compound and bowing parameter for each ternary alloy. All the values are taken from Ref. [16].

its lattice parameter to the one of the previous layers. The basal strain is given by:

$$\epsilon = \frac{a_s - a_l}{a_l}, \tag{1.2}$$

with a_s the lattice parameter of the substrate and a_l the lattice parameter of a given layer. The layer can be either lattice-matched ($\epsilon = 0$), in compressive strain state ($\epsilon < 0$), or in tensile strain state ($\epsilon > 0$). During pseudomorphic growth, the lattice is deformed, leading to some interesting new properties such as piezoelectric polarization, which will be discussed in the next section.

1.1.2 Polarization

Spontaneous polarization

The wurtzite structure possesses a lack of inversion symmetry which creates a strong dipole moment along the c-axis. It builds an internal polarization even when the crystal is not under any stress, which is called the spontaneous polarization ($\mathbf{P}^{\text{sp}}$) [15]. The orientation of the spontaneous polarization is also along the c-axis. For each binary material, $\mathbf{P}^{\text{sp}}$ will have a different value, see Tab. 1.2. In the case of ternary alloys, the spontaneous polarization can be written using a modified Vegard's law [14]:

$$\mathbf{P}^{\text{sp}}_{\text{A}_x\text{B}_{1-x}\text{N}} = x \cdot \mathbf{P}^{\text{sp}}_{\text{AN}} + (1-x) \cdot \mathbf{P}^{\text{sp}}_{\text{BN}} - \mathbf{b}_{\text{A,B}} x(1-x), \tag{1.3}$$

with x the fraction of the A material, and $b_{\text{A,B}}$ the polarization bowing parameter for the different alloys expressed in C/m^2, which can be found in Tab. 1.2.

Piezoelectric polarization

For devices such as LEDs, different materials are grown on top of each other which induces strain in the layers. Typically, for an InGaN/GaN QW grown on a GaN on sapphire template, the InGaN layer experiences compressive strain. The strain changes the lattice parameter, thus influencing the polarization. This effect is called the piezoelectric polarization and can be written for the different binaries as [17]:

$$\begin{aligned}
P^{\mathrm{pz}}_{\mathrm{AlN}} &= -1.808\epsilon + 5.624\epsilon^2, \text{ for } \epsilon < 0\\
P^{\mathrm{pz}}_{\mathrm{AlN}} &= -1.808\epsilon - 7.888\epsilon^2, \text{ for } \epsilon > 0\\
P^{\mathrm{pz}}_{\mathrm{GaN}} &= -0.918\epsilon + 9.541\epsilon^2\\
P^{\mathrm{pz}}_{\mathrm{InN}} &= -1.373\epsilon + 7.559\epsilon^2
\end{aligned} \tag{1.4}$$

with ϵ the basal strain. For alloys, Vegard's law can be applied to compute the piezoelectric polarization:

$$P^{\mathrm{pz}}_{\mathrm{A}_x\mathrm{B}_{1-x}\mathrm{N}} = x \cdot P^{\mathrm{pz}}_{\mathrm{AN}}(\epsilon(x)) + (1-x) \cdot P^{\mathrm{pz}}_{\mathrm{BN}}(\epsilon(x)), \tag{1.5}$$

with $\epsilon(x)$ which depends on the lattice constant of the studied layer, which can be found with Eq. (1.1).

Finally, the total polarization can be written as:

$$\mathbf{P} = \mathbf{P}^{\mathrm{sp}} + \mathbf{P}^{\mathrm{pz}}. \tag{1.6}$$

This equation will play an important role when we will discuss the properties of InGaN/GaN QWs in Sec. 1.2.2.

1.2 Optical properties

In this part, we will discuss the optical properties and specificities of III-nitride materials. QWs in III-nitrides will be addressed by focusing on the case of *c*-plane grown InGaN/GaN QWs as it is the main subject of this study.

1.2.1 Bandgap

As mentioned, III-nitrides have a direct bandgap, which makes them particularly suitable for the realization of optoelectronic devices. In Fig. 1.2(a), the band structure around the Γ-point is displayed. A particularity of III-nitrides is their wide bandgap range, which spans from the IR with the bandgap of InN, 0.64 eV, to the deep UV with the bandgap of AlN, 6.0 eV. The bandgap of GaN lies in between with a gap around 3.44 eV. The different bandgaps are taken from Ref. [18–22] and are the band to band values expected at 300 K (Tab. 1.3). The large spectral range accessible and the direct bandgap of III-nitrides makes them particularly suitable to enter in the fabrication of visible emitters.

The bandgap of different alloys (InAlN, InGaN, and AlGaN) can be computed by using a modified Vegard's law:

$$E_g(\mathrm{A}_x\mathrm{B}_{1-x}\mathrm{N}) = x \cdot E_g(\mathrm{AN}) + (1-x) \cdot E_g(\mathrm{BN}) - x(1-x)b_{\mathrm{A,B}}, \tag{1.7}$$

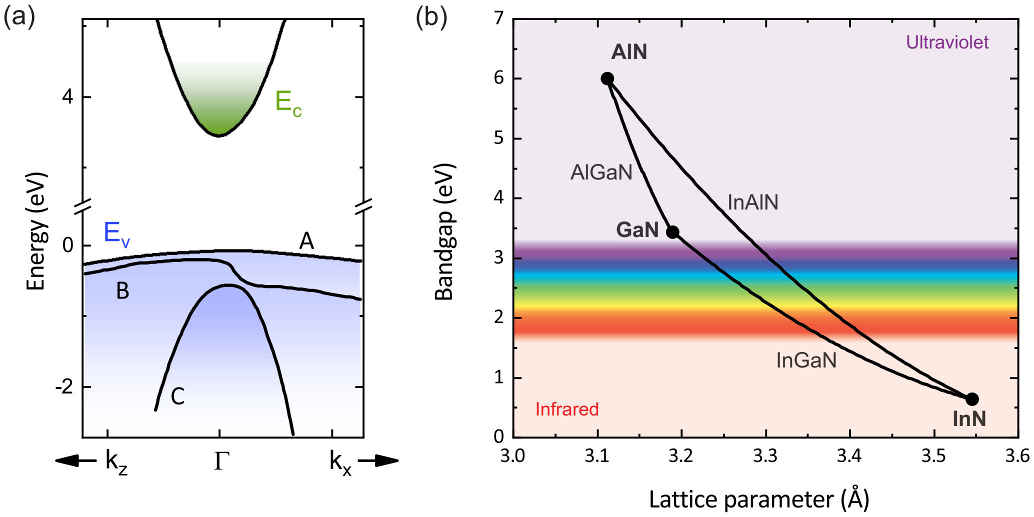

Figure 1.2 – (a) Band structure around the Γ-point for GaN, which is representative of all the III-nitrides. Courtesy of S. Tamariz. (a) Bandgap of III-nitride materials at 300 K as a function of the in-plane lattice parameter. The visible range is shown by a "rainbow".

with x the fraction of the AN material, and $b_{\mathrm{A,B}}$ the bandgap bowing parameter for the different alloys in eV. Fig. 1.2(b) shows the bandgap evolution for the different alloys as a function of the in-plane lattice parameter a. The values used for the bowing in Fig. 1.2(b) are taken from Ref. [22]. Notice that the bowing parameter values vary a lot in the literature. III-nitrides should be able to cover the near IR to deep UV spectral range. However, due to some limitations, the visible range beyond the green is difficult to access. Indeed, the InGaN alloy with a composition exceeding 25% can not be grown pseudomorphically sparing[23]. On the other hand, deep UV emitters are also difficult to achieve due to the large AlN bandgap, which makes electrical conductivity, especially p-type , difficult to achieve. The main optoelectronic applications of III-nitrides are blue to green LEDs, and LDs, which are made of the InGaN alloy with an indium content typically ranging between 6 and 25%.

The bandgap changes with the temperature (T) and can be described by a simple empirical formula (Varshni law) [24]:

$$E_g(T) = E_g(0\ \mathrm{K}) - \frac{\alpha T^2}{T+\beta} \tag{1.8}$$

with $E_g(0\ \mathrm{K})$ the bandgap at 0 K (Tab. 1.3), and α and β some fitting parameters, which should be found for each sample as they are strongly dependent on the material state (strain, quality, etc.). For example, in the case of GaN, these parameters are equal to $\alpha = 0.887$ meV/K and $\beta = 874$ K, according to Ref. [21].

	$E_g(\sim 0\ \mathrm{K})$ [eV]	$E_g(300\ \mathrm{K})$ [eV]	α [meV/K]	β [K]
AlN	6.09 [19]	6.00	1.799 [22]	1462 [22]
InN	0.69 [18]	0.64	0.414 [18]	454 [18]
GaN	3.51 [20]	3.44	0.887 [21]	874 [21]

Table 1.3 – Band to band bandgap values for the different binary compounds and their Varshni coefficients.

1.2.2 InGaN/GaN quantum wells

Spatial confinement can be obtained easily by adding a material with a small band gap surrounded by a material with a larger bandgap. Quantum confinement appears when the de Broglie wavelength of the carriers, ($\lambda_{DB} = \frac{2\pi\hbar}{\sqrt{2m_e E}}$ with $\hbar$, the reduced Planck constant, m_e the carrier mass, E the carrier energy)[25], is larger than the energy potential variation distance experienced by carriers. In this case, discrete energy levels appears which can be tuned depending on the design of the heterostructure. Quantum confinement can be done on one or all the three dimension of space. Therefore, three types of heterostructure exist: QWs (1D), quantum wires (2D), and quantum dots (3D).

In this work, we will focus only on QWs where the quantum confinement occurs only along the growth axis direction. They are made of a layer with a small bandgap (for example $In_{0.12}Ga_{0.88}N$) sandwiched between two layers with a larger bandgap (for example GaN). If the width of the InGaN layer is sufficiently thin, the allowed energies for the carriers are discrete energy levels instead of a continuum of energy states. For QWs with infinite barriers, the position of quantized energy levels is given by $E_j = \frac{\hbar(j\pi/d)^2}{2m}$, with $j = 1,2,3,...$, d the well thickness, and m the carrier mass.

To get light out of semiconductor materials, a hole and an electron need to radiatively recombine. The probability of getting radiative recombination, i.e., a photon, is related to by the oscillator strength [25]:

$$f_{\mathrm{osc}} \propto \left|\langle\phi_e|r\rangle\langle r|\phi_h\rangle\right|^2 \tag{1.9}$$

with r the position vector, and $\phi_{h,e}$ the wave-function of the hole or the electron. Therefore, the confinement in one direction will increase the oscillator strength, as the overlap between the hole wave-function ϕ_h and the electron wave-function, ϕ_e, will increase, leading to enhance radiative recombination. For this reason, in most optoelectronic devices, the active region, which is the part producing the photons, features QWs.

In the case of III-nitride LEDs or LDs, the active region for the visible range is made of GaN barriers with InGaN MQWs or $In_yGa_{1-y}N$ barriers with $In_xGa_{1-x}N$ MQWs ($y < x$). The QWs used in this work are InGaN/GaN QWs, which are commonly used in blue LEDs.

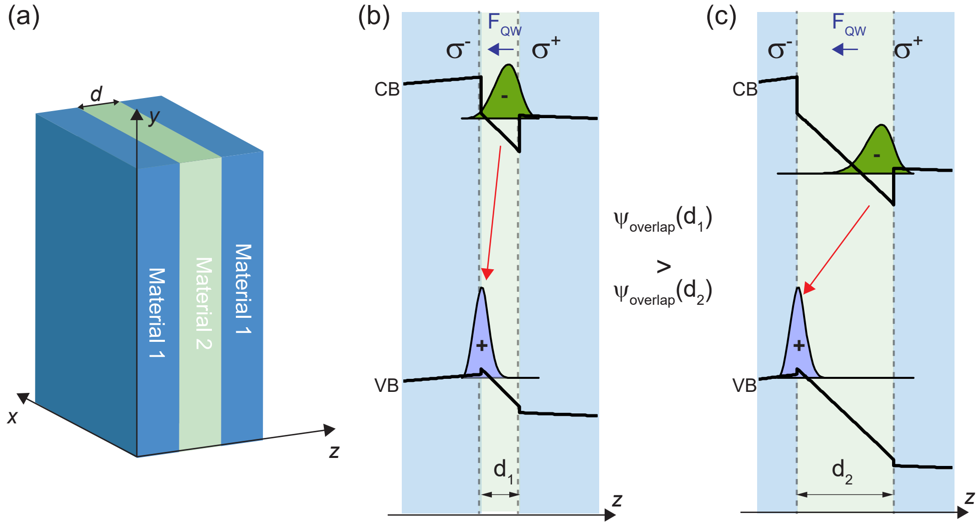

Figure 1.3 – (a) Schematic view of a triangular QW. During the growth, layers of different materials are deposited. The growth axis is the z axis by convention. The two material have a different bandgap ($E_{g,1}$ and $E_{g,2}$). (b) For a thin QW, the two wave-functions are strongly overlapping, left. (c) For a thicker QW, the two wave-functions are confined on opposite sides, which will diminish their overlap. The two charge planes, σ^- and σ^+, are indicated by the grey dashed lines.

Quantum confined Stark effect

As mentioned in section 1.1.2, III-N materials have a macroscopic polarization vector, **P**, see Eq. (1.6). When layers of different materials are grown next to each other, a discontinuity of the polarization occurs at the interface, generating a sheet of charge density, σ, due to the polarization mismatch given by Gauss law. In a QW, sheet charge density planes of opposite sign appear at the two interfaces (σ^- and σ^+), see Fig. 1.3. These two planes of charges create a field inside the QW [14, 26]:

$$\mathbf{F}_{\mathrm{QW}} = \frac{\sigma_P}{\varepsilon_w}\mathbf{n}, \text{ with } \sigma_P = -\Delta\mathbf{P}\cdot\mathbf{n}, \tag{1.10}$$

with **n**, the unit vector perpendicular to the growth interface, $\varepsilon_w = \varepsilon_0 \cdot \varepsilon_r$, the product of the vacuum and QW relative permittivities, $\Delta\mathbf{P}$ the difference of polarization between the two materials. If we develop the term $\Delta\mathbf{P}$ using Eq. (1.6), we obtain:

$$\Delta\mathbf{P} = \mathbf{P}^{\mathrm{sp}}_{\mathrm{B}} - (\mathbf{P}^{\mathrm{sp}}_{\mathrm{QW}} + \mathbf{P}^{\mathrm{pz}}_{\mathrm{QW}}), \tag{1.11}$$

with $\mathbf{P}^{\mathrm{sp}}$ the spontaneous polarization of the barrier, B, or of the QW, and $\mathbf{P}^{\mathrm{pz}}_{\mathrm{QW}}$ the piezoelectric polarization of the QW. Here, we assume the standard situation where the barriers are unstrained, i.e., the piezoelectric polarization of the barrier is 0. In III-nitrides, the value of these built-in fields depending on the layers composition and the materials is rather high. For InGaN/GaN QWs and for GaN/AlGaN QWs, it can be around a few MV/cm [27–29].

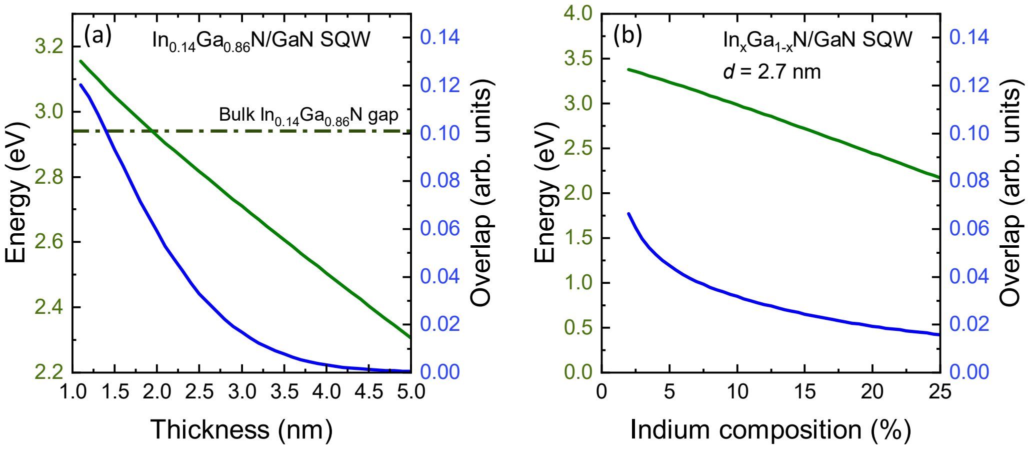

Figure 1.4 – Emission energy and overlap between the hole and the electron wave-functions as a function of QW thickness (a), and as a function of indium composition (b). To compute those parameters, simulations with the help of the commercial software NextNano are realized.

The built-in field F_{QW} in the QW will bend the band structure leading to a triangular shape instead of the conventional rectangular shape, see Fig. 1.3. The triangular shape of the QW modifies the confinement of the carriers, and the transition energy can be written as [14]:

$$E_{e_1-hh_1} = E_{g,\mathrm{QW}} + e_1 + hh_1 - E_B - eF_{\mathrm{QW}} l_{\mathrm{QW}}, \tag{1.12}$$

with $E_{g,\mathrm{QW}}$, the QW bandgap, e_1 the electron confinement energy, hh_1 the hole confinement energy, E_B the exciton binding energy[1], e the elementary charge, l_{QW} the width of the QW, and F_{QW} the norm of the internal electric field. The influence of the built-in field on the QW transition energy is called the quantum confined stark effect (QCSE).

The QCSE will change the emission energy of the QW for a given composition as a function of the QW thickness l_{QW}, see Fig. 1.4(a). Thanks to the QCSE, a broad range of energies can be covered depending on the QW thickness. For thick QWs, emission below the bandgap of the bulk material is accessible, which can be an advantage. Indeed, the indium composition being limited to 25% for pseudomorphic layers [23], the minimum bulk bandgap is around 2.54 eV (490 nm) , which is not in the green range. Thanks to the QCSE, it is therefore possible to have QWs emitting between 510 and 550 nm (2.43-2.25 eV) [30–32]. Contrary to a common belief, the built-in field has a positive effect for the realization of long wavelength devices.

On the other hand, the built-in field separates the electron and the hole wave-functions, see Fig. 1.3. As the overlap between the two wave-functions reduces, the oscillator strength decreases, leading to a longer radiative lifetime (i.e., a smaller radiative efficiency). In Fig. 1.4(a), the overlap for an $\mathrm{In_{0.14}Ga_{0.86}N/GaN}$ SQW is displayed as a function of QW thickness. Even if it is possible to reach the green spectral range (2.2 eV) with an $\mathrm{In_{0.14}Ga_{0.86}N/GaN}$ SQW, simulations predict a very small overlap, i.e., a QW with poor internal quantum efficiency.

---

[1] The calculations realized will not take into account the binding energy.

Another parameter we can modify is the material inside the QW. By changing the material, the polarization difference between the barriers and the QW will change, thus impacting F_{QW}. In InGaN/GaN QWs, this phenomenon is dominated by the strain difference, i.e., the In content. For a 2.7 nm thick InGaN/GaN QW, we plot the evolution of the emission energy as a function of indium composition, see Fig. 1.4(b). The wave-function overlap is also reported. When the indium content increases, the emission energy decreases, which is expected both from the bulk InGaN bandgap reduction and the increase of the QCSE. Simultaneously, the wave-function overlap also decreases due to the strong built-in field. In the end, a trade-off needs to be found between thickness and composition to get the targeted energy with a reasonable oscillator strength.

Localization

The behavior shown in Fig. 1.4 is deduced from simulations. To get these trends, the band structure for each thickness and composition was simulated with the help of the commercial software, NextNano. Even if we can get an idea of the energy of emission using simulations, in the case of InGaN QWs, the calculated values are often different from the experimental ones. In the simulations, the InGaN QW band structure is flat, and the percentage of indium is homogeneous in the InGaN layer. However, in reality, the composition at the nanoscale of the InGaN alloy is not homogeneous. Indeed, InGaN layers exhibit random indium composition fluctuations, which in turn create a disordered potential [33].

The potential fluctuations localize the carriers present in the QW. Localization was proposed to explain why InGaN LEDs are efficient even if the density of dislocations is high. Indeed, in other III-V semiconductors, dislocations are known to drastically decrease the LED efficiency. In the case of GaAs, for a dislocation density around 10^6 cm^{-2}, the efficiency is around 20% [34]. Blue LEDs exhibit InGaN/GaN QWs with an IQE reaching more than 80%,[11, 35–37] for a dislocation density higher than 10^8 cm^{-2}. Localization due to InGaN alloy fluctuations was proposed as a mechanism for diminishing the diffusion length of the carriers hence preventing them to reach NRCs such as threading dislocations [38, 39].

One of the easiest ways to observe localization in InGaN QWs consists in performing PL experiments as a function of temperature. Cho *et al.* discovered that the energy of the QW is not decreasing with temperature as expected from Eq. (1.8) [40]. The QW peak energy as a function of temperature exhibits a characteristic S-shape, see Fig. 1.5. This S-shape behavior can be explained in four steps: (1) At low temperature (12 K, in our case), all the carriers are evenly distributed across the energy landscape without the possibility of moving. (2) When the temperature increases, the carriers gain some energy and can reach some local minima, which will decrease the mean emission energy. A redshift can be observed for the QW energy, see Fig. 1.5(b). (3) As the temperature continues to increase (above 50 K, in Fig. 1.5(b)), the carriers start to delocalize and the QW energy blueshifts. (4) Finally, when the temperature is high enough (140 K, in our case), all the carriers are delocalized and the QW energy follows Varshni law, see Eq. (1.8).

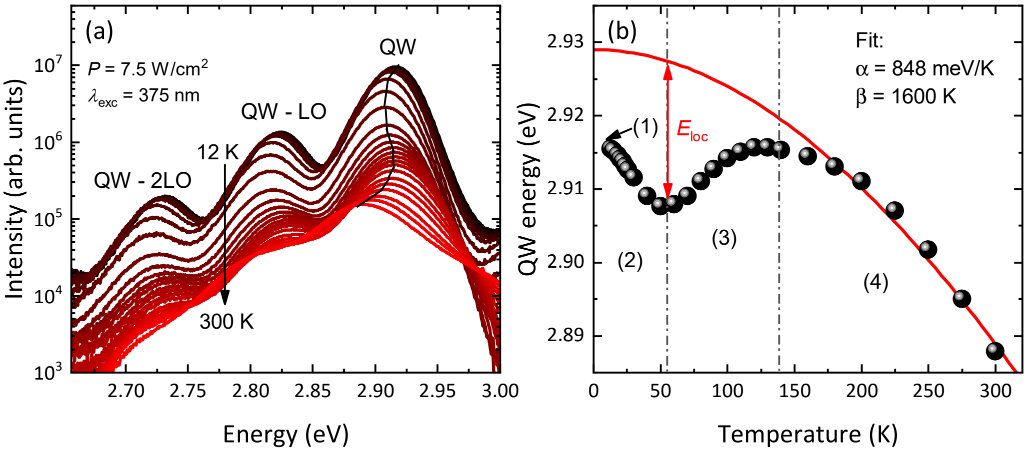

Figure 1.5 – PL spectra of an InGaN/GaN SQW as a function of temperature (a). Energy of the QW as a function of temperature (b). The typical S-shape behavior of an InGaN QW can be observed.

The "degree" of localization of two different samples can be compared by measuring the QW emission energy as a function of temperature. To quantify the localization, one can fit with Eq. (1.8) to the QW energy as a function of temperature in the high temperature range. The localization energy (E_{loc}) is the difference between the energy minimum and the fit, see Fig. 1.5(b). For Fig. 1.5(b), the localization energy is around 20 meV. Another way of finding the localization energy is by comparing the Stokes shift, which is the difference between the absorption edge and the emission energy (not used in this work). As InGaN will always have potential fluctuations which cannot be controlled, the only way to get a similar degree of localization between two samples is by growing the same QW using the same growth conditions.

1.3 Light-emitting diodes

In this section, we first discuss the basic features of LEDs. In a second part, the ABC model is discussed, and the Shockley-Read-Hall (SRH) recombination scheme is described in details.

1.3.1 The *p*-*n* junction

The basic building block of LEDs is the $p-n$ junction. A $p-n$ junction is created when an n-type material and a p-type material are brought together. In the ideal case, the junction between the two materials is abrupt. On one side, there is the p-type material with a density of dopant N_A and on the other side the n-type material with a density of dopants N_D. If we assume that all the dopants are ionized, the density of free holes p and electrons n will be N_A and N_D, respectively. When the two regions are in contact, the holes will start to diffuse toward the n-type side and the electrons toward the p-type side. This will create a region without any free carrier called the depletion region. The only charges staying in the depletion region are the ionized donors and acceptors which are fixed. This creates a built-in potential V_D, which is expressed as [41]:

$$V_D = k_B T/e \ln\left(\frac{N_D \cdot N_A}{n_i^2}\right), \tag{1.13}$$

where n_i is the intrinsic carrier concentration of the semiconductor and k_B is the Boltzman constant. When an external bias V is applied to the junction, the width of the depletion region, W_D, changes and is equal to:

$$W_D = \sqrt{\frac{2\varepsilon}{e}(V_D - V)\left(\frac{1}{N_A} + \frac{1}{N_D}\right)}, \tag{1.14}$$

with e the elementary charge, $\varepsilon = \varepsilon_{sc}\varepsilon_0$ with ε_{sc} the permittivity of the semiconductor and ε_0 the vacuum permittivity. The depletion region can thus be reduced or increased depending on the applied bias. For a forward bias, the electrons and the holes will be injected into the depletion region where they can recombine with each other. In such a case, the current density as a function of the applied voltage to the diode can be written as [42]:

$$J = e\left(\sqrt{\frac{D_p}{\tau_p}}N_A + \sqrt{\frac{D_n}{\tau_n}}N_D\right)\exp(e(V - V_D)/k_B T), \tag{1.15}$$

with D_j the diffusion carrier constant, and τ_j the minority carrier lifetime for the holes and the electrons ($j = p, n$). When the bias is higher than the diffusion voltage V_D, the current will exponentially grow.

Ideality factor

In the case of a real diode, to be able to understand the J-V curve, a simplified and empirical version of Eq. (1.15) is used:[43]

$$J \approx J_s e^{eV/(\eta_i k_B T)}, \tag{1.16}$$

with η_i the ideality factor. The ideality factor can be extracted from the I-V curve of an LED. This value will tell how the device behaves compares to the ideal diode equation (Eq. (1.15) with $\eta_i = 1$). In real diodes, the ideality factor varies as a function of the current. This gives information about the injection regime. For an ideality factor equal to 1, the diffusion current dominates transport properties. For low currents, the recombination current due to NR recombinations (SRH) dominates, i.e., $\eta_i = 2$, and when the current increases the diffusion current takes over, i.e., $\eta_i = 1$. In the case of QW LEDs, the diffusion current will be driven by the radiative recombination occurring in the QW.

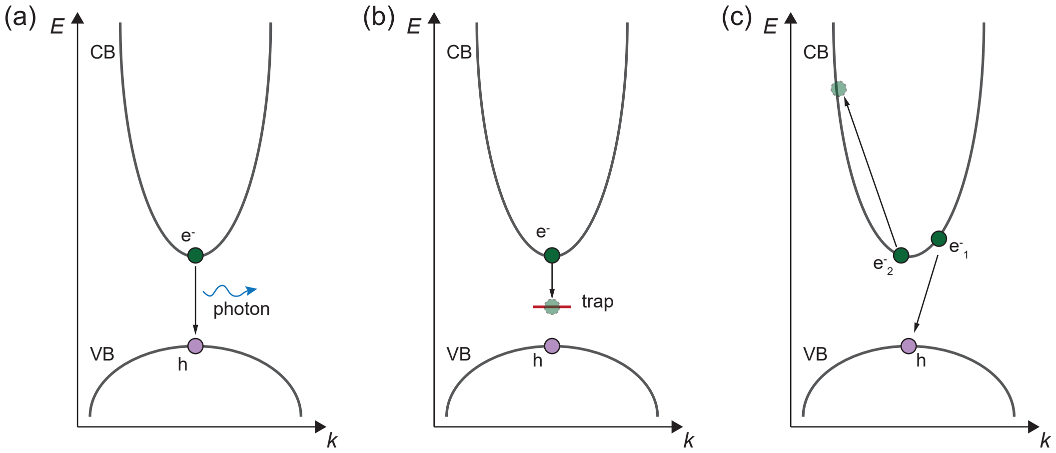

Figure 1.6 – (a) Radiative recombination: an electron and a hole recombine and emit a photon. (b) SRH recombination: an electron is captured by a trap present in the gap. (c) Auger recombination: an electron e_1^- and a hole h recombine and give their energy to another electron e_2^-. The recombination process presented in (b) and (c) can also happen for holes instead of electrons.

1.3.2 ABC model

The most important property of an LED is its ability to emit light. Therefore, it is useful to be able to characterize its efficiency. When carriers reach the active region of an LED, they will have two ways of recombining: radiatively or non-radiatively. The radiative recombination process occurs when an electron and a hole recombine by emitting a photon. The non-radiative recombination process can happen by trapping carriers (holes or electrons) or by Auger recombination, a three body process, see Fig. 1.6. The efficiency of an LED is given by its IQE, which can be written as [43]:

$$IQE = \frac{R_\mathrm{R}}{R_\mathrm{R} + R_\mathrm{NR}} = \frac{\tau_\mathrm{NR}}{\tau_\mathrm{NR} + \tau_\mathrm{R}}, \tag{1.17}$$

with R_R the radiative recombination rate, R_NR the non-radiative recombination rate, and the associated lifetimes τ_R and τ_NR.

The radiative recombination rate can be written as $R_\mathrm{R} = Bn^2$ where B is the radiative coefficient and n is the number of carriers in the QW. The B coefficient mainly depends on the overlap between the hole and the electron wave-functions, i.e., the oscillator strength. Therefore, two QWs with the same composition and thickness shall have the same B coefficient.

As discussed earlier, the NR recombination rate depends on two processes: at low injection, the carriers can be captured by some traps forming deep states in the bandgap. This is called the SRH recombination for which only one carrier is trapped (either a hole or an electron). This will be discussed in more details in the next section. At higher injection, the carriers are subjected to the Auger recombination, which is a three-carrier process. Two carriers will exchange energy and give it to a third one which is promoted to a higher energy level, see Fig. 1.6(c). The NR recombination rate can be written as $R_{\mathrm{NR}} = An + Cn^3$ with A the SRH coefficient and C the Auger coefficient. With these different recombination rates and Eq. (1.17), we can express the IQE in the framework of the well known ABC model:

$$IQE = \frac{Bn}{A + Bn + Cn^2}, \tag{1.18}$$

However, the IQE is difficult to determine experimentally. The quantity which we can measure is the EQE which depends either on the optical power P or the injected current I. The EQE is given by the number of extracted photons divided by the number of injected electrons, i.e., $\frac{P}{h\nu} \cdot \frac{e}{I}$, with h the Planck constant and ν the photon frequency. The two quantities are proportional: $EQE = \eta_{inj}\eta_{ext}IQE$, with η_{inj} the injection efficiency and η_{ext} the extraction efficiency. Finally, we can write:

$$\mathrm{EQE} = \eta_{ext}\eta_{inj} \cdot \frac{Bn}{A + Bn + Cn^2}. \tag{1.19}$$

In most cases, the injection efficiency is assumed to be equal to 1. For the extraction efficiency, it is more complicated as it depends on the stack of layers, the surface roughness, the contact reflectivity, and other parameters. A method to extract the IQE from the EQE is presented in Sec. 1.4.3.

1.3.3 Shockley-Read-Hall recombination

In this work, the LEDs and QWs will be driven most of the time in the low injection regime where the SRH recombination process is the principal source of NR recombinations, as Auger recombination is negligible in the low injection regime. As explained before, SRH recombination happens when an electron or a hole is captured by a trap. These traps can be located at different energies in the bandgap. However, the most efficient traps are those situated in the middle of the bandgap [44]. We will assume only midgap traps, and that the number of carriers present in the QW is sufficient, i.e., the electron density is equal to the hole density, $n = p$. The NR lifetime can then be written as [44]:

$$\tau_{\mathrm{NR}} = \frac{\sigma_n + \sigma_p}{\sigma_n \sigma_p v_{th} N_t} = \frac{1}{\sigma v_{th} N_t} \tag{1.20}$$

with $\sigma_{n,p}$ the capture cross-section for electrons (n) or holes (p), v_{th} the thermal velocity and N_t the trap concentration. Often, the cross section of the holes and the electrons is replaced by an effective cross-section $\sigma = \frac{\sigma_n \sigma_p}{\sigma_n + \sigma_p}$. The cross-section strongly depends on the nature of the traps. Theoretical computations and experimental measurements, such as deep level optical spectroscopy, can give, for different kinds of traps, an insight about the capture cross-section (or the capture coefficient, $C_{n,p} = v_{th}\sigma_{n,p}$ [45, 46]) [47, 48]. The link with the SRH coefficient present in the ABC model can easily be found [47]:

$$A = \frac{C_n C_p}{C_n + C_p} N_t. \tag{1.21}$$

Depending on the number of traps present in the QW, the IQE will be more or less affected. In Fig. 1.7, different IQE curves are displayed where the A coefficient is varied while B and C are fixed. When A is increased, the maximum of IQE decreases as there are more NR recombinations. Furthermore, the carrier density to reach the maximum of IQE also increases. Here, we assumed that when the trap density is increased only the SRH coefficient is impacted. However, recently, David *et al.* showed that Auger recombination can be enhanced by the number of traps present in the QW (trap-assisted Auger recombination) [12]. Therefore, the reduction of the trap density is important to get a high IQE but also a smaller droop.

The traps, which are involved in the SRH recombination, can be of different natures. One of the first to come to mind are impurities such as carbon, oxygen, iron, etc. Often, it is possible to reduce the concentration of impurities by controlling the gases and the environment during the growth. Other NRCs can be dislocations or crystal defects, which are more problematic to reduce as they are generated by the heteroepitaxy on sapphire or silicon substrates.

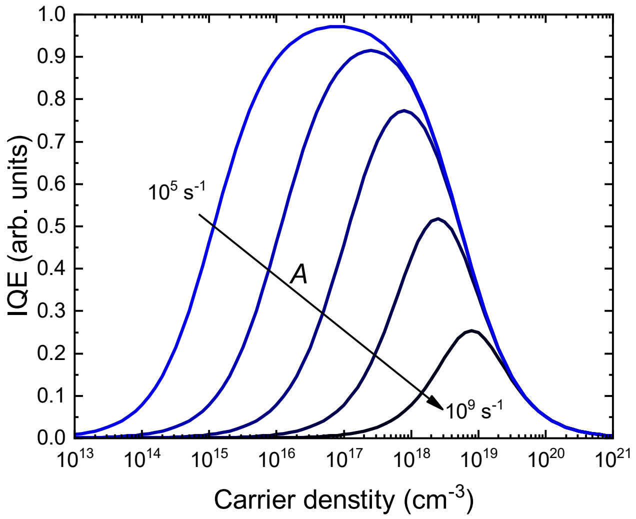

Figure 1.7 – IQE as a function of the carrier density for different values of the A coefficient. The B and C coefficients are fixed to $8.6 \cdot 10^{-11}\mathrm{cm}^3\mathrm{s}^{-1}$ and $1.6 \cdot 10^{-29}$ $\mathrm{cm}^6\mathrm{s}^{-1}$, respectively.

1.4 Experimental techniques

In this section, we will discuss the different experimental techniques used in this work. The growth of III-N will be discussed first with a focus on MOVPE, as all the samples presented here are grown with this technique. Then, the PL and the TRPL set-ups will be described. Finally, the characterization of LEDs will be discussed.

1.4.1 Growth

Substrate

The growth of III-nitrides was a real challenge for many years as no lattice-matched substrate was readily available. Indeed, contrary to other III-V materials, bulk GaN crystal was not available until recently. For a long time, the only substrate available was sapphire (Al_2O_3) substrate. In the 1960s, the first GaN layers on sapphire with a reasonable quality were grown by vapor phase epitaxy [49]. In 1986 [4], Amano *et al.* proposed to use an AlN buffer on top of the sapphire before growing the GaN buffer and managed to grow GaN films with a much better crystal quality. For a long time, only sapphire templates were available. Nowadays, several substrates can be found on the market for the growth of GaN [50]. We will present the two substrates used in this work: GaN on sapphire templates and freestanding GaN.

C-plane sapphire is one of the most commonly used substrates for the production of LEDs. To manage the growth of GaN films with a reasonable density of dislocations (1×10^9 cm^{-2}), the following steps are required. The first step is called the nitridation. To realize this step in MOVPE, the surface is exposed to ammonia (NH_3) and hydrogen, which react with the sapphire to form a thin layer of AlN. The next step is the growth of a GaN layer at LT (550 °C), which is annealed at 1000°C under H_2 to create 3D islands. Finally, a thick GaN layer of few μm grown at HT is deposited. This layer smooths the surface morphology and allows some of the dislocations to merge, which reduces the total amount of threading dislocations present in the GaN epilayer. Nowadays, 2" GaN on sapphire templates can be bought for 100$. Their dislocation density is around 1×10^8 cm^{-2}, which is mainly due to the lattice mismatch between GaN and sapphire.

Even, if GaN on sapphire templates are used for LEDs, for other applications such as laser diodes, a substrate with a lower dislocation density is required to reach long device lifetimes. As the fabrication of GaN substrates with the Czochralski process is not possible, free-standing GaN was developed as an alternative to real single crystal substrates. In this work, we used substrates which are supplied by Sumitomo Electric. For those substrates, the fabrication is starting with a GaAs substrate where a thick layer of GaN is deposited by hybrid vapor phase epitaxy (HVPE). After the growth of almost 0.5 mm of GaN, the GaAs substrate is removed and the GaN layer is polished to obtain a FS-GaN substrate [51]. FS-GaN substrates have a dislocation density around 1×10^6 cm^{-2}. As the quality is higher and the fabrication more complicated than for GaN on sapphire templates, the price for a 2" c-plane FS-GaN substrate is around 1000-1500$.

Metal organic vapor phase epitaxy (MOVPE)

MOVPE is a chemical vapor deposition technique which allows to grow thin layers of material. Metalorganic precursors are used to bring the different metals to the growth chamber where they react with ammonia at the surface and create a thin crystalline layer of crystal. In this

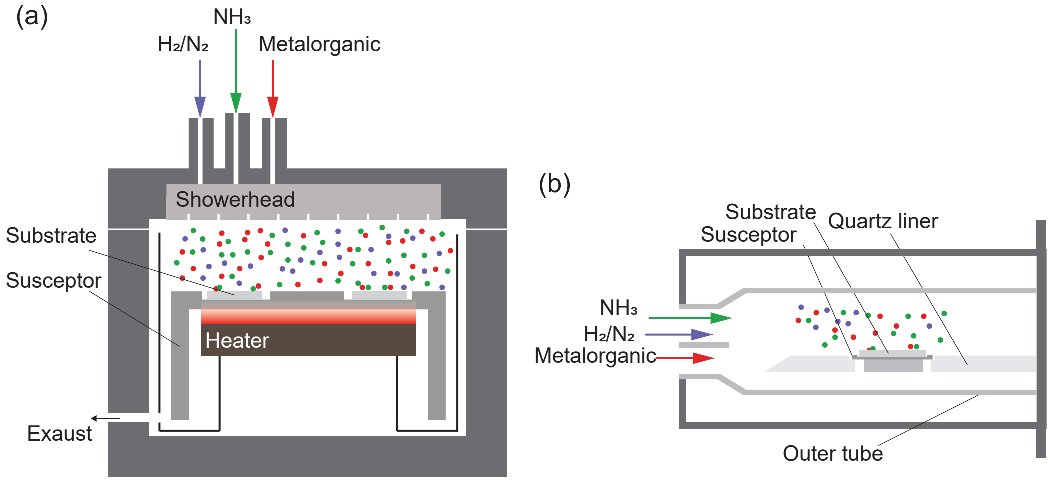

Figure 1.8 – (a) Schematic view of the showerhead reactor. (b) Schematic view of the horizontal reactor.

section, we will discuss only MOVPE, but other technologies such as MBE and HVPE can also be used to grow III-nitride films. However, MOVPE is the most widely used technique in the industry for the growth of III-nitrides as it has a high repeatability and gives films with high optical quality.

The different metalorganics are contained in a bubbler at a given temperature. A carrier gas which can be either H_2 or N_2 is passing through the bubbler and collect the metalorganic vapor. This flow is brought to the growth chamber where it mixes with NH_3, which provides the nitrogen atoms. In the chamber, the substrate is heated at a given temperature, which cracks NH_3 and the metalorganics. Then the atoms are free to bind to the surface.

We used TMGa, TEGa, TMIn, TMAl for the metallic atoms, and SiH_4, Cp_2Mg for n-type doping and p-type doping, respectively. TMGa is used for the growth at HT with H_2 used as carrier gas while TEGa is used during the growth of LT layers with N_2 used as carrier gas.

In this work, we used two different types of MOVPE reactor: a showerhead reactor (Aixtron 3 × 2” CCS) and a horizontal reactor (Aixtron 200/4 RF-S), see Fig. 1.8. The basic principle is the same, but the materials in the chamber and the heating system are different. For the showerhead reactor, see Fig. 1.8 (a), a susceptor is placed on top of a coil where a current is passing through thus heating the susceptor. The susceptor has some specific spots, called pockets, where substrates can be placed. The showerhead is on top of the susceptor and distributes the different gases. The showerhead temperature is kept around 55 °C to avoid reaction on the surface. The chamber and the showerhead are made of stainless steel. For the horizontal reactor, see Fig. 1.8 (b), a susceptor made of graphite is placed in the chamber surrounded by a quartz liner. There is no coil to heat the susceptor in this machine. Instead, RF induction is used to heat the susceptor.

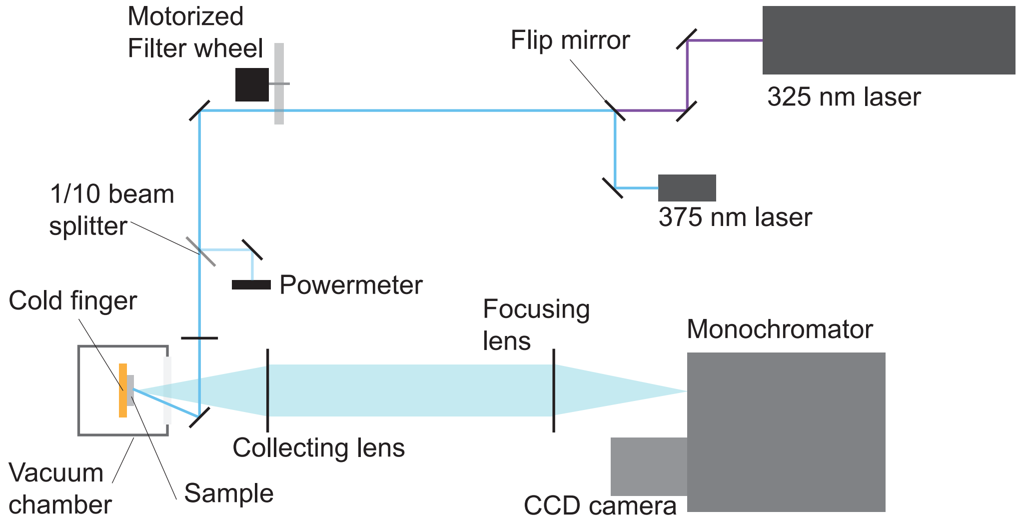

Figure 1.9 – Schematic view of the PL setup used in this work. In the vacuum chamber, a cold finger connected to a closed-cycle helium cryostat. On the cold finger, the sample is glued, which will allow to vary the temperature.

1.4.2 Photoluminescence

The principle of PL is straightforward. A pump laser excites a material where it generates electron-hole pairs. The carriers recombine either radiatively or non-radiatively. A spectrometer collects the luminescence that carriers produce when they recombine radiatively. A schematic view of our set-up is shown in Fig. 1.9.

Depending on the experiments, two kinds of continuous wave pump laser are used: a HeCd gas laser emitting at 325 nm or a semiconductor laser emitting at 375 nm. The energy of the HeCd laser is high enough to pump above the bandgap of GaN, which is useful to get an overview of all the features in the sample used in this work. The 375 nm semiconductor laser has the particularity to pump below the bandgap of GaN. Therefore, it is possible to perform quasi-resonant pumping in the InGaN/GaN QWs, i.e., this laser is only absorbed by the InGaN QW. The laser beam size on the sample is around 180 μm in diameter.

PL temperature series can be done thanks to a closed-cycle helium cryostat controlled by a temperature controller. The temperature range is between 12 and 300 K. Additionally, the pump laser power can also be varied with a filter wheel, allowing us to do power series. The light coming out of the sample is collected by two lenses, and analyzed by a Jobin Yvon iHR320 monochromator coupled to a Peltier cooled CCD detector.

PL temperature and power series are used to get an idea about the IQE of an InGaN QW. For this purpose, the ratio between the integrated PL of the QW emission at room temperature (300 K) and at low temperature (12 K) is computed for different powers. The measurements can be repeated for several samples, and the ratio can be compared. In this work, this PL ratio will be noted $Q_{\mathrm{PL},300\,\mathrm{K}/12\,\mathrm{K}}$. It gives an idea about the IQE of the QW at a given excitation power density. Indeed, when the temperature is decreased, the NR centers become inactive and all the carriers should recombine radiatively. This is likely not the the case at 12 K, and the IQE extracted this way must be taken with cares. In addition, the PL ratio strongly depends on the carrier concentration in the QW. When QWs are compared, one should be sure that a similar number of carriers are in the QW, i.e., that the absorption and the laser excitation power density are similar. In this work, to avoid any issues with a variation of excitation power density, when samples are compared by this method, all measurements are performed in a row.

The PL ratio as a function of excitation power density should follow the IQE curve of an LED under electrical injection. At low injection, the SRH recombination dominates. Then, for a higher injection, the maximum of IQE is reached. At high injection, Auger recombination starts to dominate. As we are mainly interested in the SRH recombination, the excitation power density is always chosen to be sensitive to the first regime. Therefore, the PL ratio shown in this work can never be compared with the maximum of IQE of a QW. It is only useful to compare the efficiency of QW between them.

Time-resolved photoluminescence

TRPL works with the same principle as PL except that the pump laser is a pulsed laser and the detector unit is a monochromator coupled with a Hamamatsu streak camera operating in synchroscan mode, which allows to monitor the carrier recombination as a function of time. In our set-up, the laser is the third harmonic of a mode-locked Ti:sapphire laser emitting at 280 nm with a 2 ps pulse length, and a repetition rate of 80.5 MHz. For all the TRPL measurements shown in this work, the laser was working under these conditions. As the PL decay can be longer than 1 ns, we used a pulse picker to extend the detection time window. The laser beam diameter on the sample is ~ 90 μm. In this set-up, temperature-dependent measurements can also be carried out thanks to a closed-cycle helium cryostat.

1.4.3 Electroluminescence

The characterization of LEDs is carried out with the help of a Keithley 2400 source meter and a calibrated photo-diode. The n and p contacts are connected with a needle probe station. Then, the LED is driven in voltage mode and the current passing through the device is measured. A calibrated photo-diode is placed on the backside of the device to collect and measure the EL intensity. For all the devices shown in this work, the n and p contacts are made of metal stack layers of Ti/Al/Ti/Au and Pd/Au, respectively. On this set-up, an optical fiber is connected to a spectrometer (a monochromator (MicroHR, Horiba Jobin Yvon) and a Peltier-cooled CCD (Horiba Jobin Yvon)), to measure the emission wavelength. With this set-up, we can easily acquire current-voltage (I-V) and light-current (L-I) curves, which gives us access to the EQE.

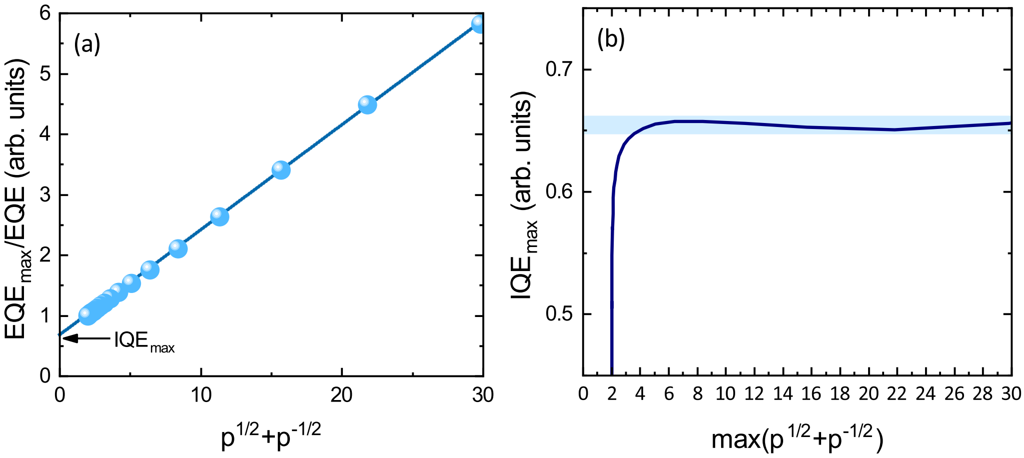

Figure 1.10 – (a) $\frac{EQE_{\text{max}}}{EQE}$ plotted as a function of $p^{\frac{1}{2}} + p^{-\frac{1}{2}}$. The blue dots are the experimental data and the blue line is a linear fit. The intersection of the linear fit with the y axis is the maximum of IQE. (b) Depending on the region used for the linear fit, the IQE maximum slightly varies.

Internal quantum efficiency

To determine the IQE of our devices, we used the method described in Dai *et al.*, [52] and Titkov *et al.* [36].

The first step is to plot $\frac{EQE_{\text{max}}}{EQE}$ as a function of $p^{\frac{1}{2}} + p^{-\frac{1}{2}}$, see Fig. 1.10, where p is defined as:

$$p = \frac{EQE \cdot I}{EQE_{\text{max}} \cdot I_{\text{max}}}, \tag{1.22}$$

with I the current, EQE_{max} the maximum of EQE, I_{max} the current at the maximum of EQE. We define Q as $Q = B/\sqrt{AC}$ where the A, B, and C coefficients are the ABC model coefficients. Using the ABC model equation with the assumption that the injection efficiency is equal to 1, see Eq. (1.19), we can show that:

$$\frac{EQE_{\text{max}}}{EQE} = IQE_{\text{max}} + \frac{p^{\frac{1}{2}} + p^{-\frac{1}{2}}}{Q+2}. \tag{1.23}$$

On Fig. 1.10, the y-intercept will be equal to IQE_{max}.

As for all the methods used to extract the IQE, it has some limitations. One of the hypotheses we made is that the ABC model holds for LEDs. However, for LEDs with a lot of NR recombinations some deviations from the ABC model have been observed, see Chap. 5. For such LEDs, the value of IQE_{max} might be wrong. The second important point is the range of $p^{\frac{1}{2}} + p^{-\frac{1}{2}}$ used to do the regression. Depending on this range, IQE_{max} can vary by several percents. In the end, this method is a good way of comparing samples provided they follow the ABC model and they have a similar structure.

2 Role of the InGaN underlayer

LEDs are composed of *p*-type and *n*-type doped layers with an active region including QWs emitting at the desired wavelength. QWs are used to spatially trap carriers along the growth axis direction, here the *c*-axis. This enhances the overlap between the hole and the electron wave-functions, thus improving the efficiency of the device. Furthermore, as the well is made of a ternary alloy, InGaN, the emission wavelength can be tuned by changing the indium composition. This offers an additional degree of freedom, as we are not forced to change the QW thickness to reach a different emission wavelength.

In III-nitrides, *p*-type doped material was difficult to obtain contrary to *n*-type doped material as GaN layers were naturally *n* doped. The first success for *p*-type doped GaN was reported in 1989 by Amano and Akasaki [5], by irradiating a GaN layer doped with Mg with an electron beam. The availability of *p*-type GaN opened up the realization of LEDs. In 1992, Nakamura *et al.* demonstrated conductive GaN:Mg layers after annealing around 600 °C [6], which is the technique used nowadays to activate *p*-type layers. The reason why annealing or irradiation is needed to activate the magnesium dopant is that Mg forms a bond with hydrogen creating a Mg-H complex during MOVPE growth [53, 54]. To break this bond (0.7 eV [55]), additional energy is needed and hydrogen needs to escape from the layer. Therefore, in III-nitrides, the growth of an LED always starts with the *n*-type material (often GaN:Si), then the active region is deposited, and finally, the *p*-type material is grown (often GaN:Mg). With the *p*-type doped region on top, hydrogen can escape from the sample upon annealing.

In many devices, after the growth of the active region, an electron blocking layer is grown. It is an AlGaN layer with a composition between 10 and 20 %. The role of this layer is to avoid electron overflow when the LED operates under high injection. On the *n*-type side, an additional layer can be found in InGaN/GaN QW LEDs. This underlayer is made of InGaN alloy and is present in all commercial blue LEDs. Even if this layer is massively used, its actual role was still unclear and under debate in the literature at the beginning of this thesis. The only well-established fact was that the InGaN UL is compulsory for getting high efficiency blue LEDs. In this chapter, we will discuss the mechanism behind this InGaN UL by looking through the different hypotheses that have been proposed in the literature. We designed

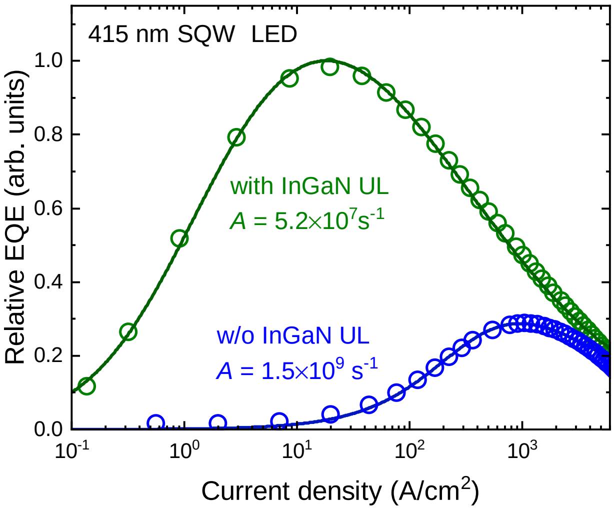

Figure 2.1 – Relative EQE of SQW LEDs without an InGaN UL (blue curve) and with an InGaN UL (green curve). Both curves are divided by the EQE maximum of the LEDs with an InGaN UL. The dots are the experimental data and the ABC model fitted to the data is shown as a line. The same *B* and *C* coefficients are used for both LEDs: $8.6 \cdot 10^{-11}$ $\mathrm{cm^3 s^{-1}}$ and $1.6 \cdot 10^{-29} \mathrm{cm^6 s^{-1}}$, respectively.

specific sets of samples and experiments to check each of these hypotheses.

2.1 Introduction

Nowadays, white LEDs are well developed and used in everyday life. Companies are using InGaN QW based LEDs emitting either at ~ 415 nm or at 450 nm combined with phosphors to produce white light [35]. Huge progress in material synthesis has been done since 2010. InGaN QWs exhibit nowadays an IQE higher than 90 % [11, 35–37]. When the epitaxial structure of these devices is studied in depth, one can find on the n-type side of the LEDs an additional InGaN layer, with a lower indium content than in the one of the active region. This layer has been called an UL, a prelayer, a strain compensating layer or an electron reservoir layer depending on the papers [56–65]. In this work, we will call it UL as it has no specific connotation about its presumed role.

InGaN UL is claimed to strongly increase the efficiency of blue LEDs containing InGaN QWs. We thus tried to reproduce this enhancement on LEDs which only have a single InGaN/GaN QW. We chose to use SQW LEDs as it simplifies the understanding of the carrier injection, i.e. all the emitted blue light will come from the SQW. In the case of MQW LEDs, it has been reported that not all of the QWs are injected in a similar way [66], which can make the interpretation more challenging. Additionally, the impact of the InGaN UL is on a single layer (the InGaN SQW), thus making all subsequent analyses easier. For that purpose, two SQW LEDs emitting at 415 nm were grown by MOVPE on a GaN on sapphire template. The InGaN SQW is 2.7 nm thick with an indium composition about 12%. The two LEDs are identical except that one includes a 55 nm thick $In_{0.03}Ga_{0.97}N$ UL in one of them. The EQE curve is displayed in Fig. 2.1. As expected, the maximum of EQE is improved by a factor of 4 for the device featuring an InGaN UL. Also, its EQE maximum is shifted toward lower current density. To analyze the EQE curves more carefully, we applied the ABC model (see Chap. 1.3.2). As the InGaN/GaN SQW is similar for both LEDs, the radiative coefficient B should be the same. For the C coefficient, we first assume that the value does not change between the two LEDs. However, the effective C coefficient can be slightly different as shown by David *et al.* [12] when the density of traps increases in the QW. The fitting procedure was adjusted in the low current density regime to extract the A coefficient. We found that the SRH coefficient (A) is decreased by almost two orders of magnitude when there is an InGaN UL.

As mentioned, the increase of EQE when adding an InGaN UL is well documented in the literature, [56–65]. However, the reasons which have been invoked are numerous. We will investigate each of them in the following sections.

2.2 Injection efficiency

Hypothesis from the literature

One of the hypotheses that can be found in the literature is that the InGaN UL improves the carrier injection [57, 58, 60, 62]. The idea is that the InGaN UL is added to balance the injection of the electrons compared to the one of the holes. The authors performed PL or EL to characterize the performance of each device. In all the cases, they observed a better performance (optical and electrical) of LEDs when the InGaN UL (namely the electron reservoir layer in the papers) is added below the active region. In all these papers, the active region is made of MQWs.

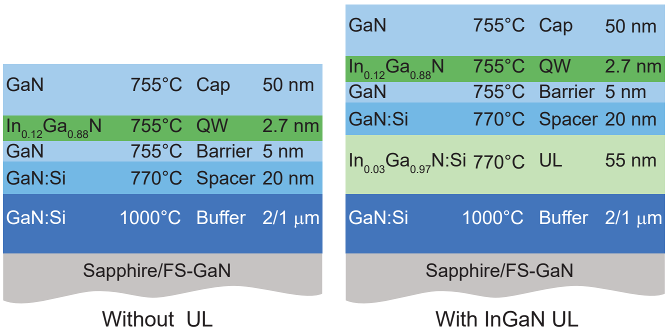

Figure 2.2 – Main sample structure used in this chapter.

Our study

In order to test this hypothesis, we performed an experiment where we generate the carriers directly in the InGaN QW. If the main mechanism of the InGaN UL is to help with the carrier injection, there should be no difference between a sample with and without InGaN UL in such excitation scheme. For this purpose, quasi-resonant PL experiments are the best choice. Quasi-resonant PL is realized with a continuous wave laser whose excitation energy is below the GaN bandgap and above the energy minimum of the QW. Therefore, carriers are generated directly in the InGaN SQW.

For this study, we grew two samples by MOVPE on GaN on sapphire template, see Fig. 2.2. The only difference between the two samples is the insertion of an InGaN UL. For both samples, the buffer is grown with TMGa under H_2, and the rest of the sample is grown with TEGa and TMIn under N_2. The structure was kept as simple as possible and as close as possible to the one of the LEDs used in Fig. 2.1 but without any *p*-type as we only perform optical pumping. The 2.7 nm thick InGaN QW emits around 2.85 eV (indium content around 12%), which allows us to do quasi-resonant PL using a 375 nm semiconductor laser diode (3.3 eV). The PL data for these two samples can be seen in Fig. 2.3.

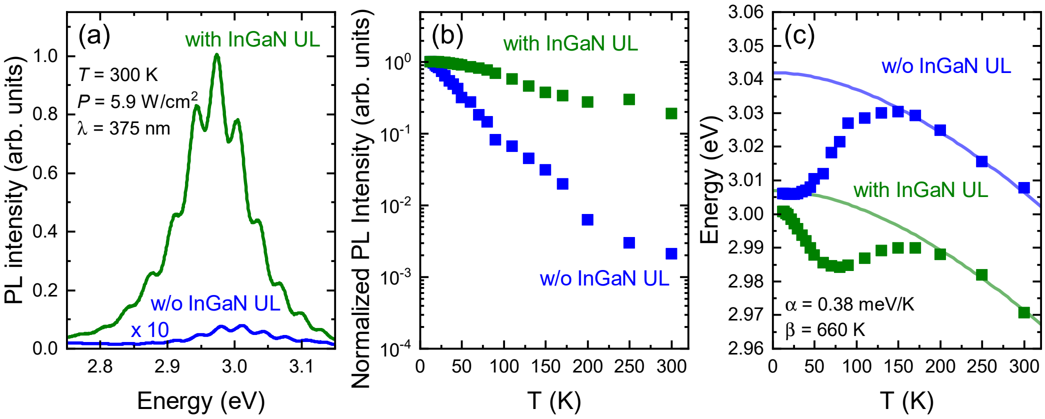

Figure 2.3 – PL spectra recorded under quasi-resonant pumping at 300 K for the sample with an InGaN UL (green) and without UL (blue) grown on sapphire substrate (a). Normalized PL intensity as function of temperature for the two samples (b). QW peak energy as a function of temperature for the same samples (lines are fits obtained with Eq. (1.8), (c)).

Fig. 2.3(a) displays the 300 K PL spectra for the SQW without an InGaN UL (blue) and with an InGaN UL (green). The PL intensity is almost two orders of magnitude higher for the sample with an InGaN UL (Fig. 2.3(b)). Additionally, we can notice that the SQW emission comes from delocalized states (above the mobility edge), even if they have a difference in localization energy (35 and 20 meV for the sample without and with UL, respectively), see Fig. 2.3(c). The difference in localization energy is still unclear but it goes in the other way around since the lower the localization, the higher the efficiency should be. The PL intensity ratio between low and room temperature for the QW with an InGaN UL is $Q_{\mathrm{PL},300\,\mathrm{K}/12\,\mathrm{K}} = 0.19$ while it is only $Q_{\mathrm{PL},300\,\mathrm{K}/12\,\mathrm{K}} = 0.002$ for the sample without an InGaN UL. The IQE is therefore significantly higher for the SQW with an InGaN UL. Therefore, we can conclude that the main role of the UL is not to improve the injection efficiency.

2.3 Threading dislocation

Hypothesis from the literature

As LEDs in III-nitrides are mainly grown on GaN on sapphire templates, the initial dislocation density of the template is rather high, i.e., $\sim 2 \times 10^8$ cm^{-2}(extracted from HR-XRD [67]). This is due to the lattice parameter difference, around 15%, between the sapphire substrate and the GaN layer [50]. The mismatch creates some threading dislocations along the c-axis. In conventional III-V semiconductors, dislocations are known to decrease the LED efficiency drastically [34]. However, in III-nitrides, dislocations seem less problematic, and high efficiencies can be reached with a high dislocation density [68]. One of the proposed mechanisms is that the InGaN UL stops the threading dislocations [61]. Trömä *et al.* [61] performed an AFM analysis on top of two MQW structures, one with an InGaN UL and one without an InGaN UL grown on sapphire substrate. They noticed a reduction of the number of pits for the sample with an InGaN UL. They deduced a lower density of threading dislocations (10 % to 20 % less) for the sample with an InGaN UL and proposed this as an explanation for the improvement of the LED efficiency.

Our study

We performed AFM scans on the previous samples in order to compare the density of V-pits. While not every dislocation will create V-pits, they reflect the density of threading dislocations [69].

AFM images are shown in Figs. 2.4(a) and 2.4(b). The V-pit density is 3.4×10^8 and 4.2×10^8 cm^{-2} for the sample without and with an InGaN UL, respectively. The densities are rather similar, but on top of each SQW, a 50 nm thick GaN cap were grown which could have an impact on the measured density. Thus, two new samples sharing the same structure but without the SQW neither the cap are grown. Therefore, AFM probes the surface morphology just before the growth of the SQW. The AFM images are shown in Figs. 2.4(c) and 2.4(d). A statistic realized on 10 AFM images for each sample gives a density of 2×10^8 cm^{-2} for the sample without UL and 6×10^8 cm^{-2} for the sample with an InGaN UL. One can conclude that the InGaN UL does not reduce the dislocation density. Besides, the InGaN UL revealed threading dislocations by forming V-pits. Indeed, indium is known to lower the surface energy, which can in turn promote the creation of pits [69]. In conclusion, we observe more pits when the UL is present, which is going against the proposed hypothesis.

To investigate further the impact of dislocations, the same structures as those shown in Fig. 2.2 were grown but this time on FS-GaN where the dislocation density is around 10^6 cm^{-2}, i.e.

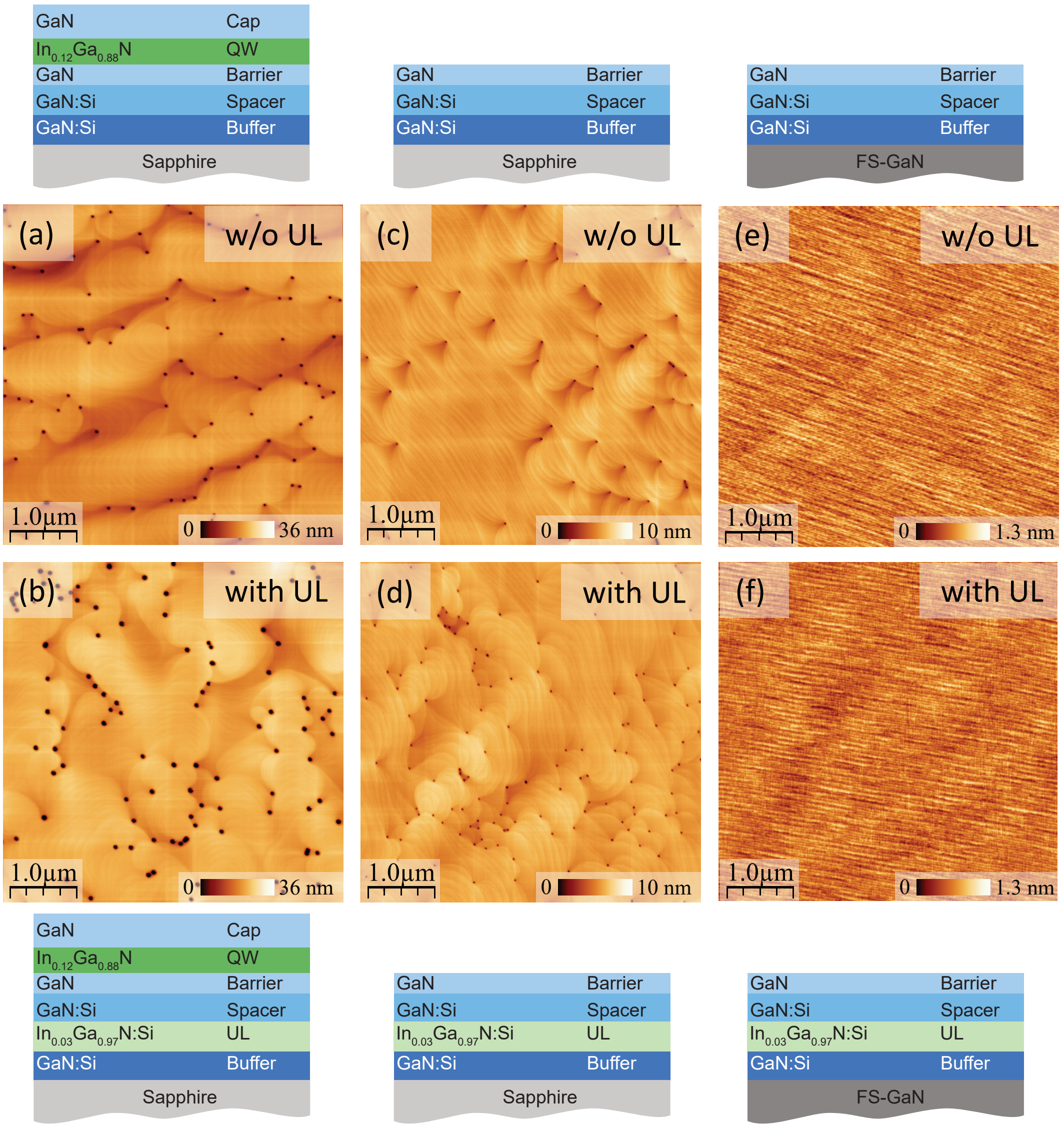

Figure 2.4 – 5×5 μm^2 AFM images of the samples (Fig. 2.2) grown on sapphire without UL, (a), and with UL, (b). A similar sample as in Fig. 2.2 was grown but the growth was stopped before the QW. AFM images (c) and (d) show the surface morphology before the QW when the samples are grown on sapphire. Similar surface morphology images are shown for samples grown on FS-GaN, without and with UL, in (e) and (f), respectively. Note that the same height scale was chosen for each category of samples.

two orders of magnitude lower than on sapphire. By performing AFM scans on these samples, we did not observe any V-pits, see Figs. 2.4(e) and 2.4(f). We then performed quasi-resonant PL on these samples. Surprisingly, we still observed a positive effect of the InGaN UL on the SQW emission, see Fig. 2.5(a). If the suppression of threading dislocations by the UL was the main mechanism governing the efficiency of LEDs, the effect of the InGaN UL on FS-GaN should be negligible. However, it is not the case here, as can be seen in Figs. 2.5(a) and 2.5(b).

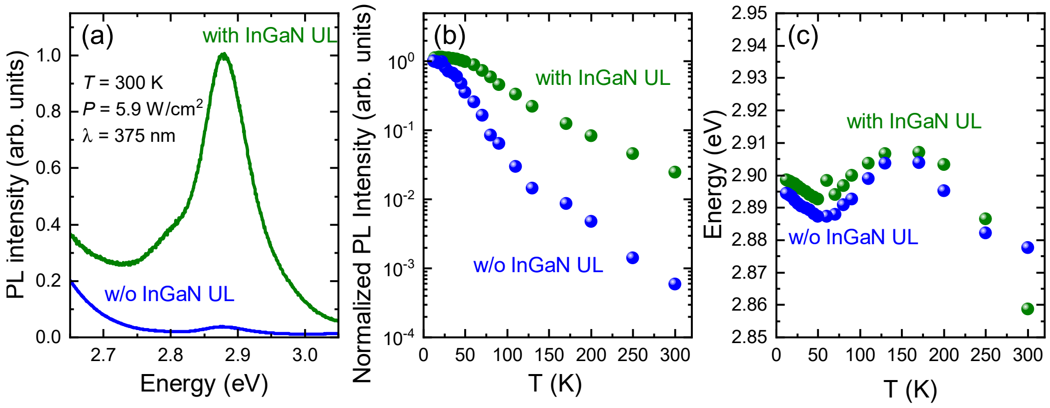

Figure 2.5 – PL spectra recorded at 300 K for the sample with an InGaN UL (green) and without UL (blue) grown on FS-GaN substrate (a). PL intensity as function of temperature for the same two samples, (b). Peak energy of the QW as a function of temperature for the same samples, (c).

The SQW intensity is still increased by a factor of 40 when an InGaN UL is added which is a bit smaller than the improvement observed on sapphire (factor of 90). We can thus conclude that the role of the UL is not to reduce the threading dislocation density.

2.4 Formation of V-pits

Hypothesis from the literature

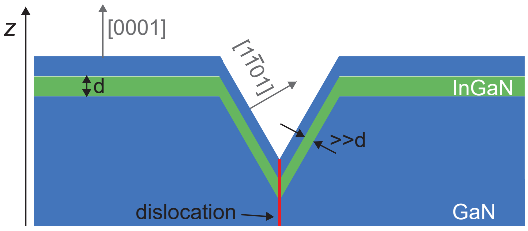

Figure 2.6 – Schematic view of a V-pit and its impact on an InGaN QW. The V-pit expose to the growth the semi-polar plane. The indium incorporation is diminish on the side of the V-pit and the QW thickness (*d*) is smaller than on the *c*-plane.

Looking at the results found in the last section, we could think that the role of the InGaN UL is to promote the formation of V-pits on top of threading dislocations. To explain why threading dislocations seem to not critically affect the blue LED efficiency, A. Hangleiter *et al.* invoked the formation of V-pits [70]. The specific geometry of the pit exposes semi-polar planes to the growth front, for which the indium incorporation is lower. Additionally, the QW is thinner on these planes. These two effects create an energy barrier around each dislocation, which prevents carriers from being captured. This mechanism leads to a self-screening of the dislocations. Therefore, promoting V-pits could be the main effect of the InGaN UL, as proposed by Zhao *et al.* and Okada *et al.* [71, 72].

Our study

We performed the same experiments than those previously performed on sapphire template but on FS-GaN. The surface morphology of the samples whose growth was stopped prior to the QW is shown in Figs. 2.4(e) and 2.4(f). As expected, neither dislocation nor V-pit can be observed in both cases. As the morphology is similar, one should expect no difference between the samples.

As in section 2.2, quasi-resonant PL has been performed on this sample series. At room temperature, a clear difference by a factor of 40 in PL intensity between the sample with and without an InGaN UL can be observed, see Fig. 2.5(a). The PL intensity dependence as a function of temperature is shown in Fig. 2.5(b). Above 50 K, the intensity of the QW without UL decreases much faster than its counterpart. The behavior of the peak energy with the temperature is nearly identical, which allows us to conclude that the localization in both samples is similar, see Fig. 2.5(c). This is not surprising as the two QWs are the same. One can conclude that the UL does not impact on the microscopic potential landscape of the QW.

Even for a substrate with a low dislocation density, the InGaN UL improves the QW emission by a factor of 40. As the UL still improves the efficiency when V-pits are absent, we can conclude that the self-screening of dislocations due to pits is not the main effect at play.

2.5 Impact on the step edge morphology

During the growth of the samples, the growth proceeds with the step-flow mode. As indium is a surfactant and may change the surface kinetics, we decided to check if the step edge morphology changes depending on the presence of the InGaN UL (single ML step edge or double ML step edge). The idea behind this is that the incorporation of defects could be different for single ML step edges or double ML step edges.

To study this effect, AFM images of 1×1 μm^2 are taken on several locations on the two samples for which the cap and the QW are missing. Fig. 2.7 shows typical AFM images, (a) and (b), and height profiles, (c) and (d). The spacing between the dotted gray lines is the height of one ML (0.259 nm). We can conclude that the InGaN UL does not impact the step edge height. On average, only single ML steps were found in both cases. We can thus conclude that the InGaN UL is not changing the step edges, and thereby the carrier localization.

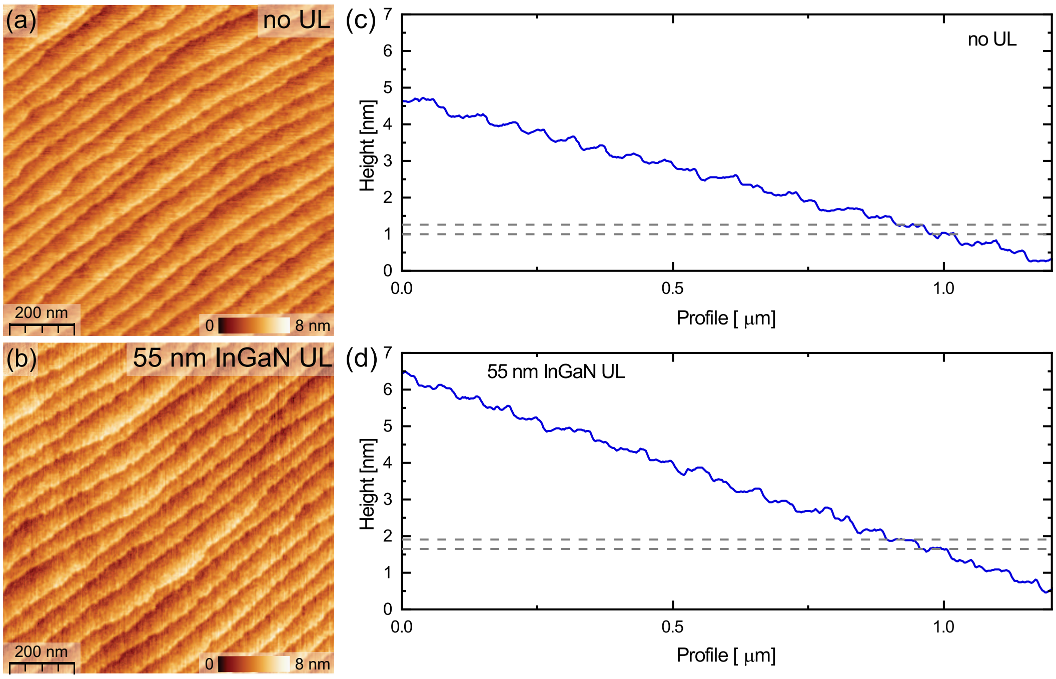

Figure 2.7 – 1 × 1 μm^{2}AFM images for a sample on FS-GaN without UL (a) and with an InGaN UL (b). The height profile taken from the top left edge to the bottom right edge for the case without UL (c) and with an InGaN UL (d). The separation between the two gray lines is 2.592 Åwhich is the height of a GaN ML.

2.6 Reduction of the electric field

Hypothesis from the literature

Another hypothesis, proposed by Davies *et al.* [37, 63] and other groups [65], is that the InGaN UL decreases the built-in field in the InGaN QW, thus increasing the oscillator strength. Indeed, as exposed in Sec. 1.2.2, InGaN QWs are sensitive to the built-in field generated by the difference of polarization between the well and the barrier materials. When the built-in field increases in the QW, the wave-function overlap of the electron and the hole decreases thus reducing the oscillator strength. As the radiative lifetime depends on the oscillator strength, the QW efficiency should change as a function of the built-in field [27, 28].

Davies *et al.* investigated samples with and without an InGaN UL featuring a SQW [63]. They also tried to replace the InGaN:Si UL by a GaN:Si UL grown at LT and HT and an undoped GaN layer. In their sample, the GaN thickness between the InGaN UL and the InGaN QW is very thin, i.e., 3 nm. TRPL at 10 K was performed on these samples. They observed a similar lifetime for the sample with LT GaN UL and HT GaN UL (19 ns). For the sample with an InGaN:Si UL, the lifetime was 10 ns at low temperature. This shows that the radiative lifetime is shorter for this sample than for the sample without the InGaN UL. To understand these results, they used NextNano simulations to show that the built-in field in the QW is lower. Therefore, they proposed that the main mechanism of the InGaN UL is to reduce the built-in field in the QW, which in turn enhances the wave-function overlap.

Our study

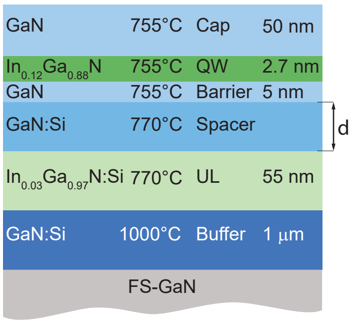

Figure 2.8 – Samples grown with a spacer of 20 nm, 50 nm and 100 nm for built-in field studies. The silicon doping level is $3 \cdot 10^{18}$ cm^{-3}.

In the experiments of Davies *et al.*, the UL was located near the QW where the band bending is strong. Therefore, a study on the impact of the distance between the UL and the SQW can give us some insights into this hypothesis. For this purpose, we looked at a simple structure, see Fig. 2.8 where we varied the spacer thickness between the UL and the SQW.

The first step is to simulate this structure with the software NextNano. The simulations are done for a spacer thickness varying from 0 to 120 nm. As the spacer doping may also have an impact on the built-in field, we performed the simulations for three different silicon doping levels: 3×10^{17} cm^{-3}, which corresponds to the unintentional doping level, 5×10^{17} cm^{-3}, and 3×10^{18} cm^{-3}, which corresponds to the n-type doping level of LEDs. For each spacer thickness, the ground state wave-function of the hole and of the electron are computed, and the oscillator strength is extracted. The oscillator strength decreases when the spacer thickness is increased (Fig. 2.9(a)). Depending on the doping level, after a given thickness, the InGaN UL has no impact on the QW built-in field. For instance, in the case of a doping level around 3×10^{18} cm^{-3}, the thickness is 20 nm. Therefore, for the standard spacer thickness, the QW built-in field is not reduced by the InGaN UL.

To check the simulation prediction, we grew three samples with different spacer thicknesses (20, 50, and 100 nm) with a doping level of 3×10^{18} cm^{-3}. Whereas the spacer thickness is increased up to 100 nm, the intensity of the SQW remains the same (Fig. 2.9(b)). Therefore, we can safely conclude that the main role of the InGaN UL is not to reduce the QW built-in field.

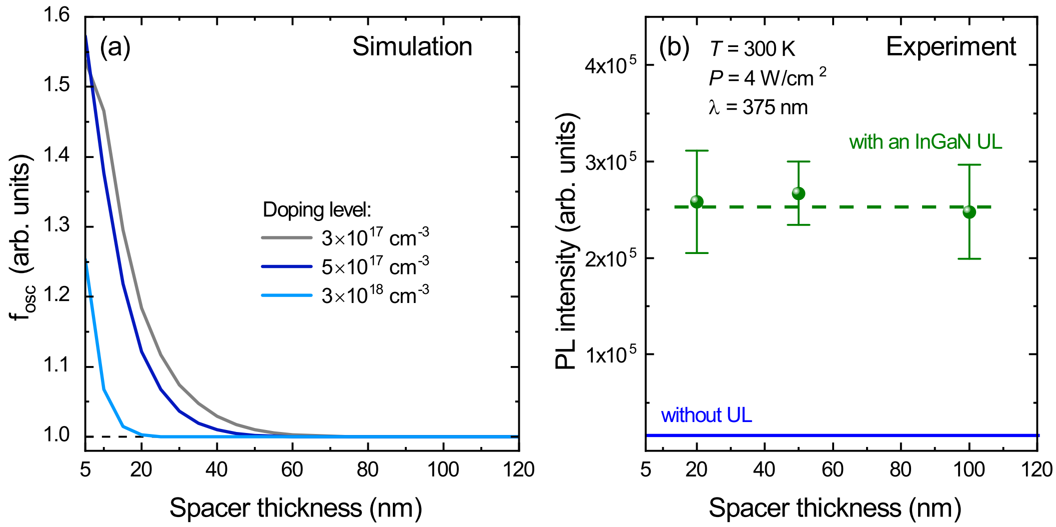

Figure 2.9 – (a) Oscillator strength as a function of the spacer thickness when an InGaN UL is present. Three different doping levels are considered. (b) PL intensity as a function of spacer thickness (20, 50, and 100 nm). The sample structure is shown in Fig. 2.8.

2.7 Strain management

Hypothesis from the literature

When growing an InGaN QW on GaN, the InGaN material is under compressive strain. This compressive strain could generate a piezoelectric field which induces a lower oscillator strength. It was also proposed that strain may create some defects in the QW [59]. Several papers proposed that the insertion of an InGaN UL could change the strain state of the QW, decreasing thereby the electric field and/or the number of point defects. It was thus proposed that the InGaN UL acts as a strain compensating layer [59, 73, 74].

Our study

To study this hypothesis, an experiment was designed to test the strain condition of a layer after the growth of an InGaN UL. We chose to test the strain state of a 30 nm thick GaN layer by analyzing the band edge PL at low temperature. For this purpose, two samples were carefully designed (Fig. 2.10 left) to maximize the luminescence coming from the top GaN layer. Therefore, to avoid any parasitic signal coming from the buffer, a 500 nm thick $Al_{0.06}Ga_{0.94}N$ layer was added after the buffer to absorb most of the laser power.[1]

To probe the strain state of the 30 nm thick GaN layer, PL was performed with a 325 nm HeCd laser at 11 K. Thanks to the $Al_{0.06}Ga_{0.94}N$ layer, the main signal comes from the top GaN layer. Figure 2.10 shows the GaN band edge for the sample without UL (blue) and with an InGaN UL

---

[1] After 500 nm of $Al_{0.06}Ga_{0.94}N$, only 0.3% of the initial excitation power reaches the buffer.

(green). For the sample without UL, the free A exciton (FX_A) and the free B exciton (FX_B) are more visible than in the sample with an InGaN UL. We hypothesize that free excitons could diffuse toward the InGaN UL and recombine in the InGaN UL. On the other hand, the neutral donor bound exciton A (D^0X_A) is localized and the intensity is similar in both cases.

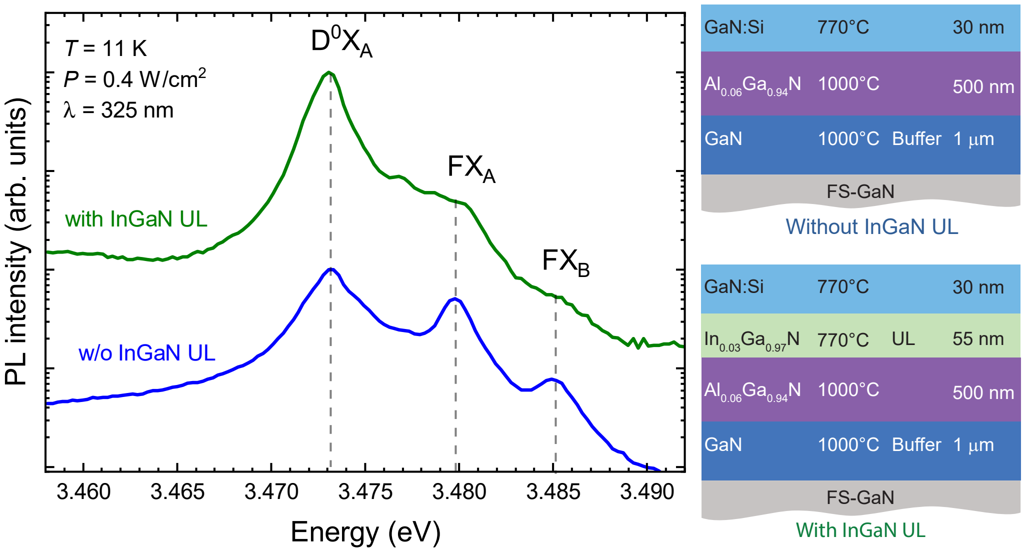

Figure 2.10 – Left: PL spectra, shifted for clarity, of the GaN band edge recorded at 11 K, for a sample without UL and with an InGaN UL. Right: Schematic view of the two samples analyzed by PL.

The striking feature is that the energy position of the excitons for both samples is identical. The D^0X_A and the FX_A energy are 3.473 eV and 3.480 eV, respectively which is close to the reported transition energy for unstrained GaN [20, 75]. This measurement of the band edge was repeated at different positions on the two samples. We observed some variations on both samples, around 0.3 meV, which corresponds to 0.4 kbar. This variation might come from the substrate itself as FS-GaN substrates have some residual strain inhomogeneity due to the fabrication process. From this experiment, we can conclude that the strain is similar in both layers.

To be even more conclusive, we grew a sample with an UL which is supposed to add compressive strain in the QW. This UL was made with InAlN with an indium percentage around 15 % [76]. The improvement of the QW intensity with a 50 nm thick $In_{0.15}Al_{0.85}N$ underlayer is in the same order of magnitude than for an InGaN UL. The InAlN UL is discussed in more detail in Chap. 3 and used in LEDs in Chap. 5. Therefore, the role of the InGaN UL is not to decrease the compressive strain in the InGaN QW.

2.8 Reducing the density of non radiative centers

Hypothesis from the literature

Akasaka *et al.* [56] and Armstrong *et al.* [64] proposed that the InGaN UL reduces the number of NRCs in the QW. Akasaka *et al.*[56] demonstrated that the InGaN UL increases the PL intensity at room temperature. They also analyzed the evolution of the MQW intensity with temperature by performing a fit with the following equation: $I(T) = I_0 / \left(1 + \alpha e^{\frac{-E_a}{k_B T}}\right)$ with I_0 the initial intensity, E_a the activation energy, and α the process rate parameter (proportional to the total number of defects) [56]. They showed that the same activation energy for the NRCs can be found for the samples with and without InGaN UL, but α is 20 times smaller. They concluded that the same NRCs were at play in the two samples, but the density of NRCs is strongly reduced for the QW with an InGaN UL. Furthermore, they tried to replace the InGaN UL by a LT GaN UL without any success hence confirming that indium is needed to increase the QW efficiency.

Armstrong *et al.* [64] worked on two SQW samples: one with an InGaN UL and one without UL. They performed deep level optical spectroscopy and found that deep states are the same in both SQWs. However, for the SQW without UL, a level at $E_c - 1.62$ eV has a density 3.4 times higher than for the sample with an InGaN UL. They concluded that the InGaN UL allows to reduce the density of NRCs in the QW.

Our study

Our previous resonant PL experiments carried out on the samples with and without an InGaN UL are consistent with the hypotheses of Akasaka *et al.* and Armstrong *et al.* [56, 64], who proposed that the InGaN UL reduces the number of NRCs in the QW. To push further the analyses, we performed TRPL on various samples. TRPL gives access to the QW effective lifetime, which is defined as:

$$\frac{1}{\tau_{\text{eff}}} = \frac{1}{\tau_{\text{NR}}} + \frac{1}{\tau_{\text{R}}}, \tag{2.1}$$

with τ_{NR} the NR lifetime and τ_{R} the radiative lifetime. The radiative lifetime depends on the oscillator strength, which should be similar for all the samples as the QW has the same nominal thickness (2.7 nm) and indium content (12 %). The QW effective lifetime, thus depends only on the NR lifetime. Therefore, performing TRPL measurements gives access to a quantitative study of NRCs in the QWs.

The two samples grown on FS-GaN are used for this study, see Fig. 2.2. Thanks to the resonant PL measurements (Fig. 2.5) we know that their indium content is similar and that the localization is the same for both samples. TRPL is performed with a 280 nm laser[2] at 300 K and 15 K, see Figs. 2.11(a) and 2.11(b). The excitation power density was carefully chosen to

---

[2] For information on the TRPL set-up and the laser, see Sec. 1.4.2.

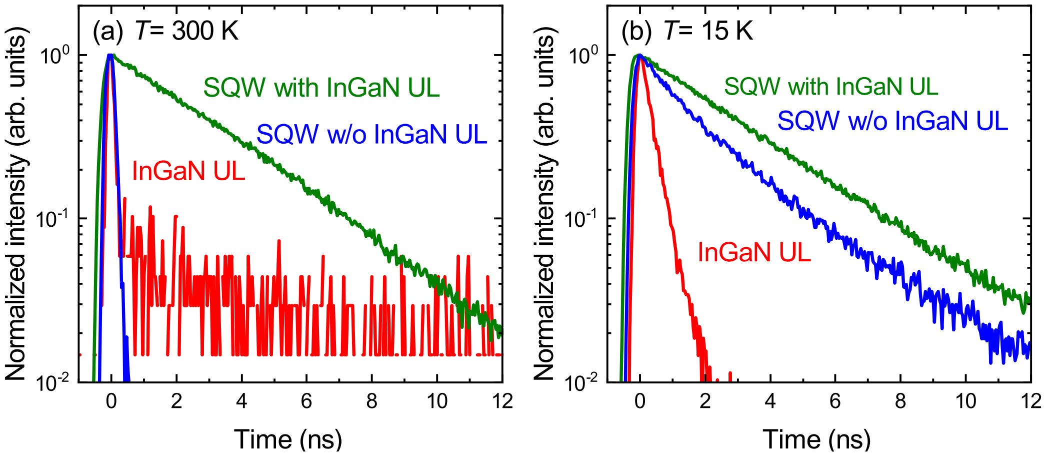

Figure 2.11 – Normalized PL decay of a SQW with an InGaN UL, a SQW without UL, and the UL at 300 K (a) and at 15 K (b). The measurements were performed with an excitation wavelength of 280 nm. The power density is 12 mW/cm^2.

be in a regime where we are sensitive to NR recombination and to avoid any screening of the built-in field. For each curve, the PL decay is fitted with $\alpha \cdot \exp(\frac{-t}{\tau_{\text{eff}}})$ to get the effective lifetime (determined in the early delay). All the effective lifetimes are reported in Tab. 2.1.

T [K]	SQW w/o UL	SQW with an InGaN UL	UL
15	2.1 ns	3.2 ns	0.37 ns
300	0.1 ns	3.3 ns	0.1 ns

Table 2.1 – Effective lifetime for the different curves presented in Fig. 2.11.

At room temperature, the effective lifetime of the SQW with an InGaN UL is longer (3.3 ns) than that of the SQW without InGaN UL (0.1 ns). If we assume that the radiative lifetime is similar for the two QWs, we can conclude that the concentration of NRCs in the QW with an InGaN UL is much smaller than the one in the QW without the InGaN UL, which is consistent with the PL experiments shown earlier and with the papers of Akasaka *et al.* and Armstrong *et al.* [56, 64]. When the temperature is decreased, the NRCs should be inactive. At LT (15 K), the effective lifetime of the two QWs should be similar as the NR lifetime tends to infinity, i.e. the effective lifetime will be close to the radiative lifetime. As expected, the two samples have similar effective lifetime, 2.1 ns and 3.2 ns for the sample without UL and with an InGaN UL, respectively. The difference between the two effective lifetimes can come from the fact that, at 15 K, NRCs are still active.

More interestingly, we notice that the InGaN UL effective lifetime is identical to the one of the SQW without UL (0.1 ns in both cases). This can be the sign that we are dealing with the same NRCs in the SQW and the InGaN UL. We can thus conclude that the InGaN UL is used to bury some kinds of point defects in it, as proposed by Armstrong *et al.* [64].

Hypothesis	Our conclusion:	Argument:
Injection efficiency [57, 58, 60, 62]	No	• InGaN UL improves the PL signal of a SQW under resonant pumping
Reduction of threading dislocations [61]	No	• Our data shows an increase of the pit density in the presence of an InGaN UL • The UL also improves SQWs grown on FS-GaN
Formation of V-pits [71]	No	• SQW efficiency is also improved by an InGaN UL when grown on FS-GaN
Step edge morphology	No	• AFM measurements
Layer localization	No	• PL energy vs temperature
Electric field reduction [37, 63, 65]	No	• InGaN UL still efficiently improves the SQW emission after a thick spacer
Strain mitigation [59, 73, 74]	No	• Strain measurements by PL show a similar strain state for samples with and without UL • Tensile InAlN layer also works as an efficient UL
Decrease in NRCs [56, 64]	Yes	• Confirmed by TRPL

Table 2.2 – Summary of each hypothesis studied in this chapter with the main mechanism behind the QW improvement due to the presence of an InGaN UL with the arguments we used to draw a conclusion.

Summary

After reviewing all the hypotheses present in the literature, we can conclude that the most convincing one is that the InGaN UL is used to bury point defects, which in turn create NRCs in indium-containing layers [77]. The nature of these defects will be discussed in chapter 4, where we will show inconclusive SIMS measurements for several impurities and the possible intrinsic nature of those defects. We propose that the same defects are present at the growth surface and are incorporated in the InGaN UL or in the InGaN QW. These detrimental point defects are called surface defects (SDs) hereafter.

3 Capture of surface defects by indium

In the previous chapter, we discussed several hypotheses present in the literature and we concluded that the mechanism leading to the improvement of the InGaN QW efficiency is the burying of points defects in the InGaN UL. In this chapter, we explore the impact of different UL parameters such as the choice of material, thickness, and composition. Our findings indicate that surface defects (SDs) interact with In atoms and then get buried. We propose a model that quantifies this mechanism.

3.1 Experimental evidence of the capture mechanism

To get the full picture of the capture mechanism of SDs, we designed four sample series where we varied different parameters, see Fig. 3.1. These different sample series were grown in two MOVPE reactors (one horizontal and one vertical), and on two types of substrates (FS-GaN and GaN on sapphire template). The difference between the vertical reactor (or showerhead reactor) and the horizontal reactor, except for their geometry, is the materials which are present in the growth chamber. In the vertical reactor (reactor 1), the showerhead is made of stainless steel. Stainless steel could release some impurities like iron during growth, which could be incorporated in the samples. In the case of the horizontal reactor (reactor 2), a quartz liner is used. If the UL has a similar effect in both cases, we can deduce that SDs are reactor independent. We have also chosen to use two different type of substrates, FS-GaN and GaN on sapphire template. In the previous chapter, we already showed that the InGaN UL works in the same way whatever the substrate type, i.e., whatever the dislocation density.

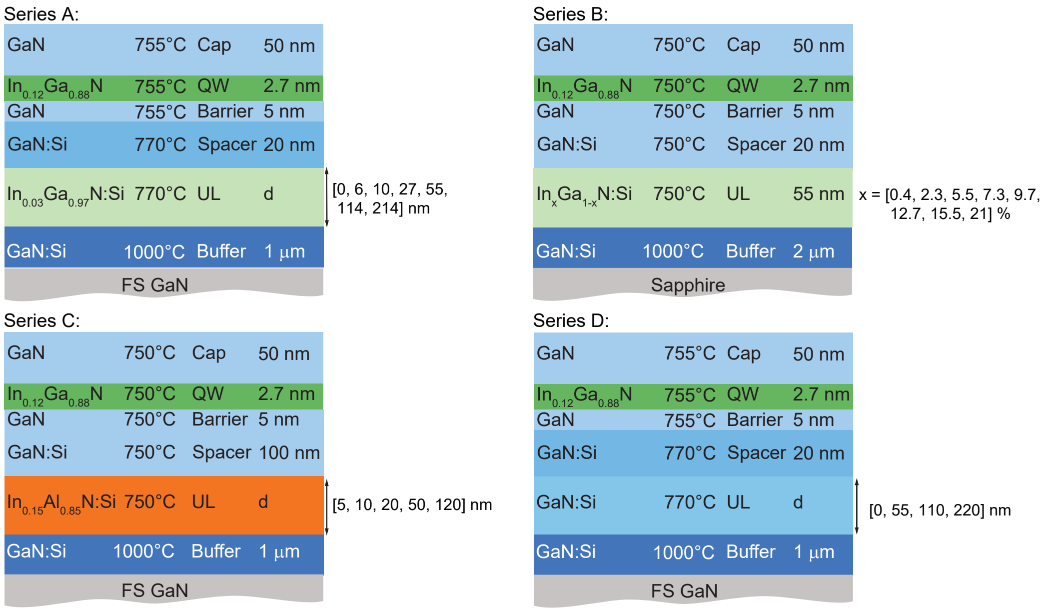

Figure 3.1 – Sample structure used in this chapter. Four series of samples were grown. The doping level in all the series is $3 \cdot 10^{18}$ cm^{-3}, and the reactor used for series A and D was the vertical reactor. The horizontal reactor was used for series B and C. The different parameters are indicated on the figure. For the 120 nm thick InAlN UL, the UL consists of four 30 nm thick InAlN layers separated by 5 nm thick GaN interlayers.

3.1.1 InGaN underlayer thickness

The first parameter, we explore, is the thickness of the InGaN UL. Sample series A is designed with the same indium content in all the InGaN ULs (around 3 %), and we varied the thickness of the UL from 0 to 214 nm, see Fig. 3.1, series A.

Samples growth

For this samples series, we used the showerhead reactor and FS-GaN substrates. The growth starts with a 1 μm thick GaN buffer grown at 1000 °C using TMGa and H_2 as carrier gas, doped at $3 \cdot 10^{18}$ cm^{-3}. Then the temperature is decreased to 770°C and the carrier gas is switched to N_2 and the GaN precursor to TEGa. The InGaN:Si UL thickness is varied from 0 to 214 nm, while the indium composition is nominally equal to 3%. A 20 nm thick GaN:Si spacer is inserted between the UL and the QW. The top part of the sample is grown at 755°C and consists of an undoped GaN barrier of 5 nm, a 2.7 nm thick InGaN QW, and a 50 nm thick GaN cap.

The thickness and composition were extracted from HRXRD analysis performed on each sample. Small variations in the In content of the UL are present due to the temperature repeatability of the MOVPE. Indeed, one degree centigrade of temperature variation will change the indium composition by ~ 1.5%. However, variations are usually rather small, and

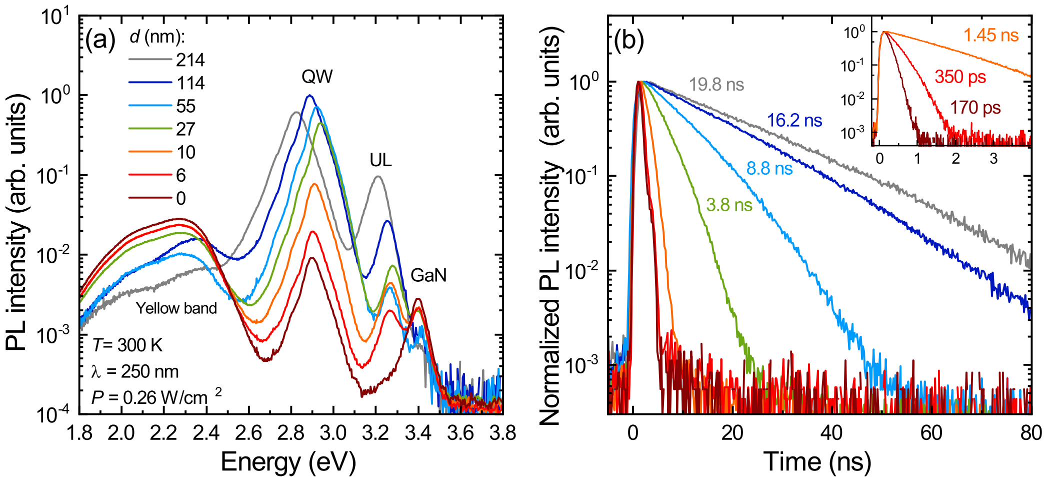

Figure 3.2 – (a) PL spectra measured at 300 K for series A. Each curve corresponds to a different InGaN UL thickness. (b) Normalized QW PL decay traces recorded at 300 K which correspond to the spectra shown in (a). The time window is 80 ns and 4 ns for the inset, respectively.

the composition in indium of the InGaN UL is ranging between 3.2 % and 4.5 % with an average around 3.4 %. For the InGaN QW, similar variations can also be observed which will have an impact on the QW peak energy. The QW peak position occurs between 2.82 and 2.93 eV for the two extremes, which corresponds to a variation in indium content around 2 %.

Results

For the measurements shown in this chapter, we used a 280 nm pulsed laser to get access to PL and TRPL data. This laser is pumping the samples non-resonantly, i.e., above the GaN barrier bandgap. To limit as much as possible potential side effects, the thickness of the cap, the QW, and the spacer were kept the same for all the samples. By doing so, the number of photogenerated carriers injected in the SQW should be similar for a given power density. We also cared about the carrier density which was low enough to avoid any built-in electric field screening. For a power density of 0.26 W/cm^2, the injected carrier density[1] is estimated around 10^{11} cm^{-2} in the QW, which is one order of magnitude lower than the carrier density for which screening of the built-in electric field occurs ($\sim 10^{12}$ cm^{-2}) [80, 81].

The PL spectra for each sample are displayed, in Fig. 3.2(a). Four peaks can be observed and attributed to: the YB, the InGaN QW, the InGaN UL, and the GaN band edge emission. The peak of interest is the QW peak as its intensity is proportional to its efficiency assuming the same extraction efficiency for all the samples. The maximum intensity of the QW emission

---

[1] We estimated the carrier density in the QW, from the power density and the absorption into the cap, the InGaN QW, and the spacer, $n = n_{\text{photon}} \cdot (1 - R)(1 - e^{-\alpha \cdot (d_{\text{QW}} + d_{\text{cap}} + d_{\text{spacer}})})$, with n_{photon} the photon density at the surface, R the GaN reflectivity at the pumping wavelength (~0.2 [78]), α the GaN absorption coefficient (1.5×10^5 cm^{-1} [79]), and $d_{\text{QW, cap, spacer}}$ the thickness of the cap, of the QW, and of the spacer, respectively.

increases with the thickness of the InGaN UL for an UL thickness up to 115 nm. Then it slightly decreases for the sample with a 214 nm thick InGaN UL. Note that the QW and the UL peaks for the 214 nm thick UL sample are slightly redshifted. For this sample, we remarked afterward that the growth temperature, for both the InGaN QW and the InGaN UL, was lower (5 °C) than for the other samples, which leads to a small increase in the indium content (4.5 % in the InGaN UL instead of 3.4%). As the 214 nm InGaN UL is rather thick, we checked for any relaxation by XRD RSM analysis. No signs of relaxation were evidenced which is in line with the results of M. Pristovsek [82].

In Fig. 3.2(a), the emission of the InGaN UL grows with the UL thickness while the GaN band edge intensity decreases. This is related to the probed region by the 280 nm laser. Typically, for the sample with a 5 nm thick UL about 25 % of the initial laser power reaches the GaN buffer. In the case of the sample with a 214 nm thick UL, this number is reduced to 0.5%. This explains the decrease in the GaN band edge and the YB emission.

The QW PL decay is measured at 300 K with the spectral window centered on the QW maximum and is sharp enough to avoid the contribution from the YB or the InGaN UL. Normalized PL decay for the QW peak is reported in Fig. 3.2(b). Note that for a long delay, PL decays exhibit a nonexponential behavior. Similar observations have been made on bulk GaN substrates at room temperature [83] and attributed to the slow dynamics of NRCs. The effective lifetime is extracted from the fit of the first part of the decay. As for the QW intensity, the effective lifetime increases with the InGaN UL thickness (from 170 ps to 19.8 ns) (Fig. 3.3). With an InGaN UL of only 50 nm, the effective lifetime is multiplied by almost two orders of magnitude (from 170 ps to 8.8 ns). Then, the effective lifetime starts to saturate, and the increase of the InGaN UL thickness has no more impact.

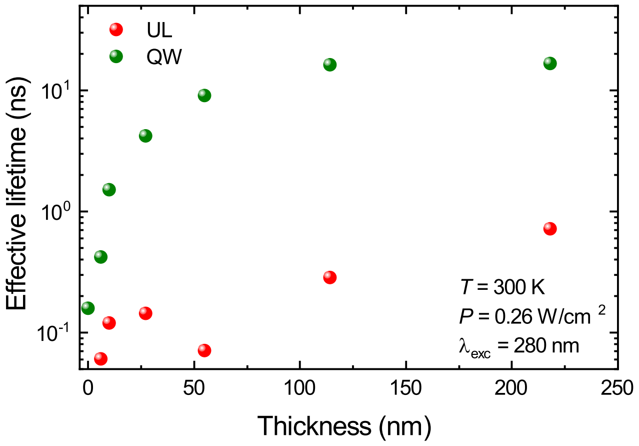

Figure 3.3 – Dependence of the effective lifetime with UL thickness for the InGaN UL (red dots) and the SQWs (green dots).

The effective lifetime is composed of the radiative lifetime and the NR lifetime, see Eq. (2.1). As the InGaN QW is always the same, the radiative lifetime for these samples, which depends on the oscillator strength, is similar. The only parameter which changes is the NR lifetime. Therefore, we can conclude that the NR recombination reduces when the UL thickness increases.

One can remark that the effective lifetime of the QW without InGaN UL is similar to the values measured in thin ULs, around 100 ps (Fig. 3.3). Also, it is worth pointing out that the carrier lifetime in the InGaN UL starts to increase when the effective lifetime of the QW does not increase anymore. This indicates that the top part of the InGaN UL gets improved too. From these observations, one may postulate that the NRCS in the QW and in the UL have the same origin as already proposed in the previous chapter. We will see that the NRCs are introduced by the presence of species at the growth front which are incorporated in InGaN layers.

3.1.2 InGaN underlayer composition

The sample series B was grown with a fixed InGaN UL thickness (50 nm) and the indium composition was varied inside the UL from 0 to 21 %, see Fig. 3.1.

Samples growth

For this series, we chose to use the horizontal reactor. We also changed the substrate to GaN on sapphire templates. The structure of the sample is the following. First, a GaN:Si buffer of 2 μm is grown under H_2 with TMGa at a temperature of 1000 °C. The doping level was $3 \cdot 10^{18}$ cm^{-3}. Then, the temperature is reduced to 750°C. Usually, for such a growth temperature we expect a rather high indium content (up to 15%). To control the indium incorporation, the 50 nm thick InGaN:Si UL was grown with a mixture of N_2 and H_2. H_2 is known to reduce the indium composition. Therefore, a high H_2 flux leads to an UL with a low indium content and when the H_2 flux is reduced the indium content increases. TEGa and TMIn were used for the growth of the InGaN UL. A spacer of GaN:Si is grown to separate the QW and the UL with TEGa, followed by an undoped GaN barrier of 5 nm. On top, a 2.7 nm thick InGaN QW is deposited. A 50 nm GaN cap layer completes the structure.

Finally, one should point out that the growth conditions for the thickness series and the composition series are significantly different, as are the growth reactors.

Results

On this series of samples, PL and TRPL measurements are performed with the same 280 nm pulsed laser as for series A. However, as samples are grown on sapphire template, the overall efficiency is lower, and the power was slightly increased to get a clear signal from the QW. Room temperature PL spectra are displayed in Fig. 3.4(a). Three clear peaks can be distinguished: the QW emission around 2.82 eV, the GaN band edge around 3.41 eV and the YB around 2.2 eV. The additional peak for each curve, which is redshifting with the indium composition, is the UL emission. As samples are grown on a GaN on sapphire template, the PL emission experiences some modulation due to internal reflections between the surface and the sapphire/buffer interface which acts as a Fabry-Perot cavity. Fig. 3.4(a) shows that the PL intensity gets higher when the In composition increases. The GaN band edge intensity decreases with the composition which is due to the laser absorption, as explained in the last section. A saturation effect can be observed for a composition higher than 9 %. One can notice that the sample with an InGaN UL at 21 % has an intensity almost as low as the sample without UL. Due to the thickness of the InGaN UL and the high indium content, the layer relaxes [82], thus introducing extended defects in the QW.

The effective lifetime is extracted from the PL decay curves as in the previous section. The QW effective lifetime is following the same trend as the QW PL intensity, see Fig. 3.4(b) and inset. An increase of the effective lifetime with indium composition by two orders of magnitude with a saturation after 9% is observed. The exception is the sample with a composition of 21 %, which is relaxed, where the effective lifetime decreases to 250 ps. As the QW is always the same, we can assume that the only parameter which changes is the NR lifetime, i.e. the concentration of NRCs in the QW. In Fig. 3.4(a), we observe a spectral shift in the QW emission peak without any clear correlation between the effective lifetime and the QW peak energy. This shift could be due to small fluctuations of the growth temperature leading to a change in the indium content of the QW. Nevertheless, the impact on the wave-function overlap is a variation of 10% at most, which is not sufficient to account for the observed difference in the effective lifetime, which varies by more than one order of magnitude (from 24 ps to 3.8ns). These results show a clear correlation between the QW efficiency and the In content in the UL.

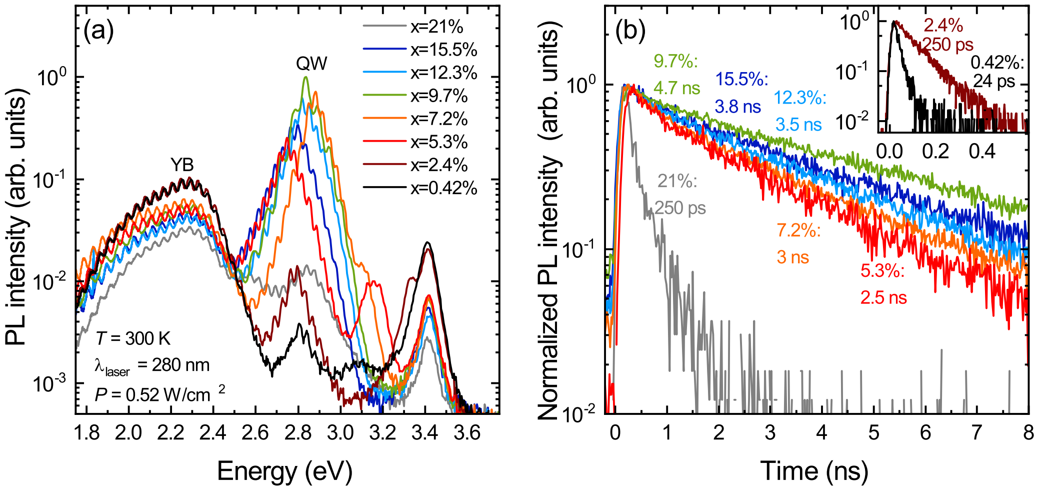

Figure 3.4 – (a) PL spectra measured at 300 K for sample Series B. Each curve corresponds to a different InGaN UL composition. (b) Normalized QW PL decay traces which correspond to the spectra shown in (a). The time window is 8 ns and 0.4 ns for the inset, respectively.

3.1.3 Low temperature GaN underlayer

The thickness and composition studies have in common the presence of In in the UL. We thus decided to replace the InGaN UL grown at 770 °C by a GaN layer grown at the same temperature, see Fig. 3.1.

Sample growth

For this sample series, we used the vertical reactor and the substrate was FS-GaN. A GaN:Si buffer of 1 μm is grown at 1000 °C with TMGa and H_2 as carrier gas. Then the temperature is decreased to the InGaN UL temperature (770°C), and GaN:Si UL of different thicknesses, (55, 110, and 220 nm) are grown with TEGa and N_2 as carrier gas. As for the other series, a 20 nm thick GaN:Si spacer is deposited at the same temperature. Then the temperature is decreased to 750 °C to grow the top part of the sample which consists of an undoped 5 nm thick GaN barrier, a 2.7 nm thick InGaN QW, and a 50 nm thick GaN cap.

Results

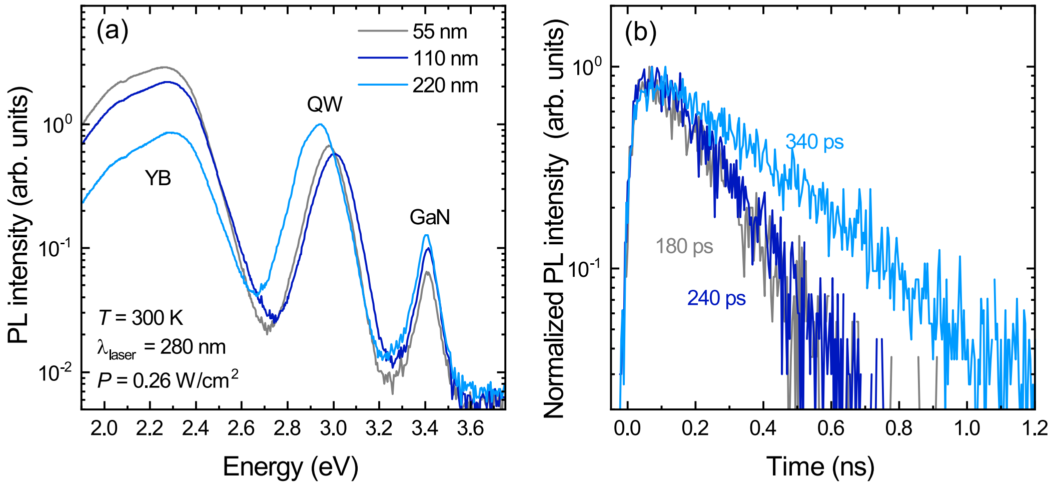

Figure 3.5 – a) PL spectra measured at 300 K for sample series D. Each curve corresponds to a different GaN UL thickness. (b) Normalized QW PL decay traces which correspond to the spectra shown in (a). The time window is 1.2 ns.

PL measurement at room temperature are performed on these samples, see Fig. 3.5(a), with the same 280 nm pulsed laser, and the same power density as for series A. As for the other samples, the YB, the QW, and the GaN emission are clearly separated, and the behavior for the YB is similar to the case of series A due to the laser absorption. For the QW emission, the intensity increases slightly for the 220 nm thick GaN UL but the effect is less pronounced than in the case of the InGaN UL. Accordingly, the effective lifetime is slowly increasing with the GaN thickness from 180 ps to 340 ps. For the 214 nm thick $In_{0.03}Ga_{0.97}N$ UL, the effective lifetime is 19.8 ns (see Fig. 3.2(b)) compared to only 340 ps for the 220 nm thick LT GaN UL.

This small effect of the GaN UL is in line with the results shown by Akasaka *et al.* [56]. The negligible effect of the LT GaN UL rules out another potential role of the InGaN UL, which is to move away the interface where the temperature change takes place as far as possible from the QW. In MOVPE, growth interruption is known to be detrimental due to the accumulation of impurities at the surface which could in turn create NRCs.

3.1.4 InAlN underlayer

If indium is the key ingredient to explain the positive improvement of the InGaN UL on the QW efficiency, any indium-rich alloy should act in the same way. In the case of the InGaN UL, to avoid any absorption of the blue light emitted by the QWs, a low indium content is used. However, InAlN has the particularity to be LM to GaN for a composition of 17%,[76], which opens interesting perspectives for high indium content UL with almost no relaxation issue and a low parasitic absorption as the bandgap for LM InAlN is equal to 4.5 eV [84]. The specificities of the InAlN alloy are discussed in more detail in Chap. 5.

For these samples, we chose on purpose a slightly lower indium content (15 %). Note that InAlN is under slight tensile strain with this composition, contrary to the standard compressively strained InGaN UL. The $In_{0.15}Al_{0.85}N$ thickness is varied from 5 to 120 nm, see Fig. 3.1, series C.

Sample growth

This series was grown on FS-GaN substrates in the horizontal reactor. We used the horizontal reactor to avoid any parasitic gallium incorporation in the InAlN alloy due to memory effects present in the vertical reactor with the showerhead [85, 86]. As always, the first layer is a GaN:Si buffer of 1 μm with a doping level of $3 \cdot 10^{18}\text{cm}^{-3}$. We used TMGa and H_2 as carrier gas for the buffer. Then, the temperature is decreased to 750°C to allow indium incorporation and the carrier gas is switched to N_2. An $In_{0.15}Al_{0.85}N$:Si UL is grown with TMAl and TMIn. Then a 100 nm thick GaN:Si spacer is deposited with TEGa. The top part of the samples (cap, QW, barriers) is similar to the other series.

Notice that the spacer thickness is 100 nm in the present series compared to 20 nm for the other series. This is due to the strong polarization mismatch between GaN and the InAlN alloy [87]. To avoid any changes in the built-in field in the QW due to the band bending, a 100 nm thick GaN:Si spacer is introduced. This thickness was chosen based on simulations realized with the commercial software NextNano.

The last sample of this InAlN series with an UL of 120 nm consists of four 30 nm thick InAlN layers separated with a 5 nm thick GaN spacer instead of a thick layer of 120 nm. This is to avoid surface kinetic roughening which occurs in InAlN layers thicker than 50 nm [88]. We will discuss this issue in more details in Chap. 5.

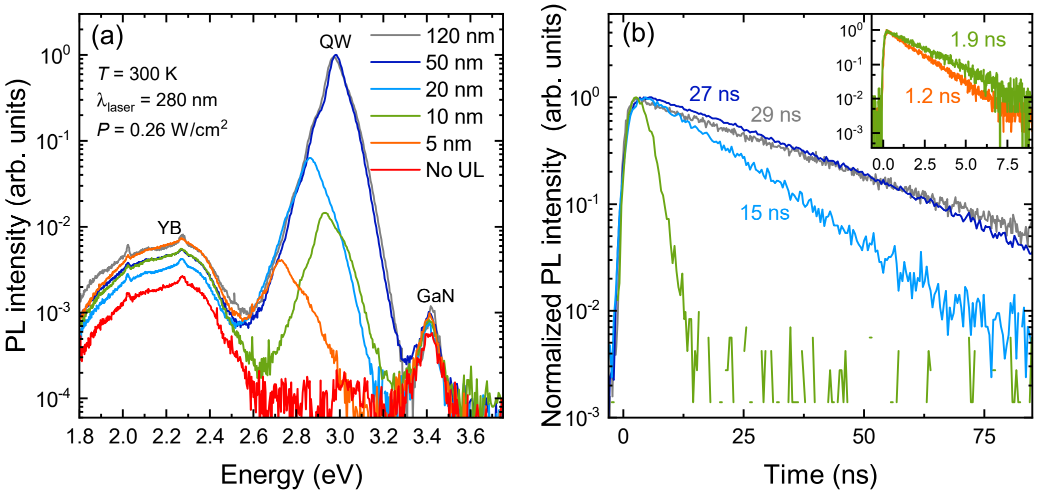

Figure 3.6 – (a) PL spectra measured at 300 K for sample series C. Each spectrum corresponds to a different InAlN UL thickness. (b) Normalized QW PL decay traces which correspond to the spectra shown in (a). The time window is 80 ns and 8 ns for the inset, respectively.

Results

PL and TRPL experiments are performed on the InAlN UL thickness series at room temperature. The excitation wavelength and the laser power density are the same as for prior studies. We do not observe the InAlN UL emission (Fig. 3.6(a)) ,as its bandgap is around 4.5 eV which is higher than our excitation energy [84]. Note that the YB intensity remains roughly constant in this case, which due to the $In_{0.15}Al_{0.85}N$ UL being transparent to the laser. A strong enhancement of the QW intensity can be observed for thick InAlN ULs, as in the case of InGaN UL. However, a saturation of the QW intensity is observed after 50 nm,instead of 110 nm for InGaN UL.

For a given thickness, the InAlN UL outperforms the InGaN UL for an equal thickness (Fig. 3.6(b)). As an illustration, the 50 nm thick InAlN UL sample exhibits a QW effective lifetime of 27 ns, to be compared to 8.8 ns for the 55 nm thick InGaN UL. The effective lifetime as a function of the InAlN thickness is reported in Fig. 3.7(d).

In the literature, some papers proposed that the role of the InGaN UL is to relax the strain in the QW, and thereby increase its efficiency. However, the results obtained with a tensely strained $In_{0.15}Al_{0.85}N$ UL rules out this hypothesis.

3.2 Modeling of the interaction of surface defects with In atoms

The QW effective lifetimes deduced from all previous studies are displayed in Fig. 3.7. A similar trend can be observed for the increase in indium composition or for an increase in the UL thickness when indium is present. For pure GaN, the effective lifetime increases only marginally. We therefore propose that SDs react with In atoms and then get incorporated in the layer. Once buried, they form NRCs, which decreases the QW efficiency. Another observation is that SDs are gradually incorporated, i.e., they seem to segregate.

With these considerations in mind, we developed a model based on surface segregation [89]. SDs segregate at the surface with a surface concentration given by:

$$[\mathrm{SD}] = \theta_0 R^N, \tag{3.1}$$

with θ_0 the initial SD density after the HT GaN growth, R the segregation coefficient and N the number of MLs of the UL. The numbers of MLs is given by $N = d/e_{\mathrm{ML}}$, where e_{ML} is the ML thickness which is computed with Vegards law, and d is the UL thickness extracted from HRXRD measurements. In the case of a GaN UL, the SDs are not buried efficiently in the UL, i.e., the segregation coefficient R is close to 1. When indium is present in the layer, SDs start to incorporate and R decreases. We also define an interaction efficiency, p, between the indium content and the SDs, such as:

$$R = R_{\mathrm{GaN}} - xp, \tag{3.2}$$

with R_{GaN} the SD segregation coefficient in GaN, and x the In composition of the InGaN or the InAlN layer. By substituting R in Eq. (3.1), the density of SDs after the InGaN UL is:

$$[\mathrm{SD}] = \theta_0 (R_{\mathrm{GaN}} - xp)^{d/e_{\mathrm{ML}}}. \tag{3.3}$$

The effective lifetime is expressed as a function of the NR lifetime and the radiative lifetime, see Eq. (2.1). We assume that the NR lifetime can be split into two parts:

$$\frac{1}{\tau_{\mathrm{eff}}} = \frac{1}{\tau_{\mathrm{R}}} + \frac{1}{\tau_{\mathrm{NR,0}}} + \frac{1}{\tau_{\mathrm{NR,SD}}}, \tag{3.4}$$

with $\tau_{\mathrm{NR,0}}$ the NR lifetime which accounts for the impact of dislocations, impurities and all other NR processes limiting the QW efficiency, and $\tau_{\mathrm{NR,SD}}$ the NR lifetime depending only on the NRCs introduced by SD in the QW. As our data do not allow us to separate τ_{R}, and $\tau_{\mathrm{NR,0}}$, we defined the effective lifetime τ_0 which is the effective lifetime for a QW free of SD related NRCs [SD]: $\left(\frac{1}{\tau_0} = \frac{1}{\tau_{\mathrm{R}}} + \frac{1}{\tau_{\mathrm{NR,0}}}\right)$. With this definition and Eq. (3.4), the effective lifetime can be written as:

$$\tau_{\mathrm{eff}} = \frac{\tau_0 \tau_{\mathrm{NR,SD}}}{\tau_0 + \tau_{\mathrm{NR,SD}}}. \tag{3.5}$$

The second hypothesis is that $\tau_{\mathrm{NR,SD}}$ is inversely proportional to [SD] in the QW, $\frac{1}{\tau_{\mathrm{NR,SD}}} = C_{n,p}[\mathrm{SD}]_{\mathrm{QW}}$. $C_{n,p}$ corresponds to the electron/hole capture coefficient of the NRCs induced by SDs. $[\mathrm{SD}]_{\mathrm{QW}}$ depends on the SD density present just before the QW, $[SD]$, see Eq. (3.1), and

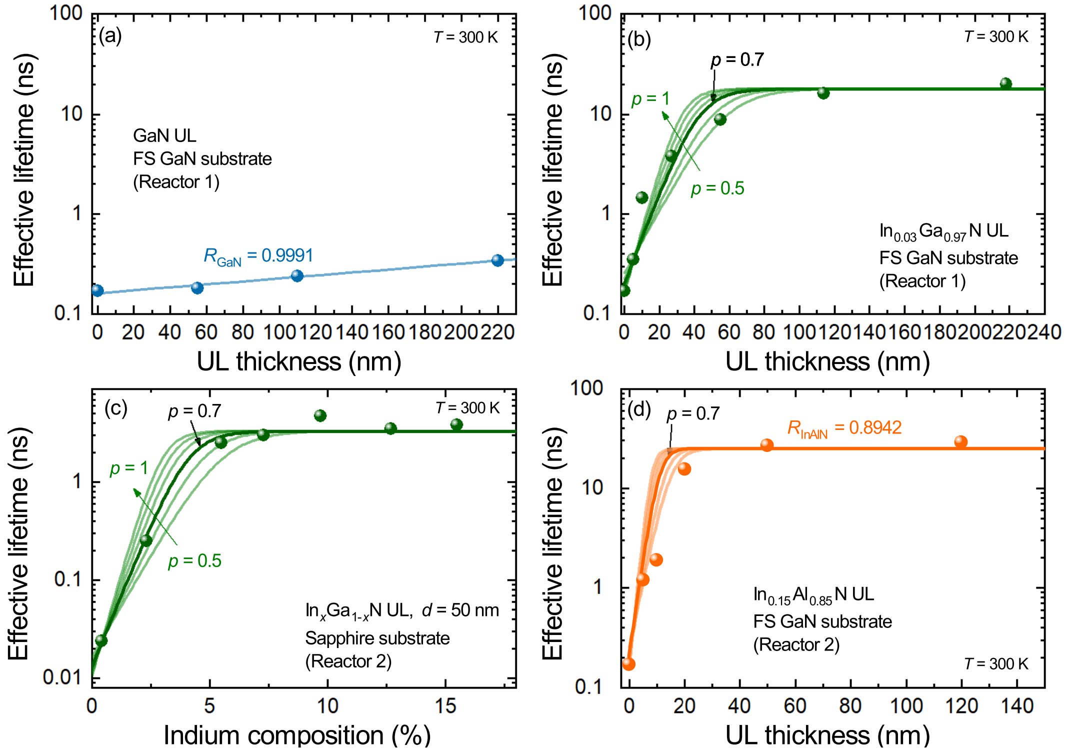

Figure 3.7 – Measured QW effective lifetimes for the different sample series. The darkest line is the model with a p value equal to 0.7 and the others are with p changing from 0.5 to 1.

the capture coefficient of the QW itself, $C_{\mathrm{QW}} = (1-(R_{\mathrm{GaN}} - x_{\mathrm{QW}}p)^{N_{\mathrm{QW}}})/L_{\mathrm{QW}}$. The QW capture coefficient depends on the QW indium content, x_{QW}, the thickness of the QW, L_{QW}, and the ML number of the QW, N_{QW}. Finally, the expression for the QW effective lifetime is:

$$\tau_{\mathrm{eff}} = \tau_0 \frac{1}{1+\tau_0 C_{n,p}\theta_0 (R_{\mathrm{GaN}} - xp)^N C_{\mathrm{QW}}}. \tag{3.6}$$

For the sake of simplification, we introduce the parameter α, with $\alpha = C_{n,p}\theta_0 C_{\mathrm{QW}}$. With the help of HRXRD, C_{QW} can be deduced. However, θ_0 and $C_{n,p}$ can not be found independently. As the QWs always have the same indium content (~12 %), C_{QW} is fixed.

R_{GaN} is deduced by fitting the data of the sample series with the GaN UL, see Fig. 3.7(a), (all the parameters can be found in Tab. 3.1). As expected, R_{GaN} is close to unity, 0.9991, meaning that only a few defects are incorporated into LT GaN. To reach a similar efficiency than a 110 nm thick $In_{0.03}Ga_{0.97}N$ UL, the LT GaN UL should reach a 2 μm thick value according to our model. Of course, thick LT layers will be problematic as the growth time will be much longer and strong meandering will appear [90]. In fact, the sample with a 220 nm thick LT GaN UL shows already some surface roughening when probed by HR-XRD.

Once R_{GaN} is determined, we can fit the other data simply using the In composition in the UL and adjusting the p. Several values for p were considered. The best fit for all the different series is obtained with a p parameter of 0.7. For the InGaN thickness series, the correspondence between the model and the data is less good than for the composition series, see Figs. 3.7(c) and 3.7(c). This might be explained by the larger sensitivity of the effective lifetime to the fluctuation of the NRCs when the QWs are grown on FS-GaN due to the longer τ_0. Notice that for the InGaN composition series (grown on GaN on sapphire template), τ_0 is shorter due to the large density of dislocations (10^8 cm^{-2} on sapphire versus 10^6 cm^{-2} on FS-GaN), which could increase the density of NRCs.

The most striking result is that the effective lifetime of the QW can be well reproduced by the model considering the In composition and $p = 0.7$. This validates our assumption that SDs get progressively buried when reacting with In atoms, generating in turn NRCs.

Sample series	τ_0 [ns]	C_{QW} [cm^{-1}]	$C_{n,p}\theta_0$ [cm s^{-1}]	$\alpha = C_{n,p}\theta_0 C_{QW}$ [s^{-1}]	$R = R_{GaN} - xp$
Series D: LT GaN UL thickness	18	$2.7 \cdot 10^6$	$2.2 \cdot 10^3$	$4.8 \cdot 10^9$	0.9991
Series A: InGaN UL thickness	18	$2.7 \cdot 10^6$	$2.2 \cdot 10^3$	$4.8 \cdot 10^9$	0.9782
Series B: InGaN UL composition	3.3	$2.7 \cdot 10^6$	$4.1 \cdot 10^4$	$8.9 \cdot 10^{10}$	-
Series C: InAlN UL thickness	25	$2.7 \cdot 10^6$	$2.2 \cdot 10^3$	$4.8 \cdot 10^9$	0.8942

Table 3.1 – Values of the parameters used in Fig. 3.7 for an interaction efficiency $p = 0.7$ for the different sample series. R is computed with Eq. (3.2).

The segregation coefficients for $In_{0.03}Ga_{0.97}N$ and $In_{0.15}Al_{0.85}N$ ULs are reported in Tab. 3.1. In the case of InAlN, as the indium concentration is higher, i.e., 15% instead of 3%, R is significantly lower, 0.8942, instead of 0.9782 for $In_{0.03}Ga_{0.97}N$. Therefore, only a thin layer (~30 nm) of InAlN is needed to capture all SDs initially present. InAlN UL could be of interest for NUV LEDs, see Chap. 5.

Effective thickness approximation

We have seen that the amount of In in the UL is the key parameter. We propose in this part to simplify Eq. (3.6), to define an "effective thickness", $d_{\text{eff}} = x_{In} \cdot d_{\text{UL}}$, with d_{UL} the thickness of the UL. Indeed, Eq. (3.3) can be rewritten by setting $R_{\text{GaN}} \approx 1$:

$$[\text{SD}] = \theta_0 (R_{\text{GaN}} - xp)^{d/e_{\text{ML}}} = \theta_0 e^{d/e_{\text{ML}} \ln(R_{\text{GaN}} - xp)} \approx \theta_0 e^{d/e_{\text{ML}} \ln(1-xp)}. \tag{3.7}$$

Using a first order expansion for xp close to 0, it becomes:

$$[\text{SD}] \approx \theta_0 e^{-\frac{d_{\text{UL}}}{e_{\text{ML}}} xp} = \theta_0 e^{-\frac{d_{\text{eff}}}{e_{\text{ML}}} p}. \tag{3.8}$$

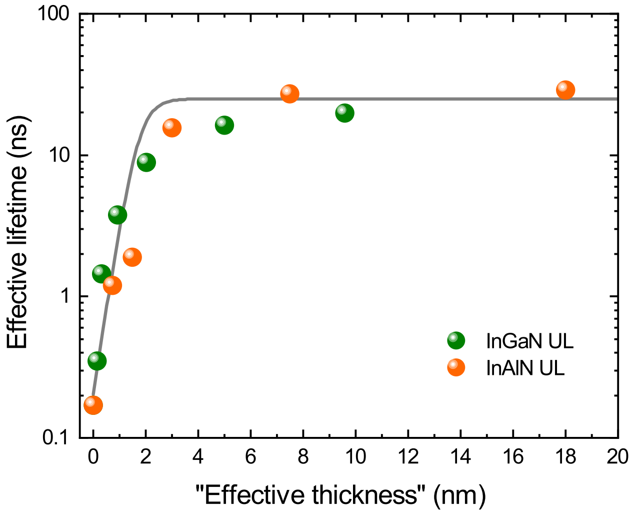

Figure 3.8 – Effective lifetime at room temperature as a function of the "effective thickness" d_{eff} for all series grown on FS-GaN. The gray line is obtained from Eq. (3.9) with $\alpha = 4.8 \cdot 10^9$ s^{-1}, $\tau_0 = 25$ ns, and $p = 0.7$.

With this equation, the effective lifetime can be written as:

$$\tau_{\mathrm{eff}} \approx \tau_0 \frac{1}{1 + \tau_0 C_{n,p} \theta_0 e^{-\frac{d_{\mathrm{eff}}}{e_{\mathrm{ML}}} p} C_{\mathrm{QW}}}. \tag{3.9}$$

This approach is interesting as it allows to compare on the same graph InGaN and InAlN UL having a different indium composition.

In Fig. 3.8, all the effective lifetimes of the sample series A and C are plotted as a function of the effective thickness. The gray line is computed from Eq. (3.9), with $\alpha = 4.8 \cdot 10^9$ s^{-1}, $\tau_0 = 25$ ns, and $p = 0.7$, which are the same parameters than the ones used in Fig. 3.7. All the data points are following the same trend, even if two different reactors and materials are used for the same substrate (FS-GaN).

3.3 Discussion on the role of multiple quantum wells

Most of the LEDs have an active region with MQWs (5-10 QWs). According to our model, SDs should be gradually incorporated in the QWs, i.e., the QW near the n-side should contain much more NRCs than the one on the p-side. Therefore, the first QWs should act as an InGaN UL by capturing SDs and hence the next QWs should have less NRCs. This allow us revisiting some papers.

A study done on three similar samples, one with an InGaN SQW, one with 5 InGaN QWs

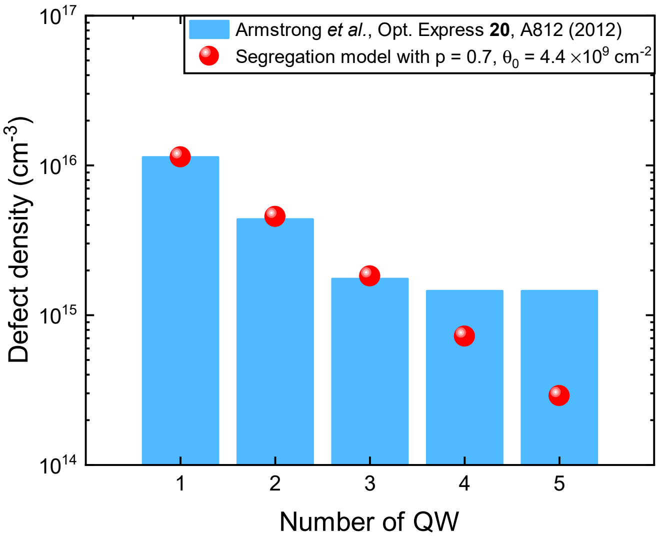

Figure 3.9 – Defect density as a function of the number of QWs. The blue bars correspond to the density of the deep level, $E_c - 1.62$ eV, discussed in Armstrong *et al.* [93]. The red dots correspond to the computed density of SDs using Eq. (3.10).

and one with 10 InGaN QWs, was realized by Minsky *et al.* in 1998 [91]. They performed TRPL measurements on these structures and showed that at 4 K all the structures exhibit an effective lifetime around 1 to 2 ns. When the temperature increases, the sample with an InGaN SQW shows an effective lifetime dropping to 60 ps at 300 K. For the two other samples, the effective lifetime is longer, 0.5 ns and 1.4 ns for the 5 QW nd 10 QW samples, respectively. The corresponding IQE is 0.37 % for the SQW and 30% for 10 QWs sample, respectively. As an explanation, the Authors proposed a decrease in the NRCs and an increase in the composition fluctuation [91]. These results are consistent with the physical mechanism we proposed in this chapter. Indeed, one can expect that the first few QWs trapped SDs, i.e., are full of NRCs, and when the QW number is sufficient the top QWs are free from SDs thus have a better IQE. Chichibu *et al.* performed TRPL measurements on a MQW structure (5 InGaN QWs) and a SQW structure and found that MQWs have a longer lifetime at room temperature and a smaller IQE dependence with temperature [92], which is also in line with our results.

Armstrong *et al.* studied the density of deep levels present in InGaN MQWs in 2012 [93]. They highlighted the fact that the first QW has more defects than the following ones (for a sample without any UL before the QWs). Their sample is made of five 2.5 nm thick $In_{0.13}Ga_{0.87}N$ QWs and they carried out deep level optical spectroscopy to determine the different defect levels and get an idea of the concentration of each trap. They found out 2 deep levels in the QWs positioned at $E_c - 1.62$ eV and $E_c - 2.76$ eV. The level $E_c - 1.62$ eV is interesting as it is the one for which they observed a reduction when an InGaN UL is added [64]. In Fig. 3.9, the $E_c - 1.62$ eV defect density observed by Armstrong *et al.* is reported for each of the QWs, blue bars. For the first QW grown, the density is close to 1×10^{16} cm^{-3}. Then, the density decreases with the growth of each QW. The 4th and the 5th QW have the same density as they were not able experimentally to separate the two QWs [93]. We know that the SD density, [SD], diminishes after each QW and that part of the SDs is buried in the QW. The density of SDs buried in the QWs, $i = 1, 2, \ldots$, can be written as:

$$[\mathrm{SD}]_{\mathrm{QW},i} = \theta_{i-1}(1-(R_{\mathrm{GaN}} - x_{\mathrm{QW}}p)^{N_{\mathrm{QW}}})/L_{\mathrm{QW}}, \tag{3.10}$$

with θ_i the SD surface density before the QW number i:

$$\begin{aligned} &\theta_0, && i = 0, \\ &\theta_i = \theta_{i-1} - [\mathrm{SD}]_{\mathrm{QW},i} \cdot L_{\mathrm{QW}}, && i = 1, 2, 3\ldots \end{aligned} \tag{3.11}$$

For each new QW, the initial surface density of SDs will be reduced by the amount of SDs captured in the previous QWs. We can then compute for each QW the density of SDs taking into account the QW parameters from Armstrong *et al.*, i.e., $L_{\mathrm{QW}} = 2.5$ nm, $x_{\mathrm{QW}} = 0.13$ [93]. We keep the interaction efficiency, $p = 0.7$ The dots in Fig. 3.9 are the densities computed with Eq. (3.10). We used the defect density of the first QW to compute the initial defect density θ_0 and found a value equal to 4.4×10^9 cm^{-2}.

When looking at papers which are trying to optimize the InGaN QWs, often we can see that indium is added into the barriers for different reasons [94, 95]. Keller *et al.* studied the effect of a confinement layer made of several QWs with a low indium content (6 to 2 %) on an $\mathrm{In_{0.13}Ga_{0.87}N}$ SQW. The Authors found that when the number of QWs in the confinement layer is increased, the SQW is more efficient [94]. Shee *et al.* studied $\mathrm{In_{0.13}Ga_{0.87}N/In_{0.02}Ga_{0.98}N}$ MQW structures where they varied the thickness of the barriers. They observed an increase of the effective lifetime when the barrier thickness is increased [95]. In both cases, when indium is added before the active QW, the QW efficiency increases, which is in line with our findings.

Summary

In this chapter, we have shown the critical role of indium for the incorporation of SDs by studying the effect of the composition and the thickness of the UL on the QW efficiency. We proposed a set of equations to describe the capture of SDs in In-containing layers. This phenomenological model works for two different reactors and different types of substrate (FS-GaN and GaN on sapphire templates). We also discussed some papers from the literature and showed that some effects, such as the improved performance of MQWs versus SQWs and the usage of low indium content InGaN barriers, could also be due to the incorporation of SDs in the first QWs or in the InGaN barriers which would then "mimic" the InGaN UL.

4 Creation and nature of the surface defects

In the previous chapter, we discussed about the incorporation of SDs in the InGaN UL. However, our observations were not able to give us a clue about their nature, and why they are present in QWs. We will show in this chapter how those SDs are created and which kind of defects they can be related to.

4.1 Creation of surface defects

Usually, the first step in sample growth is to flatten and clean the surface by depositing a thick GaN buffer layer. Substrate are known to bring some impurities in the reactor which could eventually segregate through all the layers and reach the QWs [96]. Another possibility is that impurities are introduce during the GaN growth, either by the reactor walls or by the precursors. To check this hypothesis, we grew a GaN buffer on top of a thick InGaN UL which is supposed to bury all SDs.

For this purpose, a sample is grown in the showerhead reactor with the layer sequence shown in Fig. 4.1 (sample B) on FS-GaN substrate. The first layer is a GaN buffer layer grown using standard buffer conditions, i.e., at 1000°C with TMGa under H_2. Then, the temperature is decreased, and the carrier gas is switched to N_2 to grow a 55 nm thick $In_{0.03}Ga_{0.97}N$ UL. The InGaN UL capture most of the SDs, as shown in the previous chapter. We then grow a second GaN buffer layer of 500 nm using the exact same conditions as the first one (1000 °C, TMGa and H_2). Finally, we grow, on top of the second buffer, a GaN spacer at 770 °C with TEGa under N_2 and an InGaN QW with a GaN cap layer. The top part of the sample (spacer, barrier, QW, and cap) is grown as the samples in Series B and D presented in the last chapter.

Quasi-resonant PL at room temperature is performed with a CW 375 nm laser on the sample with the double GaN buffer and on a similar sample with a 55 nm thick InGaN UL (see Fig. 4.1). Surprisingly, when the second GaN buffer is added between the QW and the InGaN UL, the integrated PL intensity drops by a factor 50, a value which is close to the difference found in intensity between samples with and without UL (×40, see Sec. 2.2). Even if the presence of an InGaN UL should have removed all the SDs, the QW efficiency of sample B is poor. Hence, it seems that the additional GaN buffer layer present in sample B has regenerated SDs.

When comparing the structure of samples A and B, the thickness of the GaN buffer layer inserted between the InGaN UL and the SQW is the first striking difference. However, we have shown in Chap. 2 that a thick layer of GaN (100 nm) grown in the same conditions as the InGaN UL is not impacting the QW efficiency. Therefore, we can look for other differences between the two GaN buffer layers. The buffer is grown with TMGa as precursor, H_2 as carrier gas and at 1000 °C, which differ from the growth conditions usually chosen for the GaN layer grown after the InGaN UL (TEGa, N_2 and 770 °C). Several phenomena could happen due to these different growth conditions and hence could decrease the SQW efficiency: TMGa could bring some new impurities, H_2 can impact the indium sticking coefficient and the morphology, the reactor can outgas due to the high temperature and release some impurities. In the following section, we will study the effect of the different gases and that of the growth temperature.

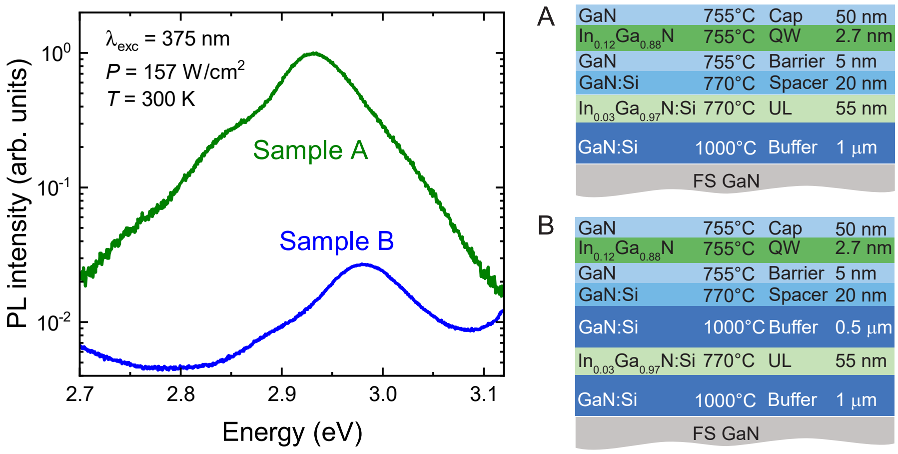

Figure 4.1 – PL spectra measured with a CW 375 nm laser at room temperature. Sample A is the reference structure with a 55 nm thick InGaN UL. Sample B has an additional GaN "buffer" layer between the 55 nm thick InGaN UL and the InGaN QW.

4.1.1 Metalorganic precursors and carrier gases

Metalorganic precursors

GaN can be grown using two types of metalorganic compounds: TMGa and TEGa. However, as TMGa is known to be a higher source of carbon and oxygen contamination [97], we only use it to grow the non active part of optoelectronic devices, i.e., the GaN buffer layer. Here, we propose to replace TEGa by TMGa during the growth of a sample in order to compare the SQW efficiency, and find a correlation with the carbon or oxygen concentration.

For this purpose, two samples with the same structure are compared (Fig. 4.2(d)). One is the reference structure grown with TEGa and N_2, which is the same as in Chap. 3, for which the

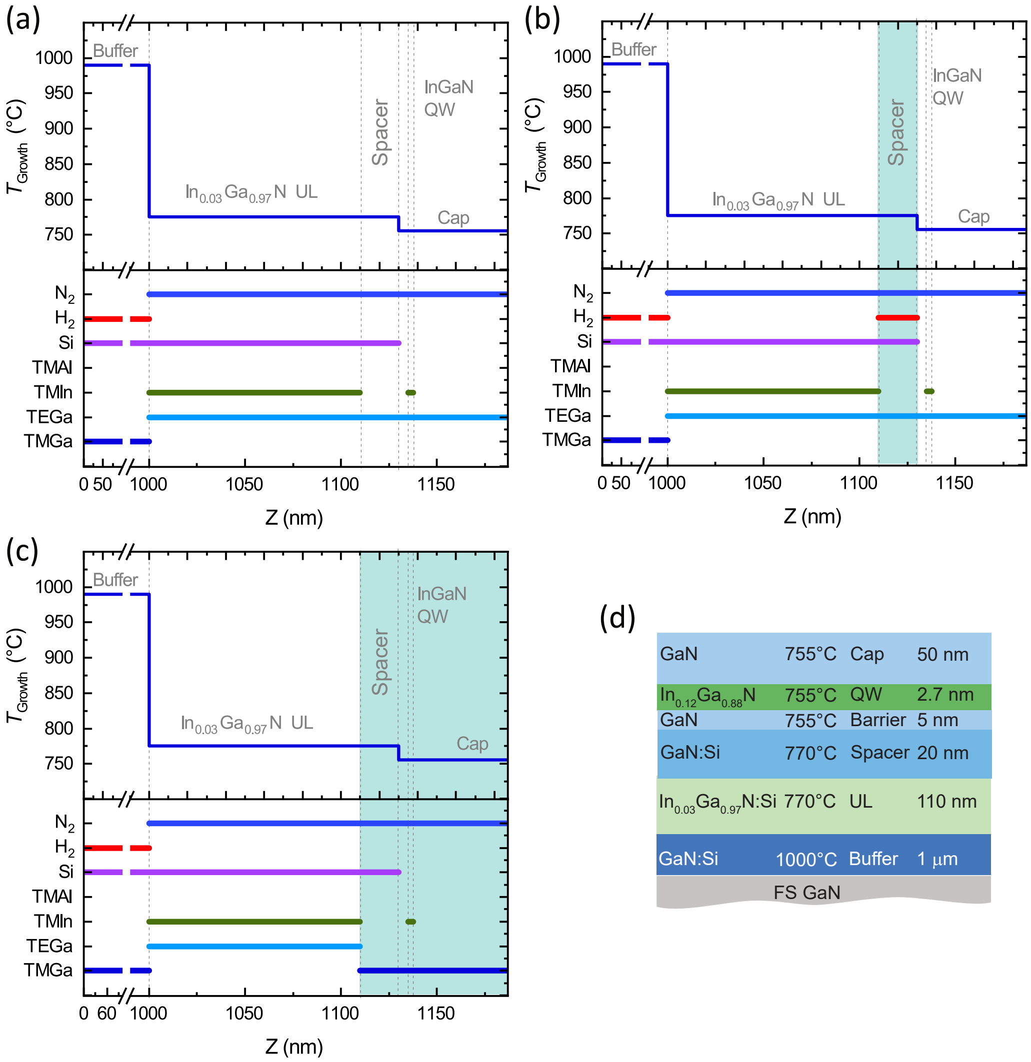

Figure 4.2 – (a) Growth conditions used for the reference sample with a GaN spacer grown with TEGa under N_2. (b) Growth conditions used for the sample with a GaN spacer grown with TEGa under H_2 and N_2. (c) Growth conditions used for the sample with the top part grown with TMGa under N_2. (d) Sample structure used in this section independently of the growth conditions. The green zone in (b) and (c) is the part of the sample where the growth conditions are changed compared to (a).

growth parameters are described in Fig. 4.2(a). The second sample is grown using conditions similar to the reference sample until the end of the InGaN UL. For the spacer, the barrier, the QW, and the cap, TEGa is replaced by TMGa under N_2 (Fig. 4.2(c)). The growth conditions are adapted to get a growth rate similar to that with TEGa. All the samples in this chapter are grown on FS-GaN with the showerhead reactor.

The SQWs are emitting around 2.65 and 2.82 eV for the samples grown with TMGa and TEGa, respectively (Fig. 4.3). The integrated PL intensity at 300 K for both samples is almost similar,

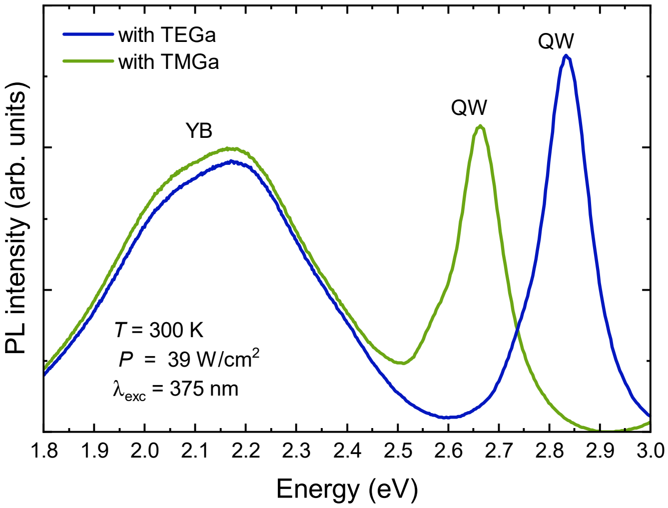

Figure 4.3 – PL spectra recorded at room temperature: the top layers (spacer, barrier, SQW, and cap) were grown with either TEGa under N_2 or TMGa under N_2.

but the SQW grown with TMGa exhibits a smaller PL intensity and a redshift. The PL ratios $Q_{\mathrm{PL},300\,\mathrm{K}/12\,\mathrm{K}}$ for an excitation power of 39 W/cm^2 are $Q_{\mathrm{PL},300\,\mathrm{K}/12\,\mathrm{K}}$= 10 % for the SQW with TMGa and $Q_{\mathrm{PL},300\,\mathrm{K}/12\,\mathrm{K}}$= 12 % for the SQW with TEGa. This slight difference could be due to the lower oscillator strength of the QW emitting at lower energy. Notice that the redshift of the SQW grown with TMGa could be the result of a larger growth rate and/or a higher In content.

Aiming to a similar SQW efficiency, we can deduce that SDs are not created via the use of TMGa. Therefore, impurities such as oxygen and carbon do not seem to contribute to the SD creation mechanism, which will be confirmed later on in this chapter by SIMS measurements. However, in the case of LEDs, impurities are more problematic as they could change the doping level and hence could impact the electrical injection, which probably explains why TEGa is always used to grow the active region of LEDs.

Carrier gases

As for metalorganic precursors, we compared two samples with the same structure but with different growth conditions (Figs. 4.2(a) and 4.2(b)). The only difference between the two samples is the nature of the carrier gas used during the spacer growth. Indeed, for the reference sample, only nitrogen is used, and in the other sample, hydrogen and nitrogen are both present. For the sample grown under H_2, the spacer is deposited with TEGa using N_2 as carrier gas, but the chamber was filled with H_2. Indeed, hydrogen is known to smooth the surface morphology at high temperature. Also, the presence of H_2 removes any residual indium atoms after the InGaN UL growth, which allows us to discard any surfactant effect.

The SQW PL intensity at 300 K is nearly identical for both samples (Fig. 4.4).The SQW emission

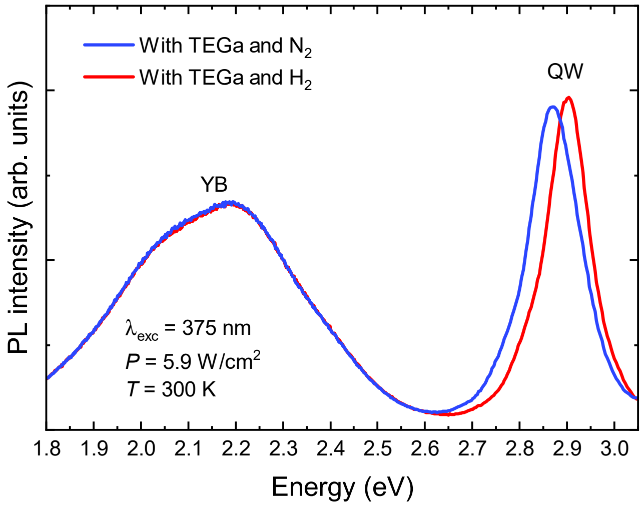

Figure 4.4 – PL spectra recorded at room temperature on a sample with a GaN spacer grown with TEGa under N_2 and a sample with a GaN spacer grown with TEGa under H_2.

for the sample grown with a spacer under H_2 (red curve) is slightly blueshifted. This could come from the presence of some residual H_2 in the chamber during the QW growth, which could have modified the indium incorporation. However, the energy difference is small (0.03 eV), which can also be due to a small variation in the reactor temperature. Additionally, the PL ratio, $Q_{\mathrm{PL,300\,K/12\,K}}$, is almost similar for both samples: $Q_{\mathrm{PL,300\,K/12\,K N_2}} = 3.5$ % and $Q_{\mathrm{PL,300\,K/12\,K H_2}} = 3.1$ % at an excitation power density of 5.9 W/cm^2 with the 375 nm laser. We can therefore conclude that hydrogen has no impact on the QW efficiency and does not play a significant role in the creation of SDs.

We have just shown that TMGa and H_2 do not markedly affect the efficiency of the InGaN QW. Therefore, we can conclude that they do not contribute to the generation of SDs, despite a higher level of impurities such as carbon and oxygen in TMGa compared to TEGa.

4.1.2 Temperature

We have seen in the introductory part of this chapter (Fig. 4.1) that while the surface is free from any SDs after an InGaN UL, the growth at HT of a GaN layer reintroduces SDs. In this section, we thus study the effect of the growth temperature. To this aim, we designed a sample series with a GaN layer inserted between the UL and the SQW grown at different temperatures (Fig. 4.5(a)).

The buffer and the 55 nm thick InGaN UL are grown with the same growth conditions than in the last section. A 20 nm thick GaN spacer is deposited on top of the InGaN UL at 770°C, followed by a 60 nm thick GaN layer at different temperatures (770, 850, 900, 935, 990, and 1020 °C). Then the temperature is set back to 770 °C and a 20 nm thick GaN spacer is grown.

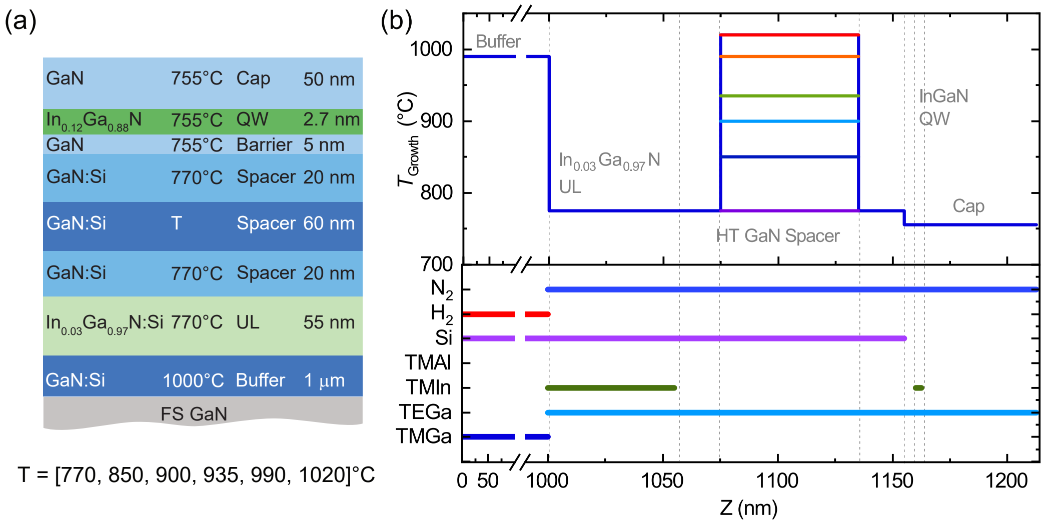

Figure 4.5 – (a) Schematic view of the sample structure where the GaN spacer temperature is varied. (b) Growth conditions used for the spacer temperature series.

As always, the top part of the sample is made of a 5 nm thick GaN barrier, a 2.7 nm thick $In_{0.12}Ga_{0.88}N$ QW and a 50 nm thick GaN cap grown at 755 °C. The sample structure and the growth conditions are displayed in Figs. 4.5(a) and 4.5(b).

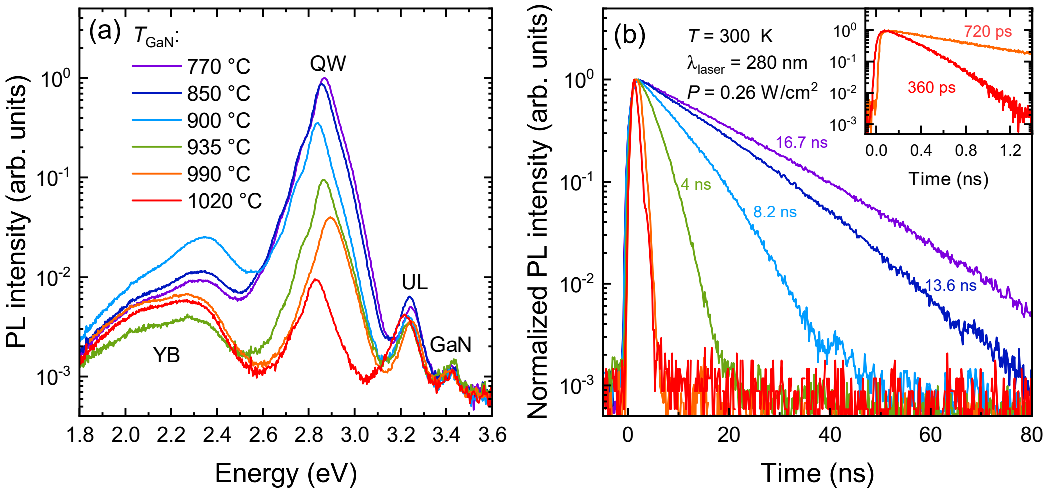

Figure 4.6 – (a) PL spectra measured at 300 K for the spacer temperature series. Each curve corresponds to a different spacer temperature, see Fig. 4.5(a). (b) Normalized QW PL decay traces at 300 K which correspond to the spectra shown in (a). The time window is 80 ns for (b) and 1.3 ns for the inset, respectively.

Non-resonant PL is performed on all the samples with a 280 nm pulsed laser. PL spectra are shown in Fig. 4.6(a). As always, four peaks can be observed on the spectra: the YB, the QW, the InGaN UL, and the GaN band-edge. Interestingly, a clear trend is observed when the spacer growth temperature, T_{GaN}, is increased: the QW peak intensity drops. The intensity is reduced by a factor of 100 when T_{GaN} is varied from 770 to 1020 °C.

The PL decay of the QW measured at room temperature is reported in Fig. 4.6(b). As for the QW intensity, when T_{GaN} is increased the effective lifetime is decreased. For a temperature close to the buffer temperature, T_{GaN} = 1020 °C, the effective lifetime (360 ps) is on the same order of magnitude than the one of a QW without any UL (170 ps, see Fig. 3.2). Clearly, the temperature of the GaN layer strongly impacts the SQW efficiency.

Double InGaN UL

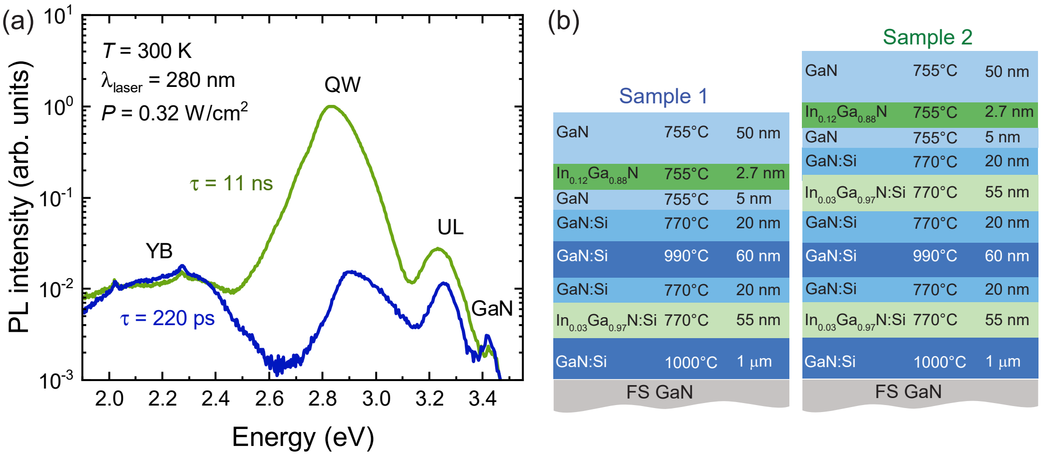

Figure 4.7 – (a) PL spectra measured at 300 K with a 280 nm laser. The blue line is for the sample with a HT spacer (sample 1) and the green line for the sample with a HT spacer and an additional InGaN UL (sample 2). (b) Structure of the two samples measured in (a).

At this stage, one may wonder if the defects created during the HT growth can also be trapped in the InGaN UL. Thus, a sample was prepared with a HT layer (990 °C) but in between the HT layer and the QW, a 55 nm thick $In_{0.03}Ga_{0.97}N$ UL was added, see Fig. 4.7(b), sample 2. Non-resonant PL and TRPL experiments are performed at 300 K on the two samples. As expected, the sample with the HT spacer (sample 1) has a low PL intensity and a short effective lifetime of 220 ps for an excitation power density of 0.32 W/cm^2. When an InGaN UL is added after the HT spacer, the effective lifetime and the intensity increases. An effective lifetime of 11 ns is measured for sample 2, which is on the same order of magnitude than for a reference sample with a single 55 nm thick $In_{0.03}Ga_{0.97}N$ UL (16 ns at 300 K for an excitation power density of 0.26 W/cm^2). Therefore, the SD creation really depends on the temperature.

Buffer temperature

In all samples, there is usually a GaN buffer layer grown at HT to refresh the substrate surface and bury impurities, which may otherwise be incorporated into the QW. On the other hand, the HT growth seems to be responsible for the creation of SDs. We thus wondered whether the

GaN buffer temperature may change the QW efficiency.

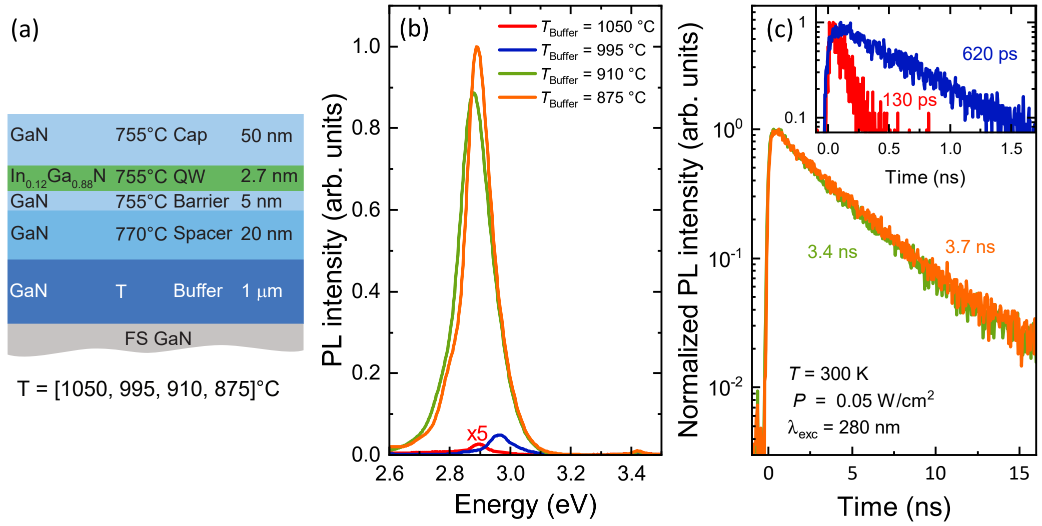

Figure 4.8 – (a) Sample structure used for the series with a variation of the GaN buffer temperature. (b) PL spectra measured at 300 K with a 280 nm laser for samples with different buffer growth temperatures. (c) Normalized QW PL decay traces for samples with a buffer temperature T_{Buffer} = 875 and 910 °C with a time window of 12 ns and for samples with T_{Buffer} = 995, and 1050 °C with a time window of 1.7 ns (inset), respectively. Courtesy of Yao Chen.

A sample series with different buffer temperatures is grown (875 to 1050 °C). The sample is grown with conditions similar to those of the SQW sample without UL presented in Chap. 2 (Fig. 4.8(a)).

The SQW integrated PL intensity dramatically increases when the buffer temperature is reduced from 1050 to 875 °C, see Fig. 4.8(b). Furthermore, the SQW effective lifetime is also increased when the buffer temperature is reduced from 130 ps to 3.7 ns (Fig. 4.8(c)). This is in line with our previous observations on the impact of the spacer growth temperature on the SQW efficiency. The effective lifetimes as a function of buffer growth temperature are reported in Fig. 4.9.

The effect of the buffer temperature is striking. There is a clear link between the GaN growth temperature and the SD density.[1]

Activation energy

The effective lifetime as a function of GaN spacer growth temperature and as a function of buffer temperature is reported in Fig. 4.9. The effective lifetime dramatically drops, i.e., the

---

[1] Note that a low growth temperature for thick layers will promote meandering features due to the lower atom mobility [90]. Furthermore, in the case of GaN on sapphire templates, a reduction of the buffer temperature might cause some additional problems as thick GaN buffer layers grown at high temperature are used to reduce the threading dislocation density.

NR lifetime decreases when the temperature increases. The SD density thus depends on the temperature and could be generated by a mass action law, with an activation energy E_a. To extract an activation energy from these measurements, we used Eq. (3.5) and made the hypothesis that $\tau_{\mathrm{NR,SD}}$ is inversely proportional to the SD density in the QW. In such a case, we can write:

$$\tau_{\mathrm{eff}} = \tau_0 \frac{1}{1 + \tau_0 \beta \exp\left(\frac{-E_a}{k_b T_{\mathrm{GaN}}}\right)}, \tag{4.1}$$

with τ_0 the effective lifetime in absence of SDs in the QW, E_a the related activation energy, β a proportionality factor, T_{GaN} the GaN growth temperature.

We fitted Eq. (4.1) to the data corresponding to the variation of the spacer growth temperature (blue dots) with a fixed value of τ_0 = 20 ns and found an activation energy of 3.6 eV. Interestingly, the activation energy is close to that of GaN evaporation which is reported between 3.4 and 3.6 eV [98, 99].

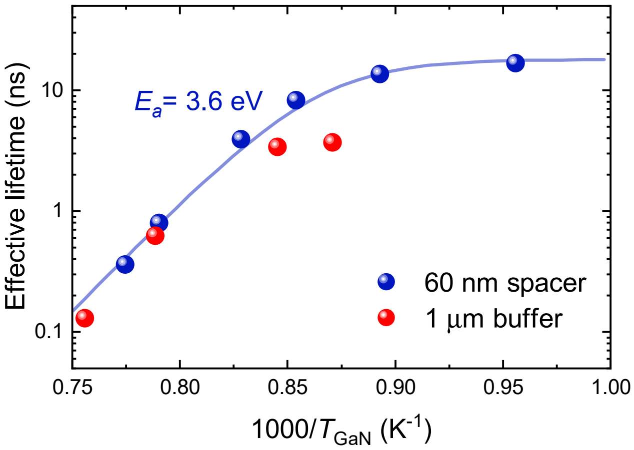

Figure 4.9 – Effective lifetime reported as a function of growth temperature of the spacer (blue dots, Fig. 4.6(b)) and the buffer (red dots, Fig. 4.8(b)). The blue line is a fit obtained from Eq. (4.1) with a fixed τ_0 value of 20 ns.

For the sample series where the buffer temperature was varied (red dots, shown in Fig. 4.9), at high temperature (> 950 °C), the SQW effective lifetime has a value similar to that of a spacer of 60 nm. However, for lower temperatures, the SQW effective lifetime in this buffer temperature series is shorter, than for the 60 nm spacer case, which indicates a higher SD density. Probably, the thickness and the growth rate difference between the two GaN layers which are generating the defects play a role.

In this section, we demonstrated that the growth temperature is the main mechanism behind SD creation. The density of SDs can be controlled as they form at temperatures higher than 850 °C and they can be buried in an indium-containing layer. This can be an advantage as we can introduce SDs in an InGaN layer without changing the whole structure of a sample, which could allow studying the InGaN layer properties, such as disorder, indium incorporation, etc.

4.2 Nature of the surface defects

In the last section, we showed that the growth temperature is responsible for the creation of SDs. However, the nature of SDs is still unknown. Two main families of point defects could be invoked. The first one deals with all kinds of impurities as they can create traps in the bandgap that could be activated by the temperature. The second one corresponds to intrinsic point defects such as vacancies, which are also known to be thermally activated [100].

4.2.1 Impurities

Unwanted impurities are always present in small amount in semiconductor samples. They can come from different sources such as the gases (carrier gases and metalorganic gases), the reactor or the substrate. One way to evaluate the concentration of impurities in the material consists in performing secondary ion mass spectrometry (SIMS). The latter is a technique where the sample surface is sputtered by means of a primary ion beam, and the ejected secondary ions are collected and analyzed by ion mass spectrometry. It will give us the concentration for a given atomic species. All the SIMS analyses shown in this work were done by EAG Laboratories, and the reported concentrations are absolute values.

During their decomposition, metalorganic precursors can introduce carbon, oxygen, and hydrogen in the layers. These impurities could have an impact on the number of NRCs present in the QW. We chose two samples from the temperature series, one with a spacer temperature of 770 °C and the other one with a spacer temperature of 990 °C (Fig. 4.5). From our previous experiments, we know that the sample with a LT spacer (770 °C) has less NRCs in the SQW. In Fig. 4.10, concentrations of different impurities are displayed for these two samples. The carbon, oxygen and hydrogen concentrations are shown in Figs. 4.10(a), 4.10(b), and 4.10(c), respectively.

In the case of carbon, the detection limit of SIMS is $\sim 3 \times 10^{15}$ cm^{-3}. The level of carbon in the SQW is close to the detection limit for both samples, and the carbon concentration did not rise with the increase in the spacer temperature. Furthermore, carbon starts to impact the QW efficiency for a level higher than 1×10^{17} cm^{-3}, as demonstrated in Ref. [101]. As expected, the only part of the sample with a higher carbon concentration level is the buffer. Indeed, TMGa is known to introduce a higher amount of carbon in the layer than TEGa [97]. We can thus safely conclude that carbon impurities are not governing the SQW efficiency.

Oxygen impurities impact the QW efficiency at a level higher than 2×10^{17} cm^{-3} according to Ref. [102]. However, the concentration of oxygen in the SQW and the InGaN UL is smaller than this critical value, as shown in Fig. 4.10(b). Also, the O concentration is similar for both samples. For hydrogen, the concentration in both samples is around 6×10^{17} cm^{-3}, and no

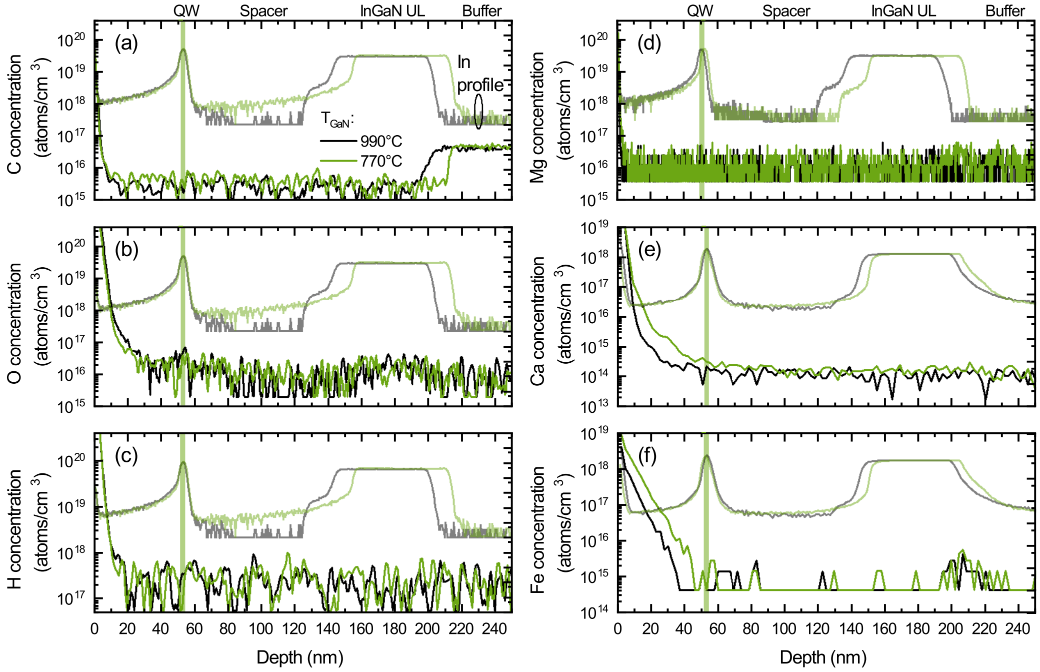

Figure 4.10 – SIMS measurements for different atomic species performed on two different samples: one with a HT spacer (990°C), in black, and one with a LT spacer (770 °C) in green. The sample structures are displayed in Fig. 4.5. The concentration in carbon, oxygen, hydrogen, magnesium, calcium, and iron is displayed in (a), (b), (c), (d), (e), and (f), respectively.

correlation is observed between the H concentration and the SQW efficiency. In the last section, we have shown that the metalorganic precursor (TMGa or TEGa) or the carrier gas (H_2 and N_2) used to grow InGaN and GaN were not playing a role on the SQW efficiency. This is in line with the fact that SDs are not linked to C, O or H, as confirmed by the present SIMS measurements.

For these two samples, three other impurities were monitored by SIMS, namely: Mg, Ca, and Fe. Magnesium is used to obtain p-type layers. However, as the samples are grown with a showerhead reactor with potential memory effects, some residual Mg could be present during the growth of the SQW and could impact the efficiency for a level higher than 5×10^{17} cm^{-3} [103]. In our samples, the Mg concentration was under the detection limit ($< 2 \times 10^{16}$ cm^{-3}) for both samples, as shown in Fig. 4.10(d). Calcium was reported to be present at the substrate surface and was shown to incorporate at low growth temperature in the case of MBE growth [96]. A theoretical study shows that the InGaN QW efficiency is impacted for a level higher than 1×10^{17} cm^{-3} [104]. As for magnesium, the Ca level in both samples is under the SIMS detection limit ($< 3 \times 10^{15}$ cm^{-3}), as shown in Fig. 4.10(e). This is below the critical level proposed by Shen *et al.* [104]. We also looked at the iron concentration in our layer as iron could come from the stainless steel showerhead and is known to segregate [107]. Furthermore, Fe could be an efficient NRC in InGaN [105]. We found an Fe concentration of 2.5×10^{15} cm^{-3}, which

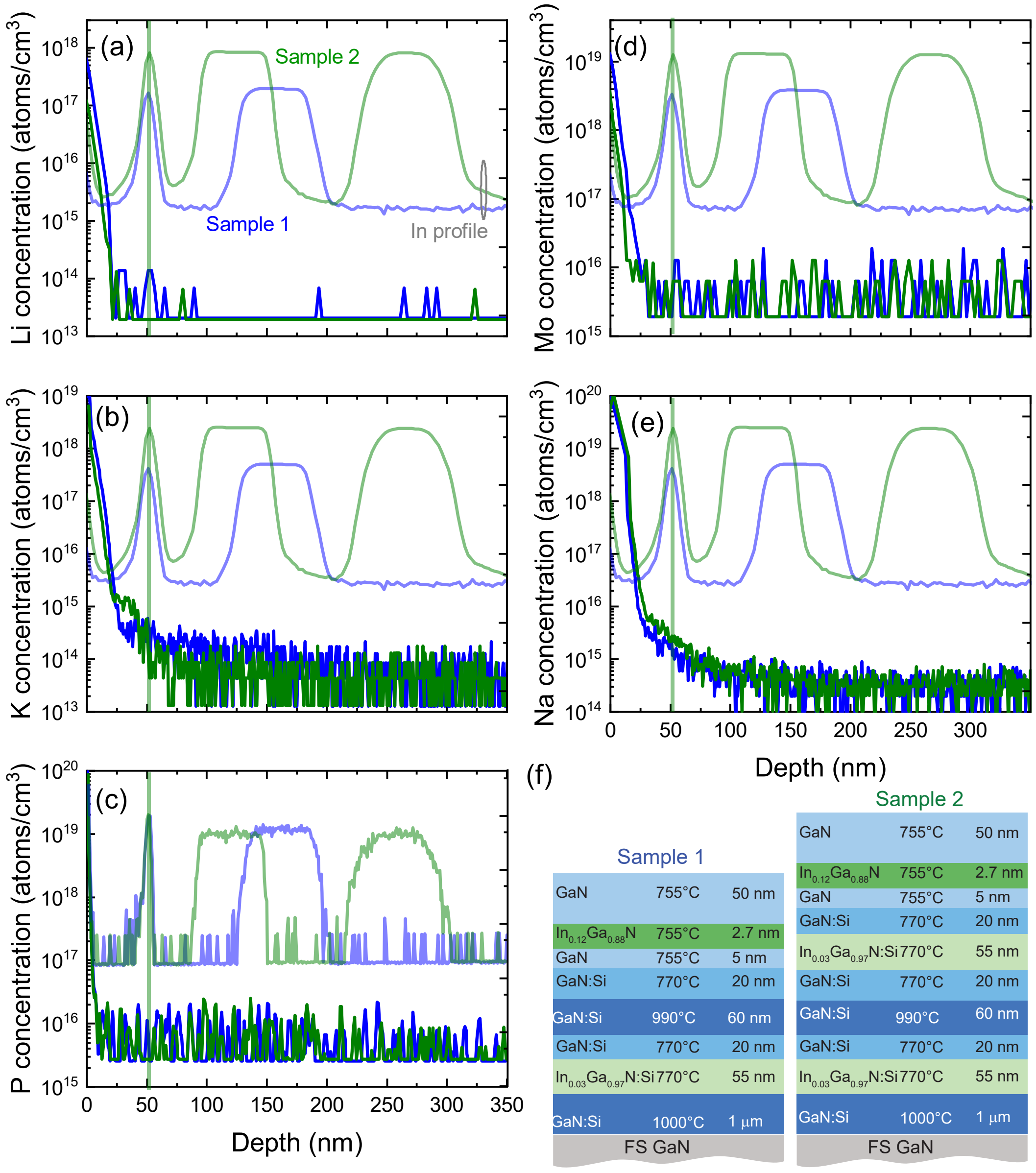

Figure 4.11 – SIMS measurements for different atoms performed on two different samples: one with a HT spacer (990°C), in blue, and one with a double UL in green. The sample structures are displayed in (f). The concentration of lithium, potassium, phosphorus, molybdenum and sodium atoms are displayed in (a), (b), (c), (d), and (e), respectively.

is slightly higher than the critical level proposed by Wickramaratne *et al.* [105]. However, the sample with the LT spacer (770 °C), in green in Fig. 4.10(f), shows the highest concentration level. Therefore, no obvious correlation could be found between iron concentration and SQW efficiency.

Additional impurities were investigated in two other samples. The sample structures, which

Z	Impurity	Level detected in the present samples [cm^{-3}]	Detection limit [cm^{-3}]	Level detected in commercial LEDs [cm^{-3}]	Critical level [cm^{-3}]
3	Li	2×10^{13}	$\leq 3 \times 10^{13}$		
6	C	3×10^{15}	$\leq 3 \times 10^{15}$		1×10^{17} [101]
8	O	2×10^{16}	$\leq 1 \times 10^{16}$		2×10^{17} [102]
11	Na	5×10^{14}	$\leq 3 \times 10^{14}$		
12	Mg	1.5×10^{16}	$\leq 2 \times 10^{16}$		5×10^{17} [103]
14	Si	2×10^{16}	$\leq 1 \times 10^{16}$		
15	P	7×10^{15}	$\leq 6 \times 10^{15}$		
19	K	7×10^{13}	$\leq 4 \times 10^{14}$		
20	Ca	1.6×10^{14}	$\leq 3 \times 10^{15}$	$\leq 1 \times 10^{13}$ [96]	1×10^{17} [104]*
22	Ti			$\leq 1 \times 10^{13}$ [96]	
24	Cr			$\leq 1 \times 10^{13}$ [96]	
26	Fe	2.5×10^{15}	$\leq 1 \times 10^{15}$	$\leq 1 \times 10^{13}$ [96]	1×10^{15} [105]*
28	Ni			$\leq 1 \times 10^{13}$ [96]	
29	Cu			$\leq 1 \times 10^{13}$ [96]	
30	Zn			$\leq 1 \times 10^{13}$ [96]	[106]**
42	Mo	5×10^{15}	$\leq 4 \times 10^{15}$		

Table 4.1 – Impurity concentrations measured in the present samples and in commercial LEDs. We also indicate, whenever possible, the critical level which may affect the LED efficiency.
*Papers based on simulations.
**Zinc was found to improve the radiative efficiency of InGaN QWs.

are analyzed, are displayed in Fig. 4.11(f). Sample 2 (green) has a better QW efficiency than Sample 1 (blue). Li, K, P, Mo, and Na concentrations were measured, see Figs. 4.11(a-e). As for the previous SIMS measurements, no correlation could be found between the SQW efficiency and the impurity concentration. Furthermore, most of the impurity concentrations are below the SIMS detection limit. From literature, we can also discard some additional impurities, such as Ti, Cr, Ni, Cu, and Zn [96]. All the impurities measured and studied are summarized in Tab. 4.1. As none of the present common impurities are playing a role on the SQW efficiency, it might not be impurities which are at play. Furthermore, the fact that the InGaN UL is used in all commercial devices where the gas purity is likely very high, and in various MOVPE reactors, tends to discard impurities as being the source of SDs.

4.2.2 Intrinsic defects

In the last sections, we found that the growth temperature controls the SD density and we excluded most of the common impurities as being at their origin. Intrinsic defects such as vacancies can be a possibility for different reasons. First, the growth temperature is known to create some vacancies in semiconductors [100], and the activation energy is close to that of GaN evaporation (3.6 eV) [98, 99], which indicates issues with the surface stability of GaN. Additionally, in other materials, vacancies are diffusing toward the surface [108], which could also be the case here as the vacancy formation energy is higher in bulk GaN than at the surface [109, 110]. This could match with our observations, as SDs are created during the HT GaN growth and stay at the surface in the LT GaN until they encounter some indium-containing layers. Two types of vacancies are possible in GaN: gallium vacancies, V_{Ga}, and nitrogen vacancies, V_N. We will study the possibilities that SDs are one of these two kinds of vacancies type.

Gallium vacancy

The gallium vacancy was proposed as an explanation for the YB luminescence in GaN in 1996 [111]. Its formation energy was theoretically computed to be rather low (1.6 eV) when the Fermi level is close to the conduction band maximum [111]. If the formation energy of V_{Ga} is small, these vacancies should not segregate as they should be incorporated into GaN. Experimentally, we observed the segregation of SDs in 200 nm thick GaN layers grown at LT, see Fig. 3.5.

We also know that SDs should create a deep level with an energy at $E_c - 1.62$ eV based on the study by Armstrong *et al.* [64]. They found that the impact of these deep levels is reduced when an InGaN UL is added. However, the deep levels associated with gallium vacancies are located at $E_c - 0.56$ eV and $E_c - 0.23$ eV according to Ref. [108]. As the energy difference between V_{Ga} deep levels and $E_c - 1.62$ eV is important, we could discard the gallium vacancies as being at the origin of SDs. Furthermore, if gallium vacancies were acting as NRCs, they could also impact GaN/AlGaN QWs. We carried out a study on the effect of the InGaN UL on GaN/AlGaN QWs and did not find any effect of the InGaN UL, as shown in App. A.2.

A recent study showed that the formation energy for V_{Ga} is higher than expected, namely, around 4.5 eV [112], which makes the presence of Ga vacancies alone less probable in as-grown GaN layers, but complexes with hydrogen or oxygen are more likely as their formation energy is lower (around 0.5-1 eV for V_{Ga}-O_N-2H [47]). Dreyer *et al.* proposed that V_{Ga} with oxygen or/and hydrogen, can act as be NRCs in InGaN layers [47]. However, their computation showed a strong dependence of the A coefficient on indium concentration. They computed the A coefficient for a defect density of 10^{16} cm^{-3} as a function of indium content and found that for indium contents lower than 15 %, the A coefficient drops quickly below 10^4 s^{-1} , i.e., those complexes should have a marginal role. Furthermore, if those complexes are related to SDs, an increase in the oxygen or/and the hydrogen content should have been observed by SIMS in the InGaN SQW and in the InGaN UL, which is not the case. We can thus safely conclude that V_{Ga} is not the source of SDs.

Nitrogen vacancy

GaN is known to be unintentionally *n*-type doped [110]. Nitrogen vacancies, which act as a shallow donor, were proposed to be the reason for this doping in the early years of GaN films [49, 113]. However, the V_N formation energy is supposed to be rather high in *n*-type material according to theoretical computations [110]. Therefore, the concentration of V_N in bulk GaN should be low. Some other theoretical papers proposed that the concentration of V_N is not negligible in bulk GaN and could be higher than $[V_{Ga}]$ [114]. Additionally, near the semiconductor surface, the formation energy of any vacancies should be smaller [109].

As SDs are generated by the temperature, one could imagine that the main phenomena occur at the surface (or subsurface). The GaN surface was found to create N_2 during its decomposition [99, 115, 116], which could lead to a nitrogen-poor growth front. This could imply a GaN growth front with a high concentration of nitrogen vacancies. The fact that nitrogen could be missing at the growth surface could be the reason why Nakamura *et al.* invented the "two-flow" MOVPE reactor [117] and got better crystal quality. Indeed, this reactor has an additional N_2 flux, which increases the NH_3 pressure close to the surface.

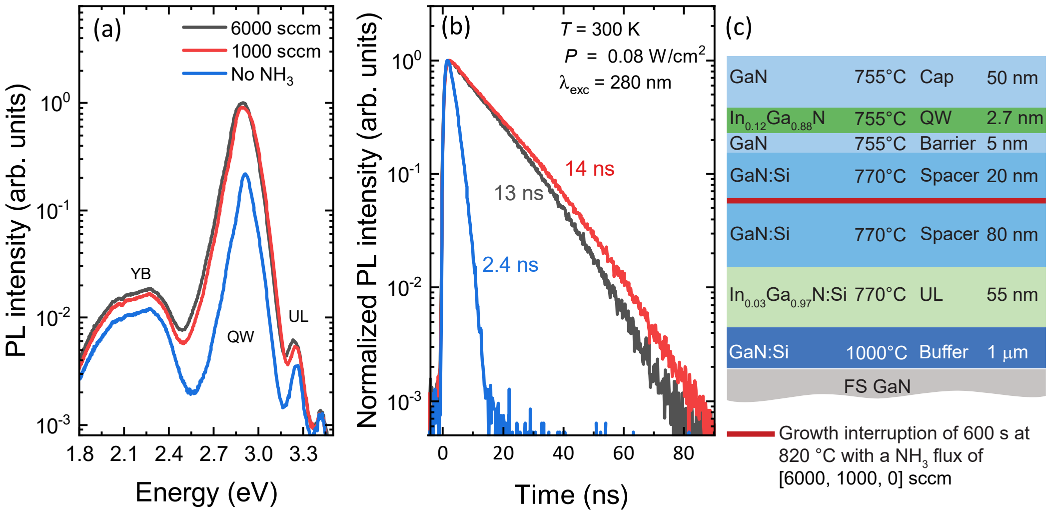

Figure 4.12 – (a) PL spectra measured at 300 K with a 280 nm pulsed laser for samples with a different NH_3 flux during growth interruption. (b) Normalized QW PL decay traces corresponding to the spectra displayed in (a). (c) Sample structure used for the NH_3 interruption series. The interruption was 600 s long under constant pressure, but the NH_3 flux was changed from 6000 sccm to no NH_3.

As NH_3 could play a role, we performed an experiment on the surface stability under different ammonia flows. For that purpose, three samples were grown on FS-GaN substrate with the showerhead reactor. The structure is shown in Fig. 4.12(c). The buffer is grown at 1000 °C with TMGa under H_2. Then the temperature is decreased, and the carrier gas is switched to N_2 for the growth of a 55 nm thick InGaN UL and of an 80 nm thick GaN spacer. After the 80 nm thick spacer, the temperature is raised to 820 °C and a growth interruption is done during 600 s. During this interruption, the pressure in the reactor chamber is kept unchanged, but the NH_3 flux is varied between 6000 sccm and 0 sccm. The GaN spacer, the GaN barrier, the QW, and the cap are similar for all the samples.

Non-resonant PL and TRPL measurements were performed at 300 K with a 280 nm pulsed laser (Fig. 4.12). Four peaks can be observed in the PL spectra (Fig. 4.12(a)): the YB (~ 1.8 eV), the InGaN SQW (~ 2.9 eV), the InGaN UL (~ 3.24 eV) and the GaN band-edge (~ 3.42 eV). The QW peak intensity decreases together with the NH_3 flux. The effect is rather small between 6000 sccm and 1000 sccm. For the sample with the NH_3 flux set to 0, the SQW intensity is diminished by a factor of 5 compared to the SQW with an NH_3 flux of 6000 sccm. From the QW PL decay, we extracted the effective lifetime for each sample. As for the QW intensity, the effective lifetime of the sample with an NH_3 flux of 6000 and 1000 sccm is almost similar (13 ns and 14 ns, respectively) as shown in Fig. 4.12(b). The shortest effective lifetime corresponds to the sample without NH_3 flux, 2.4 ns. The effect of ammonia on surface evaporation was studied in MBE [98]. It was shown that for low ammonia flows the evaporation is rather high, but it stabilized quickly for higher ammonia flows, which could explain why we observe almost no difference between the samples grown with fluxes of 1000 sccm and 6000 sccm, respectively. Therefore, in the case of low NH_3 flux, the surface is less stable, and nitrogen vacancies could be created.

Finally, we know that SDs should have a strong affinity with indium atoms as demonstrated in Chap. 3. The process could be the following one: V_N are created at the surface during the growth at high temperature but stay at the surface as they cannot be incorporated in the bulk material because of their large formation energy [118]. The segregation of the V_N is stopped when indium is present as the V_N formation energy is reduced in InGaN [119, 120], and the V_N is incorporated, creating a NRC. Indeed, Obata *et al.* performed theoretical computations on the InGaN alloy and found that the presence of indium is decreasing up to 1 eV the formation of V_N if indium atoms are the nearest neighbors. From an experimental point of view, Uedono *et al.* used positron annihilation spectroscopy to probe vacancies in InGaN layers [121]. They found that the main defect in their $In_{0.13}Ga_{0.87}N$ layers is a complex between V_N and cation vacancies V_{III}. Furthermore, they found these complexes to be also present in an $In_{0.06}Ga_{0.94}N$ layer but with a smaller density [121]. These kinds of complexes (V_{III}-V_N) were also recently found in GaN and AlGaN [122]. All these different results are in agreement with our observations. Therefore, the NRCs incorporated in the InGaN QW could be complexes involving V_N.

4.3 Surface defect density

As for the nature of these SDs, the density of SDs present at the surface remains unknown. We will try in this section to estimate their density in the SQW.

One of the first results we showed in this work is that the InGaN UL reduces the A coefficient of LEDs, as shown in Fig. 2.1. Indeed, A is equal to 1.5×10^9 s^{-1} for an LED without InGaN UL vs 5.2×10^7 s^{-1} for a sample with an InGaN UL. Depending on the capture efficiency of electrons and holes by the trap, $C_{n,p}$, the NRC density can vary over several orders of magnitude, as the density of NRCs in the QW is proportional to the A coefficient according to Eq. (1.21). Indeed, in the literature, some values for the capture efficiency of holes and electrons can be found for different kinds of defects. Thus, Ca present in $\mathrm{In_{0.15}Ga_{0.85}N}$ has a $C_{n,p}$ lower than 10^{-14} s^{-1}cm^3 according to Ref. [104]. In the case of iron in GaN, $C_{n,p}$ is close to 10^{-8} s^{-1}cm^3 [105]. Armstrong *et al.* measured a capture cross section σ of 5×10^{-16} cm^2 for the $E_c - 1.62$ eV level with a thermal velocity of 3×10^7 cm s^{-1} [64]. We can estimate $C_{n,p}$ to 1.5×10^{-8} s^{-1}cm^3. This coefficient is interesting as the deep level $E_c - 1.62$ eV is probably the deep level related to SDs. Therefore, based on Eq. (1.21), we known that:

$$N = \frac{A}{C_{n,p}}, \tag{4.2}$$

with N the density of defects in the QW. We can thus compute the defect density in our SQW without InGaN UL, 1×10^{17} cm^{-3}, and with a 55 nm thick InGaN UL, 3×10^{15} cm^{-3}. The defect density found in QW without InGaN UL was reported to be $\sim 1 \times 10^{16}$ cm^{-3} [93], which is lower than our results. Growth conditions or an overestimation of the A coefficient, due to carrier injection issue, could explain the difference.

The initial surface density of SDs, θ_0, can be estimated as we know the density of SDs captured by the SQW, C_{QW}, see Eq. (3.10). For a density of 1×10^{17} cm^{-3} and a 2.7 nm thick $\mathrm{In_{0.12}Ga_{0.88}N}$ SQW, we find 4.6×10^{10} cm^{-2}. The growth temperature creates a surface instability leading to the creation of SDs. We obtained in the last section an activation energy of 3.6 eV. At thermodynamic equilibrium, the initial surface density should be equal to:

$$\theta_0 = N_{\mathrm{site}} \exp\left(\frac{-E_a}{k_B T}\right), \tag{4.3}$$

with N_{site}, the density of sites available to create a vacancy at the surface, 1.1×10^{15} cm^{-2}. For a buffer growth temperature of 1000 °C, the initial surface density we obtain with this equation is only 6 cm^{-2} for an activation energy of 3.6 eV, which is unrealistic. To get reasonable values (between 10^9 and 10^{10} cm^{-2}), the activation energy should range between 1.2 and 1.5 eV. One possible explanation is that the GaN surface is not at thermal equilibrium and therefore we cannot apply Boltzmann law. This hypothesis is in line with the fact that in the buffer growth condition more SDs are generated for the same temperature. Probably, some surface kinetics is at play, and we cannot directly link the estimated activation energy to the density of defects. The temperature is known to impact the growth mode in MOVPE [123]. Koleske *et al.* showed that depending on the growth temperature, GaN will be grown by evaporation and recondensation (> 900 °C) or by surface diffusion (< 800 °C) [123]. Therefore, several phenomena could change the surface kinetics depending on the temperature and the growth rate.

Summary

In this chapter, experiments have been performed to find the mechanism behind the creation of SDs. We showed that the growth temperature of GaN impacts the SQW efficiency. Moreover, we showed that we can play with the SD density by increasing the growth temperature or by burying them with indium-containing layers. All the experiments that were performed lead to the conclusion that the temperature is the main factor, as summarized in Tab. 4.2.

Two open questions remain, the first one is about the nature of the SDs. We performed SIMS analyses of the main impurities known to be detrimental in InGaN QWs, without any conclusive results. Therefore, we proposed that SDs could be an intrinsic defect such as vacancies. Based on a literature review, the nitrogen vacancies or a complex between nitrogen vacancies and another group III vacancy were identified as possible candidates. However, we do not have a definitive experimental proof yet. The second question is about the density of SDs present at the surface prior to the QW growth and their creation. We estimated their density to range between 10^9 and 10^{10} cm^{-2} after the HT buffer. However, we cannot explain this high density with the activation energy we found (3.6 eV). Additional experiments should therefore be conducted in order to determine how the temperature and the growth rate are impacting the SD creation.

Experiments:	Results:	Conclusion:
Additional GaN buffer layer after the InGaN UL	The SQW intensity is decreased, see Fig. 4.1	TMGa, H_2 or T_{GaN} should create SDs
LT GaN spacer grown under H_2 or N_2 after the InGaN UL	The SQW intensity is similar, see Fig. 4.4	H_2 is not responsible for the SD creation
Top part of the sample grown with TMGa instead of TEGa	The SQW intensity is almost similar, see Fig. 4.3	TMGa is not responsible for the SD creation
GaN spacer grown at different growth temperatures	The SQW intensity and its effective lifetime are decreased when T_{GaN} is increased, see Fig. 4.6	T_{GaN} creates SDs
GaN buffer grown at different growth temperatures	The SQW intensity and its effective lifetime are decreased when T_{GaN} is increased, see Fig. 4.8	T_{GaN} creates SDs
Growth interruption with different NH_3 flows	The SQW intensity and its effective lifetime are decreased when the NH_3 flow is decreased, see Fig. 4.8	The surface stability plays a role in the SD creation
Growth interruption at LT and HT	The SQW intensity decreases when the interruption is done at HT, see Fig. A.3	The surface stability plays a role in the SD creation
Role of InGaN UL on GaN/AlGaN QWs	No variation is observed, see Fig. A.2	GaN is not affected by SD as a NRC

Table 4.2 – Experiments realized to understand the creation of SDs and main conclusions.

5 Devices: InAlN underlayer for near ultraviolet light-emitting diodes

In this work, we have shown that InGaN UL traps SDs before they reach the active region of LEDs, i.e., the InGaN QWs. It justifies the presence of InGaN UL in every commercial high efficiency blue LEDs. For blue LEDs emitting around 450 nm, the InGaN UL can have a rather high indium concentration (5 %) without absorbing the light emitted by the InGaN QW, as the InGaN QW itself has an indium content around 15 %. In Chap. 3, we demonstrated that the capture efficiency of SDs depends on the thickness and the indium content. To capture all the SDs, in the case of a high indium content UL, a thin UL is sufficient. In contrary for a low indium content UL, a larger thickness is needed to reach the same capture efficiency. Typically, for an InGaN UL with an indium content of 3%, the thickness required to removed most of the SDs is around 100 nm. However, in the case of near UV LEDs, the indium content in the QW is around 6 % or less. In this case, to avoid any absorption, the InGaN UL needs to have even less indium. As an illustration, an InGaN UL with a 0.5 % indium content should be as thick as 450 nm to capture the same amount of SDs as the 100 nm thick $In_{0.03}Ga_{0.97}N$ UL. This will have two main issues: the surface morphology impacted by the growth of a thick LT layer (due to meandering) [90], and parasitic absorption for short emission wavelength.

In Chap. 3, we have shown that any indium-containing layer could work as an UL. Therefore, we proposed to use InAlN alloy as an UL for near UV LEDs. The main benefit of InAlN is that when LM to GaN, its indium content is high (~17%) [76], but its bandgap is close to 4.5 eV [84]. In this chapter, we will discuss the InAlN properties. Then, LEDs with an InAlN bulk UL are presented. Finally, we will demonstrate a further LED improvement by introducing InAlN/GaN SL UL.

5.1 InAlN material

InAlN alloy is challenging to grow. Indeed, the growth conditions of the two binary compounds (InN and AlN) are rather opposite. In the case of InN, a low growth temperature, around 600 °C should be used, and for AlN, a high growth temperature over 1000 °C is required in MOVPE. Furthermore, InAlN is predicted to be sensitive to phase separation [124]. However, InAlN has

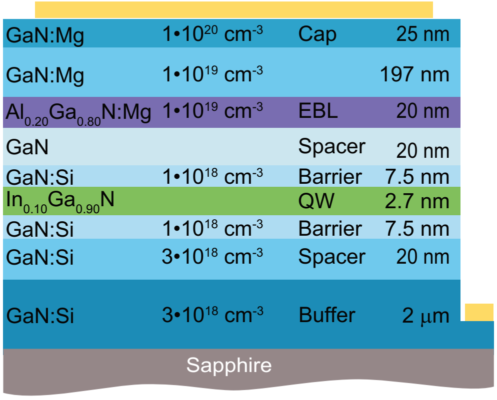

Figure 5.1 – Schematic view of an LED structure without UL used as reference sample in this chapter.

some interesting properties.

As shown, in Fig. 1.2, InAlN is LM to GaN for a composition around 17 % [76, 125]. Therefore, thick LM InAlN layers can be grown on GaN without any relaxation issues contrary to InGaN. In LM condition, InAlN exhibits a wide bandgap, ~4.5 eV at 300 K [84]. This property is particularly interesting for InAlN UL as it will not absorb the light emitted by the active region of near UV LEDs. Also, its wide bandgap is associated to a small refractive index, which is why InAlN/GaN quarter wave layer stacks are used in distributed Bragg reflectors [125].

LM InAlN has some interesting qualities, but several challenges need to be overcome. The first one is the important polarization mismatch between LM InAlN and GaN, which will create some unwanted built-in field in the samples [87]. The second problem is the morphology of thick InAlN layers. For thick LM InAlN layers, kinetic roughening occurs which induces hillocks, and after a given thickness depending on the growth condition, V-pits are formed [88]. We will address this aspect in Sec. 5.3.

5.2 InAlN bulk underlayer

5.2.1 LED structures and properties

To compare the effect of an InAlN bulk UL on a LED, we grew two LED structures on GaN on sapphire template. The first one is a reference structure without any UL (Fig. 5.1) and the second one is the same structure with a LM InAlN UL (Fig. 5.2(a)). The growth is performed in the horizontal reactor to avoid any unwanted gallium incorporation during the InAlN layer growth. For both samples, a GaN:Si buffer of 2 μm is grown with TMGa under H_2. Then the temperature is decreased to 770 °C, and the carrier gas is switched to N_2. For the sample with the InAlN bulk UL, a 50 nm thick $In_{0.17}Al_{0.83}N$:Si layer is grown with TMAl and TMIn. For both samples a GaN:Si spacer of 20 nm is grown with TEGa. The buffer, the UL and the spacer are n-doped with a level around 3×10^{18} cm^{-3}. A 7.5 nm thick GaN:Si barrier is then grown with a

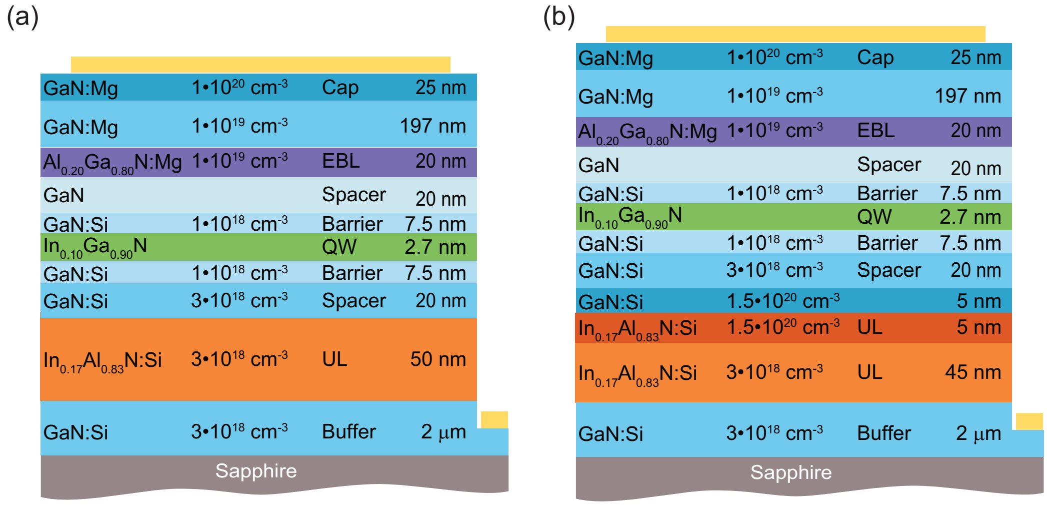

Figure 5.2 – (a) Schematic view of an LED structure with an InAlN bulk UL. (b) Schematic view of an LED structure with an InAlN bulk UL where the last 10 nm of the InAlN bulk UL and the GaN spacer are highly *n*-doped (1×10^{20} cm^{-3}).

doping level of 1×10^{18} cm^{-3} followed by a 2.7 nm thick $In_{0.1}Ga_{0.9}N$ QW and a 7.5 nm thick GaN:Si barrier and capped by a 20 nm thick undoped GaN spacer. The temperature is raised to 1000 °C, and the carrier gas is switched to H_2. A 20 nm thick $Al_{0.2}Ga_{0.8}N$:Mg layer is grown to act as an electron blocking layer followed by a 200 nm thick GaN:Mg layer. Those *p*-type layers are both doped at 1×10^{19} cm^{-3}. Finally, the sample is capped with a 25 nm thick GaN:Mg layer doped at 1×10^{20} cm^{-3} to help with the *p* contact. The samples were processed into 300×300 μm^2 LEDs. The *p*-type contacts are a stack of Pd/Au layers, and the *n*-type contacts are a stack of Ti/Al/Ti/Au layers. In this chapter, the top part (from the GaN:Si spacer to the GaN:Mg cap) of all the samples is kept the same.

Electroluminescence measurements are performed on LEDs with and without any InAlN bulk UL. All the samples are measured with a needle probe on the wafer. To get the power a calibrated photo-diode is place on the backside of the device. The results are shown in Fig. 5.3. The EL spectra at 20 mA for each device is shown in Fig. 5.3(c). The LEDs without InGaN UL emit at 405 nm and the LEDs with an InAlN bulk UL at 412 nm. The shift in wavelength can be attributed to a variation of the built-in field in the Q, due to the band bending induced by the polarization changes between InAlN and GaN (Fig. 5.4). The IQE is computed from the EQE with the method described in Sec. 1.4.3. For each sample, all the available LEDs have been measured. The curves presented in Fig. 5.3 are representative of each structure. The IQE maximum is 9 ±5 % for the sample without UL and is 29 ±5 % for the sample with a bulk UL (Fig. 5.3(a)). The InAlN bulk UL acts in a way similar to an InGaN UL. We improve the IQE maximum by a factor 3 with an InAlN bulk UL, which is the same improvement than an InGaN UL (Fig. 2.1). Furthermore, we can notice that the current density at the IQE maximum is smaller for the sample with an InAlN bulk UL. This is in line with a reduction of the NRCs in the SQW, i.e., a reduction of the A coefficient [12].

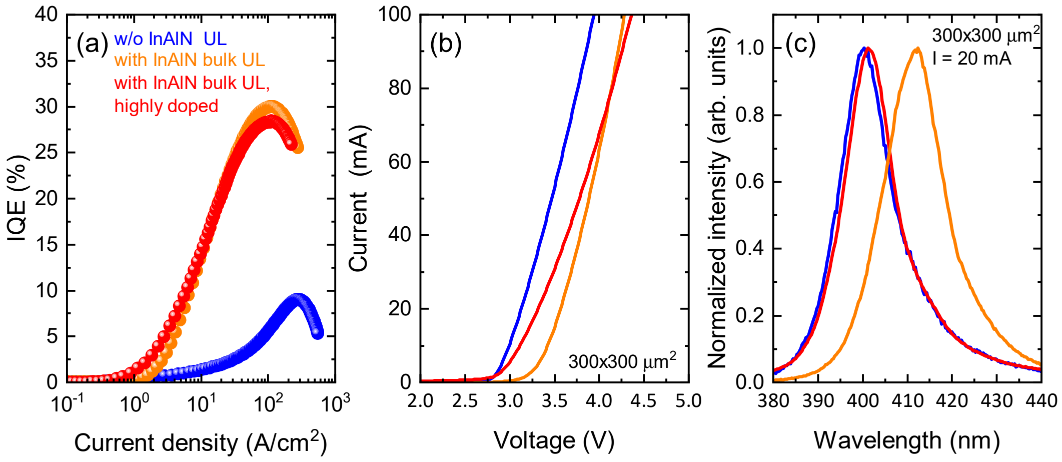

Figure 5.3 – (a) IQE as a function of current density measured on 300×300 μm^2 LEDs. Three different LED structures are shown on this figure: without UL (blue), with an InAlN bulk UL (orange), with an highly doped InAlN bulk UL (red). The structure for each sample can be seen in Figs. 5.1, 5.2(a), 5.2(b). (b) Each I-V curve is derived from the corresponding IQE curve presented in (a). (c) EL spectra taken at 20 mA for each devices.

However, the I-V characteristics for the LED with a bulk InAlN UL exhibits a turn-on voltage higher than the reference LED (Fig. 5.3(b)). At 20 mA, the bias is 3.12 V for the sample without UL and 3.56 V for the sample with an InAlN bulk UL. This trend was observed on all the measured LEDs and is due to the spontaneous polarization mismatch between InAlN and GaN. We will discuss how to overcome this issue later on.

5.2.2 Doping at the interface

LM InAlN has a large spontaneous polarization mismatch with GaN, around 0.038 C/m^2.[1] This leads to a fixed negative charge density of ~ 2×10^{13} cm^{-2}, which creates a barrier for electrons.

A simulation of the band structure shows, as expected, that in the case of an InAlN bulk UL, a strong barrier is present on the n-type side of the junction (Fig. 5.4, orange curve). The simulation was performed with the commercial software NextNano. Therefore, to avoid any additional barrier, a well known strategy is to highly dope the interface between the two materials [87]. We choose to highly dope (1.5×10^{20} cm^{-3}) the last 5 nm of the InAlN bulk UL and the following 5 nm of GaN (Fig. 5.2(b)). The band edge simulation of the highly doped structure (red) is almost the same as the one for LEDs without UL (blue) (Fig. 5.4).

The LED with a highly doped interface is grown in the same reactor than the other two samples (horizontal reactor) on a GaN on sapphire template. The growth conditions are the same as those of the sample with a bulk InAlN UL. Only the UL part is changed to a 45 nm thick InAlN

---

[1] The spontaneous polarization is −0.034 C/m^2 for GaN and −0.072 C/m^2 for $In_{0.17}Al_{0.83}N$, see in Sec. 1.1.2.

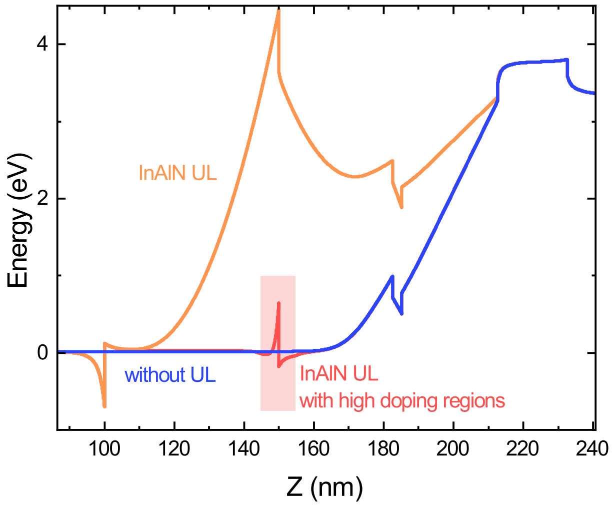

Figure 5.4 – Band edge simulation realized with NexNano of the structure without UL (blue), with an InAlN bulk UL (orange), and with an InAlN bulk UL with high doping at the interface (red).

layer with a n-doping level at 3×10^{18} cm^{-3} followed by a 5 nm thick InAlN layer with a doping level at 1.5×10^{20} cm^{-3} and a 5 nm thick GaN layer with a doping level at 1.5×10^{20} cm^{-3}. The total thickness of InAlN is similar to the sample with a bulk InAlN UL to avoid any difference in the SD density in the SQW.

Electroluminescence measurements are performed on the LEDs with a highly doped interface (Fig. 5.3, in red). The maximum of IQE is 28 ±5 %, which is similar to the LED with an undoped bulk InAlN UL (orange). As both InAlN UL capture the same amount of defects, the current density at the maximum of IQE is similar for the two types of LEDs with InAlN UL, and the IQE maxima are also similar. The emission wavelength at 20 mA is 401 nm, which is matching the one of the LEDs without UL (Fig. 5.3(c)).

The I-V curve for the sample with the highly doped interface is improved compared to its undoped counterpart (Fig. 5.3(b)). Indeed, the voltage at 20 mA is 3.32 V instead of 3.56 V. The reference sample (3.12 V at 20 mA) has still a better I-V characteristic, but the difference is reduced. For higher voltages, the current is still lower than for an LED without UL, and the slope is smaller indicating a higher series resistance for the LED with the highly doped interface. This could still be due to the remaining barrier between InAlN and GaN.

5.3 InAlN/GaN superlattice underlayer

Using our best growth parameters with the horizontal reactor, thick InAlN layers still exhibit a rough morphology, and V-pits due to kinetic roughening, as shown in Ref. [88]. We first grow a sample with only the UL and the spacer to check the surface morphology before the growth of the SQW. A 5×5 μm^2 AFM image of this sample can be seen in Fig. 5.5(a). The surface is full of V-pits. The V-pit density ($\sim 5\times10^9$ cm^{-2}) is higher than the substrate dislocation density (5×10^8 cm^{-2}), which is in good agreement with Ref. [88]. Additionally, we can compare this morphology with the one of a sample without any UL (Fig. 2.4(c)) where the pit density corresponds to the one of the dislocation density. One can notice that the size of the V-pits is smaller. Therefore, as expected, the 50 nm thick InAlN UL changed the surface morphology and promotes pits.

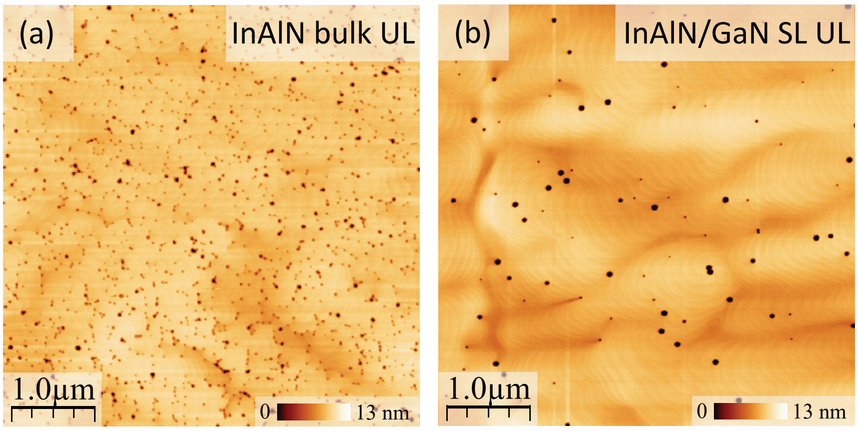

Figure 5.5 – (a) 5×5 μm^2 AFM image of a sample with an InAlN bulk UL where the growth was stopped before the SQW. (b) 5×5 μm^2 AFM image of a sample with an InAlN/GaN (2.1 nm/1.75 nm) SL UL where the growth was stopped before the SQW.

To improve the surface morphology quality, we replace the InAlN bulk UL by an InAlN/GaN SL UL. The role of the GaN layer in the UL is to retrieve the original surface morphology after the growth of the InAlN layer [125]. We chose a 2.1 nm thick InAlN layer according to Ref. [88] where only a slight roughening is observed for 2 nm thick layers. We chose to test the GaN layer thickness (0.75 nm and 1.75 nm) to obtain the optimal value to keep a good surface morphology.

Two samples are grown on GaN on sapphire template with the horizontal reactor (Fig. 5.6). The first sample has an UL made of 24 periods of an InAlN/GaN (2.1 nm/1.75 nm) SL UL, while the second sample has an UL made of 24 periods of an InAlN/GaN (2.1 nm/1.75 nm) SL UL. For all the samples, we have a total amount of InAlN around 50 nm, which should lead to a similar SD capture by the ULs.

IQE curves for both the samples and the reference sample are shown in Fig. 5.7(a). For the LEDs with an InAlN/GaN SL UL of 2.1 nm/0.75 nm, the maximum of IQE is around 37 ± 5 % and the current density at the maximum of IQE around 100 A/cm^2. These values are similar to the sample with an InAlN bulk UL, but the I-V characteristics are improved (Fig. 5.7(b)). The emission wavelength is around 409 nm (Fig. 5.7(c)). The built-in field in the GaN spacer is reduced as the polarization mismatch between the GaN spacer, and the InAlN/GaN SL UL is

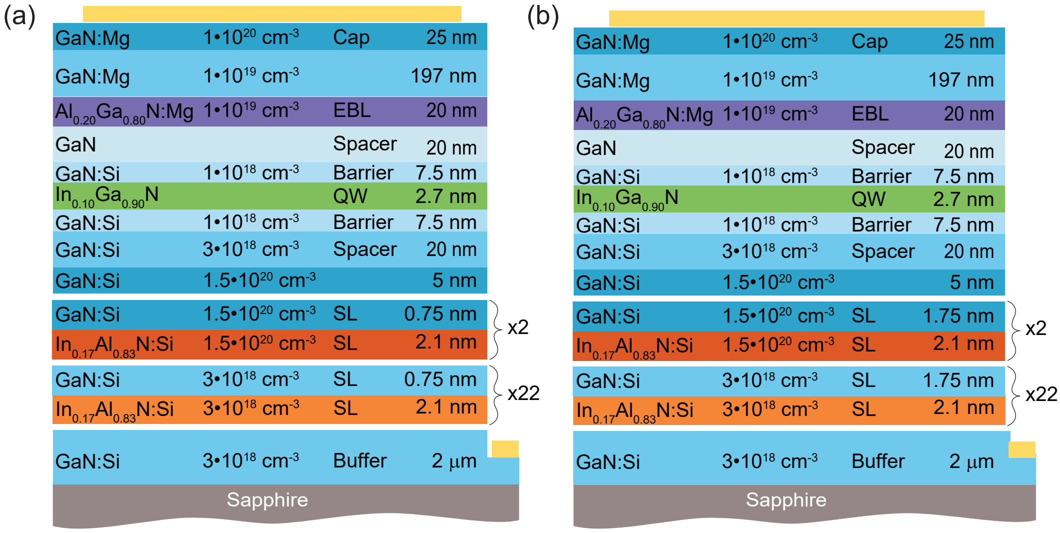

Figure 5.6 – (a) Schematic view of an LED structure with an InAlN/GaN (2.1 nm/0.75 nm) SL UL. (b) Schematic view of an LEDs structure with an InAlN/GaN (2.1 nm/1.75 nm) SL UL.

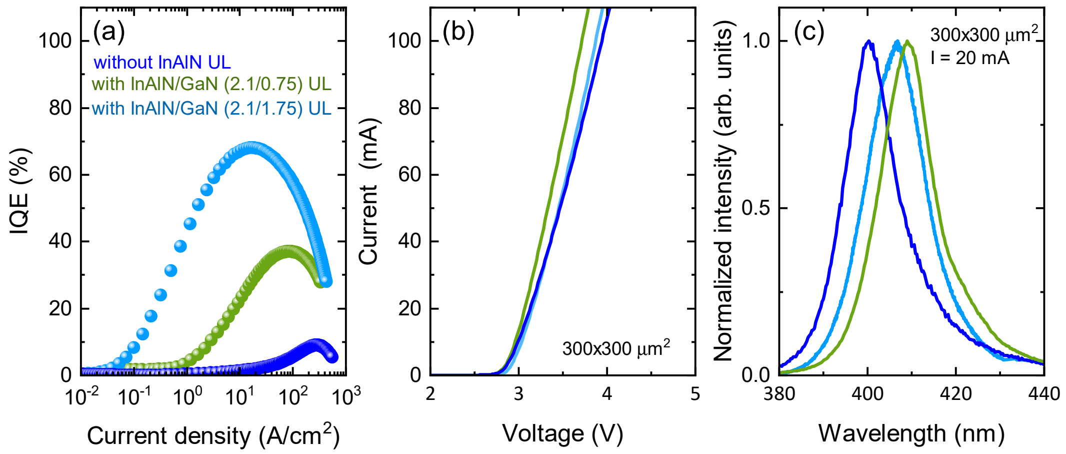

Figure 5.7 – (a) IQE as a function of current density for an LED without UL (blue), with an InAlN/GaN SL UL of 2.1 nm/0.75 nm (green) and with an InAlN/GaN SL UL of 2.1 nm/1.75 nm (light blue). (b) Each I-V curves is related to the corresponding IQE curve presented in (a). (c) EL spectra taken at 20 mA for each device.

smaller. Indeed, on average, the indium content in the SL UL is divided by a factor 2 due to the added thin GaN layer. This probably reduces the barrier for the electrons. For the LEDs with an InAlN/GaN SL UL of 2.1 nm/1.75 nm, the IQE is around 68 ± 5 % with a current density at the maximum of 20 A/cm^2 (Fig. 5.7(a)). Furthermore, the I-V characteristics are similar to that of the reference sample (Fig. 5.6(b)). The drastic increase in the IQE and the reduction of the current density at the IQE maximum can be ascribed to a reduction in the NRCs in the SQWs. However, as the total InAlN layer thickness is constant, the LED efficiency should be the same.

Actually, the surface morphology could play a role. An additional sample was grown to have access to the surface morphology before the SQW for the sample with an InAlN/GaN SL UL of 2.1 nm/1.75 nm. A 5×5 μm^2 AFM image of the surface is shown in Fig. 5.5(b). The density of V-pits present in this image is lower than in the case of an InAlN bulk UL (Fig. 5.5(a)). Their size corresponds to that of the biggest V-pits observed in the AFM image for the InAlN bulk UL. The density of V-pits for the sample with an InAlN/GaN SL UL of 2.1 nm/1.75 nm is around 3×10^8 cm^{-2}, which is close to the dislocation density of the GaN on sapphire template. Therefore, the hypothesis is that the InAlN/GaN SL UL of 2.1 nm/1.75 nm preserve the surface morphology of the sample. In turn, large V-pits create some "dead" areas for light production, which will reduce the active LED surface. Also, V-pits could shortcut the junction thus increasing the current density needed to reach the IQE maximum .

We have shown that the LED with an InAlN/GaN SL UL of 2.1 nm/0.75 nm has a lower IQE than similar InAlN/GaN SL structure with a thicker GaN layer. One explanation could be that a minimum thickness of GaN is needed to smooth the surface, i.e., 0.75 nm (~1.5 mono-layer) is too thin. Further studies are required to fully understand the drastic increase in IQE observed with the InAlN/GaN SL UL of 2.1 nm/1.75 nm.

5.4 EQE vs IQE

In Tab. 5.1, we report all the important parameters for each kind of UL used in this chapter. In this table, we have chosen to indicate the EQE measured for each LED. If we compare these EQE values with those reported in the literature, they could seem rather low. Indeed, EQE higher than 80 % can be found for commercial devices [11]. In our case, our best LEDs have an EQE of 9 %. However, as mentioned before, our LEDs grown on planar sapphire substrate are not diced, i.e., we measured them directly on wafer. Therefore, the light extraction efficiency is quite low. Additionally, the photodiode on the backside of the device collects only the light going through the substrate.

One interesting point about the method used to get the IQE from the EQE measurements is that we get access to the light collection efficiency (Tab. 5.1, last column). It varies from 0.06 to 0.13. However, on average, we get a value of 0.1, which seems to be reasonable. Even if the discussion was based on IQE values, the trend for EQE is similar. Therefore, our conclusions in this chapter are still valid.

Notice that for devices which are not well accounted for by the ABC model, typically LEDs with a large concentration of NRCs in the QW, the IQE method based on the ABC model is not really reliable, see Sec. 1.4.3. Therefore, for devices without UL, the IQE is probably overestimated.

LEDs	EQE [%]	IQE [%]	$J_{\mathrm{max}_{\mathrm{IQE}}}$ [A/cm^2]	V at 20 mA [V]	η_{ext}
without UL	0.5	9±5	270	3.12	~0.06
50 nm thick bulk $In_{0.17}Al_{0.83}N$ UL	3.8	29±5	110	3.56	~0.13
50 nm thick bulk $In_{0.17}Al_{0.83}N$ UL, highly doped	3.1	28±5	110	3.32	~0.11
24× $In_{0.17}Al_{0.83}N$/GaN (2.1 nm/0.75 nm) SL UL	2.9	37±5	100	3.07	~0.08
24× $In_{0.17}Al_{0.83}N$/GaN (2.1 nm/1.75 nm) SL UL	8.4	68±5	20	3.17	~0.12

Table 5.1 – Summary of the main LED parameters for devices described in this chapter.

Summary

In this chapter, we have shown that InAlN UL is as efficient as InGaN UL. Bulk InAlN UL gives an IQE maximum of 28 %. Due to the large polarization mismatch between InAlN and GaN, it is important to highly dope the interface between the UL and the GaN spacer. When combining high doping and an InAlN/GaN SL UL of 2.1 nm/1.75 nm, the IQE maximum can reach 69 % with I-V characteristics similar to that of the reference sample (without UL). To understand why InAlN/GaN SL UL is better than bulk InAlN UL additional work is needed. This opens promising perspectives for the realization of high efficiency near UV LEDs.

Conclusion

Throughout this work, we tried to get a better understanding of the efficiency of InGaN/GaN QWs which form the active region of LEDs and LDs. A systematic study was carried out on the role of the InGaN UL, which is present in all commercial blue LEDs and known to improves greatly the InGaN/GaN QW efficiency. Different hypotheses on the role of the InGaN UL were studied in detail: improvement of the injection efficiency, decrease of the threading dislocation density, promotion of the V-pit formation, impact on the surface morphology, reduction of the QW built-in electric field, decrease of the strain, and suppression of the NRC in the InGaN QW. We found that the main mechanism behind the increase in the blue LED efficiency is the reduction of the NRCs in the QWs.

We proposed that the role of the InGaN UL is to capture surface defects before they reach the InGaN QW. The capture mechanism of those defects by the UL is found to depends on two parameters: the thickness of the UL and its indium content. Furthermore, we evidenced that indium atoms play a key role in the capture of SDs, i.e., a GaN UL does not work, but any indium-containing layer will. For instance, we demonstrated that InAlN could be used as an efficient UL. A model based on the segregation of SDs in the layer was proposed and well account for our results.

The InGaN UL is always placed after the buffer, i.e. after the GaN layer grown at high temperature with TMGa and H_2. We studied the effect of the buffer growth conditions on the InGaN QWs. We tested the effect of the carrier gas and the metalorganic precursors on the creation of SDs without any success. The only parameter which is clearly creating SDs is the growth temperature.

Even if the creation of SDs by the growth temperature is clear, the nature of the SDs itself is not obvious. Two main possibilities have been explored: an impurity or an intrinsic defect. We performed SIMS measurements looking for different kinds of impurity without any conclusive results. Therefore, we suggested that SDs could be intrinsic defect. We proposed a complex between nitrogen vacancy and another type of vacancy as potential candidate. However, we do not have any experimental proof on the actual nature of SDs. This subject is still an open question.

Finally, we applied our findings to NUV LEDs. LEDs with a bulk LM InAlN UL and a LM

InAlN/GaN SL UL were designed and measured. As expected, the IQE of LEDs with a bulk InAlN UL (~ 30 %) was improved vs that of LED without UL (~ 9 %). The IQE was further increased (~ 70 %) with a LM InAlN/GaN SL UL. This is probably due to the better surface morphology in the case of an InAlN/GaN SL.

Outlook

We demonstrated that the role of the InGaN UL in LEDs is to capture SDs thanks to indium and that SDs are created by the growth temperature. However, several questions are still open:

- The growth temperature controls the SD density, but the actual formation mechanism is still unclear as the activation energy we found is not realistic. Indeed, if we suppose a thermodynamic equilibrium, the activation energy is too high to produce enough SDs. Therefore, a kinetic process might be at play. An extensive study on the creation mechanism of SDs depending on the growth rate and the pressure is worth to be to carried out.
- We were not able to determine the exact nature of SDs. Theoretical calculations could help with their identification.
- On the device point of view, an optimization of the InAlN/GaN SL UL could improve the LED efficiency in the NUV range.
- Finally, as we control the density of SDs, we may try to understand the role of those defects on indium incorporation, relaxation, doping, etc.

In conclusion, the work on SDs is just starting. Probably, with new experiments and time, we will get a better insight into their incorporation, creation, and nature.

A Additional experiments

In this appendix, we propose some additional experiments about the UL, which are realized to get a better understanding of some of the mechanisms we observed during this work.

A.1 Effect of the InGaN UL on InGaN/AlGaN QWs

In this section, we checked that AlGaN was not impacting the SD segregation. For this purpose, we changed the GaN barriers by AlGaN barriers and checked that the InGaN UL still improve SQW efficiency. As the growth temperature plays a role in the creation of SDs, the AlGaN was grown at low temperature (770 °C) to avoid any creation of SDs.

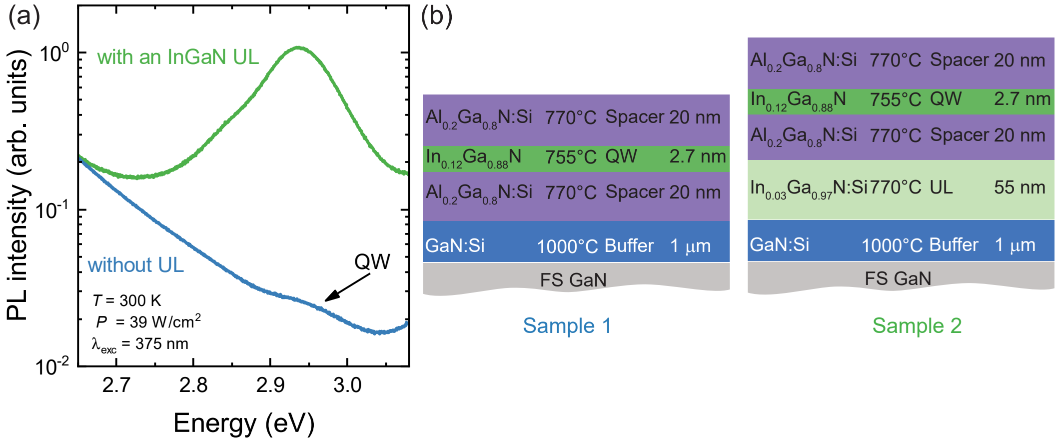

Figure A.1 – (a) PL spectra recorded under quasi-resonant pumping at 300 K with a 375 nm laser for a sample without UL and with an InGaN UL. (b) Schematic view of the two sample structures measured in (a).

Two samples are prepared on FS-GaN substrate with the showerhead reactor. The GaN:Si buffer is grown with TMGa at 1000 °C under H_2. Then, the carrier gas is switched to N_2, and the temperature is decreased to 770 °C. For the sample with an InGaN UL, a 55 nm thick

$In_{0.03}Ga_{0.97}N$ UL is deposited with TEGa and TMIn (Fig. A.1(b), sample 2). In the case of the sample without UL, the $Al_{0.2}Ga_{0.8}N$:Si spacer is directly grown (Fig. A.1(b), sample 1). For both samples, the top part is similar. A 20 nm thick $Al_{0.2}Ga_{0.8}N$:Si spacer is deposited with TMAl and TEGa. Then the temperature is decreased to 755 °C for the InGaN SQW layer. The SQW is capped by a 20 nm thick $Al_{0.2}Ga_{0.8}N$:Si layer grown at 770 °C.

Quasi-resonant PL is performed on these two samples with a 375 nm laser (Fig. A.1(a)). The QW PL intensity for the sample with an InGaN UL is higher than for the sample without UL. For the sample without UL, we can barely see the InGaN SQW. We can conclude that AlGaN layers are not stopping the SD segregation, which can be interesting information for laser diodes as the cladding is often made of AlGaN. Therefore, InGaN UL is useful for InGaN/AlGaN QWs.

A.2 Effect of the InGaN UL on GaN/AlGaN QWs

In the last section, we have shown that AlGaN is not stopping the SD segregation. The incorporation of SDs in GaN was shown to be really inefficient (Fig. 3.7(a)). Therefore, the InGaN UL should not improve GaN/AlGaN QWs.

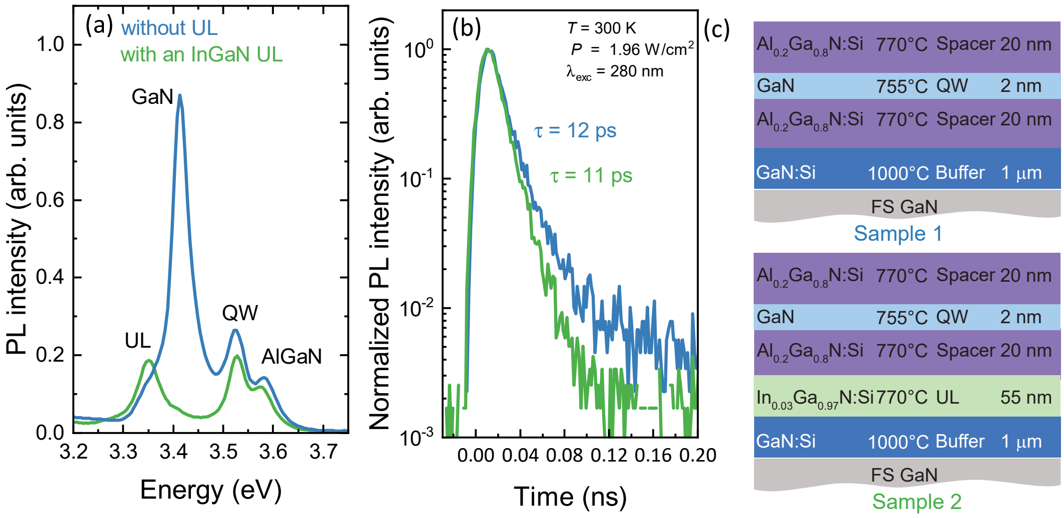

Figure A.2 – (a) PL spectra measured at 300 K with a 280 nm pulsed laser for GaN/AlGaN SQW samples without UL and with an InGaN UL. (b) Normalized QW PL decay trace corresponding to the spectra displayed in (a). (c) Sample structures used in (a) and (b).

To check this hypothesis, we grew two samples with the same growth conditions as the sample used in Sec. A.1, but with a 2 nm thick GaN SQW instead of an InGaN QW. The sample structures can be seen in Fig. A.2(c).

We performed PL and TRPL measurements with a 280 nm pulsed laser on these two samples (Fig. A.2(a) and (b)). On the PL spectra, several peaks can be observed. For the sample with an

InGaN UL, four peaks can be seen: the InGaN UL (~ 3.35 eV), the GaN band-edge (~ 3.4 eV), the GaN/AlGaN SQW (~ 3.54 eV), and the $Al_{0.2}Ga_{0.8}N$ band-edge (~ 3.58 eV), (Fig. A.2(a)). For the sample without UL, only three peaks can be observed, and the GaN band-edge is more intense as the carrier will recombine in the GaN buffer instead of the InGaN UL. The QW intensity for the sample without UL is a bit higher than for the sample with an InGaN UL. This can be due to the number of carriers present in the QW which could be more important in the case without UL. The normalized PL decay traces for the GaN/AlGaN SQWs are shown in Fig. A.2(b). The effective lifetime for both samples is similar: 12 ps for the sample without UL and 11 ps for the sample with an InGaN UL. We can conclude that the InGaN UL has no effect on the GaN/AlGaN SQWs, which is expected as GaN/AlGaN SQWs have no indium atoms to capture SDs and create NRCs. One can also remark that the lifetime is very short indicating another source of NRCs.

A.3 Effect of growth interruption on the creation of SDs

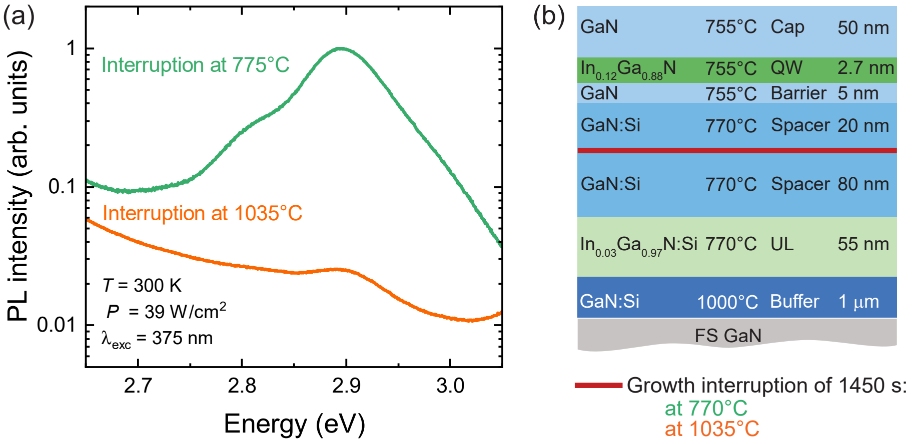

Figure A.3 – (a) PL spectra recorded under quasi-resonant pumping at 300 K with a 375 nm laser for a sample with a growth interruption at 770 °C and at 1035 °C. (b) Schematic view of the two sample structures measured in (a).

In Ch. 4, we observe that SDs are created during the GaN growth at HT which probably affects the GaN surface stability. We also demonstrated that SDs can be created during a growth interruption at 820 °C when the NH_3 supply is closed. In this section, we perform two growth interruptions at different temperatures under constant pressure with NH_3 and N_2.

The two samples are grown with the showerhead reactor on FS-GaN substrate. A 1 μm thick GaN:Si buffer is grown with TMGa under H_2. As usual, the temperature is decreased to 770 °C and the carrier gas is switched to N_2. A 55 nm thick $In_{0.03}Ga_{0.97}N$ UL is grown with TMIn and TEGa followed by an 80 nm thick GaN:Si spacer. A 1450 s long growth interruption is performed under a constant pressure with NH_3 and N_2 to stabilize the surface. This growth interruption is done at two different temperatures: 770 °C (reference sample) and 1035 °C. The temperature is then stabilized at 770 °C, and the top part of the sample is grown. A 20 nm thick GaN:Si spacer grown with TEGa is deposited followed by a 5 nm thick GaN barrier, a 2.7 nm thick InGaN QW and a 50 nm thick GaN cap. The structure is shown in Fig. A.3(b).

To test the efficiency of the SQW, quasi-resonant PL with a 375 nm CW laser is performed. The SQW PL intensity is shown in Fig. A.3(a). The intensity of the sample with an interruption at 770 °C is higher than the one with an interruption at 1035 °C. Therefore, we can conclude that the SQW with the HT interruption has more SDs.

A.4 Effective lifetime behavior with temperature

One of the hypotheses made in this work is that the radiative lifetime for the SQW is the same. Therefore, we can interpret a change at room temperature on the effective lifetime as a change in the non-radiative lifetime. In this section, we report the effective lifetime behavior as a function of temperature for two samples: one with a GaN spacer at low temperature and one with a GaN spacer at high temperature.

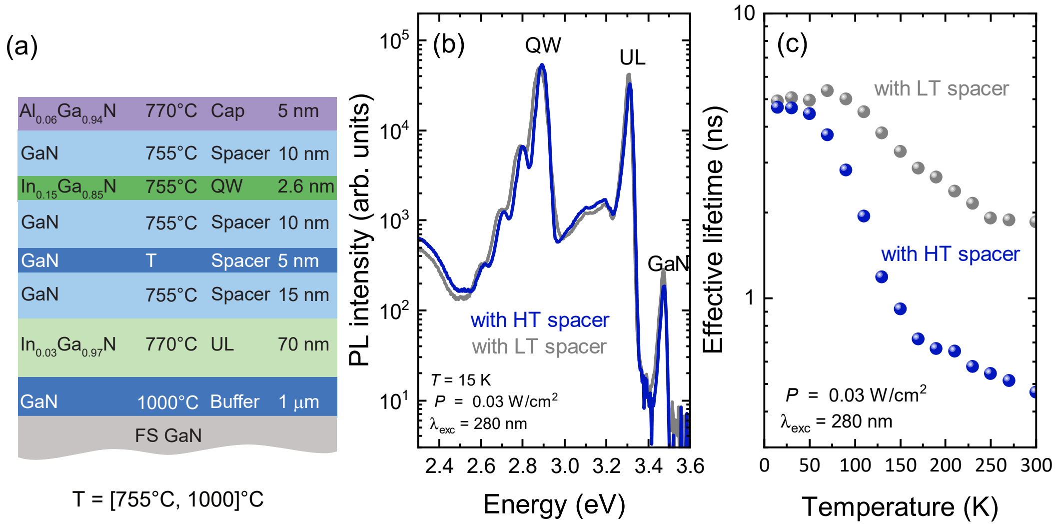

Figure A.4 – (a) Sample structures used in this section. The 5 nm thick GaN spacer is grown at two different temperatures (755 and 1000 °C) to change the density of SDs in the SQWs. (b) PL spectra taken at 15 K with a 280 nm pulsed laser for the sample with LT spacer and with HT spacer. (c) Evolution of the SQW effective lifetime as a function of temperature for both samples. Courtesy of T. Weatherley

Two sample are grown with the horizontal reactor on FS-GaN substrate. The structure is shown in Fig. A.4(a). The GaN buffer is grown with TMGa under H_2 at 1000 °C. Then the temperature is lowered to 770 °C, and the carrier gas switched to N_2. A 55 nm thick $In_{0.03}Ga_{0.97}N$ UL is grown with TMIn and TEGa followed by a 15 nm thick GaN spacer grown at 755 °C. A 5 nm thick GaN layer will be used here to change the amount of SDs present in the SQW. This layer was either grown at 755 °C for the LT spacer sample or at 1000 °C for the HT sample. On top of this layer, a 10 nm thick GaN spacer is grown at 755 °C followed by a 2.7 nm thick $In_{0.15}Ga_{0.85}N$ QW, a 10 nm thick GaN layer. A 5 nm AlGaN cap is deposited on top of these structures with TMAl, TEGa at 770 °C. The SQW will be affected by the 5 nm thick GaN layer grown at HT or LT.

In Fig. A.4(b), the PL spectra are shown. They were measured at 15 K with the 280 nm pulsed laser. The two spectra are almost similar, and the SQW intensities are comparable as most of the NRCs are inactive at 15 K. The SQW effective lifetime as a function of temperature for both samples is reported in Fig. A.4(c). At 15 K, both samples have an effective lifetime close to 5 ns. When the temperature is increased, NRCs become active and the effective lifetime drops. As expected from previous results, the SQW with a spacer at HT has a shorter effective lifetime at 300 K (0.470 ns) than the SQW with a LT spacer (1.8 ns). These results confirm that the radiative lifetime in the two samples is similar and that the growth temperature is only affecting the NRC density in the SQW. We can safely analyze the changes in the SQW effective lifetime at room temperature as a variation in the NR lifetime.

B Structure and sample name

In this appendix, all the sample used in this work is named and a quick description is given. The samples with a name beginning with the letter C are grown in the showerhead reactor. The sample with a name beginning with the letter A are grown in the horizontal reactor.

Sample	Chapter	Series	Substrate	Quick description
C2245	2	-	Sapphire	SQW LED without InGaN UL
C2265	2	-	Sapphire	SQW LED with InGaN UL
C2492	2	-	Sapphire	similar structure as in Fig.2.1 with InGaN UL and without the QW and the cap.
C2493	2	-	Sapphire	similar structure as in Fig.2.1 without InGaN UL and without the QW and the cap.
C2575	2	-	FS-GaN	see Fig.2.10, without an InGaN UL
C2576	2	-	FS-GaN	see Fig.2.10, with an InGaN UL
C2655	4	-	FS-GaN	see Fig.2.8, sample B
C2656	2, 4	Spacer thickness	FS-GaN	see Fig.2.8, with a spacer of 20 nm
C2657	2	Spacer thickness	FS-GaN	see Fig.2.8, with a spacer of 50 nm
C2658	2	Spacer thickness	FS-GaN	see Fig.2.8, with a spacer of 100 nm
C2686	A	Interruption	FS-GaN	see Fig.A.3, with an interruption at 1035 °C
C2687	A	Interruption	FS-GaN	see Fig.A.3, with an interruption at 770 °C

Sample	Chapter	Series	Substrate	Quick description
C2707	4	Spacer temperature	FS-GaN	see Fig.4.5, with T_{spacer} = 900 °C
C2708	4	Spacer temperature	FS-GaN	see Fig.4.5, with T_{spacer} = 770 °C
C2709	4	Spacer temperature	FS-GaN	see Fig.4.5, with T_{spacer} = 850 °C
C2710	4	Spacer temperature	FS-GaN	see Fig.4.5, with T_{spacer} = 990 °C
C2720	4	Spacer temperature	FS-GaN	same structure as in Fig.4.5, with T_{spacer} = 990 °C without the cap and the QW
C2721	4	Spacer temperature	FS-GaN	same structure as in Fig.4.5, with T_{spacer} = 770 °C without the cap and the QW
C2722	2	InGaN UL thickness	FS-GaN	see Fig.3.1, with 10 nm InGaN UL
C2723	2, 3	InGaN UL thickness	FS-GaN	see Fig.3.1, without UL
C2724	2, 3	InGaN UL thickness	FS-GaN	see Fig.3.1, with 55 nm InGaN UL
C2725	3	InGaN UL thickness	FS-GaN	see Fig.3.1, with 5 nm InGaN UL
C2739	2	-	Sapphire	see Fig.2.1, without UL
C2740	2	-	Sapphire	see Fig.2.1, with UL
C2745	3	InGaN UL thickness	FS-GaN	see Fig.3.1, with 110 nm InGaN UL
C2746	3	InGaN UL thickness	FS-GaN	see Fig.3.1, with 220 nm InGaN UL
C2779	A	AlGaN/GaN SQW	FS-GaN	see Fig. A.2 , without UL
C2791	A	AlGaN/GaN SQW	FS-GaN	see Fig. A.2, with an InGaN UL
C2851	2	-	FS-GaN	similar structure as in Fig.2.1, with InGaN UL and without the QW and the cap.

Sample	Chapter	Series	Substrate	Quick description
C2852	2	-	FS-GaN	similar structure as in Fig.2.1, without InGaN UL and without the QW and the cap.
C2880	4	Spacer temperature	FS-GaN	see Fig.4.5, with T_{spacer} = 935 °C
C2881	4	Spacer temperature	FS-GaN	see Fig.4.5, with T_{spacer} = 1020 °C
C2882	4	NH_3	FS-GaN	see Fig.4.12(c), with 6000 sscm
C2883	4	NH_3	FS-GaN	see Fig.4.12(c), with 1000 sscm
C2884	4	NH_3	FS-GaN	see Fig.4.12(c), with 0 sscm
C2902	3	LT GaN UL thickness	FS-GaN	see Fig.3.1, with 55 nm LT GaN UL
C2903	3	LT GaN UL thickness	FS-GaN	see Fig.3.1, with 110 nm LT GaN UL
C2904	3	LT GaN UL thickness	FS-GaN	see Fig.3.1, with 220 nm LT GaN UL
C3179	4	Gas variation	FS-GaN	see Fig.4.2(a)
C3182	4	Gas variation	FS-GaN	see Fig.4.2(b)
C3193	4	Buffer temperature	FS-GaN	see Fig. 4.8(a), with T_{buffer} = 1050 °C
C3206	4	Buffer temperature	FS-GaN	see Fig. 4.8(a), with T_{buffer} = 875 °C
C3223	4	Buffer temperature	FS-GaN	see Fig. 4.8(a), with T_{buffer} = 910 °C
C3224	4	Buffer temperature	FS-GaN	see Fig. 4.8(a), with T_{buffer} = 995 °C

Sample	Chapter	Series	Substrate	Quick description
A3654	3	InGaN UL composition	Sapphire	see Fig.3.1, with an indium content of 0.42 %
A3655	3	InGaN UL composition	Sapphire	see Fig.3.1, with an indium content of 5.3 %
A3656	3	InGaN UL composition	Sapphire	see Fig.3.1, with an indium content of 2.3 %
A3659	3	InGaN UL composition	Sapphire	see Fig.3.1, with an indium content of 0.42 %
A3663	3	InGaN UL composition	Sapphire	see Fig.3.1, with an indium content of 21 %
A3664	3	InGaN UL composition	Sapphire	see Fig.3.1, with an indium content of 15.5 %
A3665	3	InGaN UL composition	Sapphire	see Fig.3.1, with an indium content of 12.7 %
A3671	3	InGaN UL composition	Sapphire	see Fig.3.1, with an indium content of 9.7 %
A3716	3	InAlN UL thickness	FS-GaN	see Fig.3.1, with 0 nm InAlN UL
A3717	3	InAlN UL thickness	FS-GaN	see Fig.3.1, with 50 nm InAlN UL
A3729	3	InAlN UL thickness	FS-GaN	see Fig.3.1, with 20 nm InAlN UL
A3730	3	InAlN UL thickness	FS-GaN	see Fig.3.1, with 5 nm InAlN UL
A3731	3	InAlN UL thickness	FS-GaN	see Fig.3.1, with 10 nm InAlN UL
A3781	3	InAlN UL thickness	FS-GaN	see Fig.3.1, with 120 nm InAlN UL

Sample	Chapter	Series	Substrate	Quick description
A3808	5	InAlN UL LEDs	Sapphire	see Fig. 5.2(b)
A3810	5	InAlN UL LEDs	Sapphire	see Fig. 5.1
A3812	5	InAlN UL LEDs	Sapphire	see Fig. 5.6(b)
A3813	5	InAlN UL LEDs	Sapphire	see Fig. 5.2(a)
A3814	5	InAlN UL LEDs	Sapphire	see Fig. 5.6(a)
A3834	5	Morphologie	Sapphire	similar as structure in Fig. 5.6(b) without the *p*-type and the QW
A3835	5	Morphologie	Sapphire	similar as structure in Fig. 5.2(b) without the *p*-type and the QW

Bibliography

[1] T. A. Edison, “Electric lamp”, US patent, US223898A (1880).

[2] S. Pimputkar, J. S. Speck, S. P. DenBaars, and S. Nakamura, “Prospects for LED lighting”, Nature Photonics **3**, 180–182 (2009).

[3] P. Pust, P. J. Schmidt, and W. Schnick, “A revolution in lighting”, Nature Materials **14**, 454–458 (2015).

[4] H. Amano, N. Sawaki, I. Akasaki, and Y. Toyoda, “Metalorganic vapor phase epitaxial growth of a high quality GaN film using an AlN buffer layer”, Applied Physics Letters **48**, 353–355 (1986).

[5] H. Amano, M. Kito, K. Hiramatsu, and I. Akasaki, “P-Type Conduction in Mg-Doped GaN Treated with Low-Energy Electron Beam Irradiation (LEEBI)”, Japanese Journal of Applied Physics **28**, L2112–L2114 (1989).

[6] S. Nakamura, T. Mukai, M. Senoh, and N. Iwasa, “Thermal annealing effects on p-type Mg-doped GaN Films”, Japanese Journal of Applied Physics **31**, L139 (1992).

[7] S. Nakamura, T. Mukai, and M. Senoh, “Candela-class high-brightness InGaN/AlGaN double-heterostructure blue-light-emitting diodes”, Applied Physics Letters **64**, 1687–1689 (1994).

[8] S. Nakamura, M. Senoh, S.-i. Nagahama, N. Iwasa, T. Yamada, T. Matsushita, H. Kiyoku, and Y. Sugimoto, “InGaN-Based Multi-Quantum-Well-Structure Laser Diodes”, Japanese Journal of Applied Physics **35**, L74–L76 (1996).

[9] S. Nakamura, “Background Story of the Invention of Efficient InGaN Blue-Light-Emitting Diodes (Nobel Lecture)”, Angewandte Chemie International Edition **54**, 7770–7788 (2015).

[10] T. Fujii, Y. Gao, R. Sharma, E. L. Hu, S. P. DenBaars, and S. Nakamura, “Increase in the extraction efficiency of GaN-based light-emitting diodes via surface roughening”, Applied Physics Letters **84**, 855–857 (2004).

[11] S. P. DenBaars, D. Feezell, K. Kelchner, S. Pimputkar, C.-C. Pan, C.-C. Yen, S. Tanaka, Y. Zhao, N. Pfaff, R. Farrell, M. Iza, S. Keller, U. Mishra, J. S. Speck, and S. Nakamura, “Development of gallium-nitride-based light-emitting diodes (LEDs) and laser diodes for energy-efficient lighting and displays”, Acta Materialia **61**, 945–951 (2013).

[12] A. David, N. G. Young, C. A. Hurni, and M. D. Craven, “Quantum Efficiency of III-Nitride Emitters: Evidence for Defect-Assisted Nonradiative Recombination and its Effect on the Green Gap”, Physical Review Applied **11**, 031001 (2019).

[13] S. Limpijumnong and W. R. L. Lambrecht, “Homogeneous Strain Deformation Path for the Wurtzite to Rocksalt High-Pressure Phase Transition in GaN”, Physical Review Letters **86**, 91–94 (2001).

[14] R. Butté and N. Grandjean, “Effects of Polarization in Optoelectronic Quantum Structures”, in C. Wood and D. Jena (Editors), “Polarization Effects in Semiconductors”, pages 467–511, (Springer US, Boston, MA, 2008).

[15] F. Bernardini, V. Fiorentini, and D. Vanderbilt, “Spontaneous polarization and piezoelectric constants of III-V nitrides”, Physical Review B **56**, R10024 (1997).

[16] O. Ambacher, J. Majewski, C. Miskys, A. Link, M. Hermann, M. Eickhoff, M. Stutzmann, F. Bernardini, V. Fiorentini, V. Tilak, B. Schaff, and L. F. Eastman, “Pyroelectric properties of Al(In)GaN/GaN hetero- and quantum well structures”, Journal of Physics: Condensed Matter **14**, 3399–3434 (2002).

[17] V. Fiorentini, F. Bernardini, and O. Ambacher, “Evidence for nonlinear macroscopic polarization in III–V nitride alloy heterostructures”, Applied Physics Letters **80**, 1204–1206 (2002).

[18] J. Wu, W. Walukiewicz, W. Shan, K. M. Yu, J. W. Ager, S. X. Li, E. E. Haller, H. Lu, and W. J. Schaff, “Temperature dependence of the fundamental band gap of InN”, Journal of Applied Physics **94**, 4457–4460 (2003).

[19] M. Feneberg, B. Neuschl, K. Thonke, R. Collazo, A. Rice, Z. Sitar, R. Dalmau, J. Xie, S. Mita, and R. Goldhahn, “Sharp bound and free exciton lines from homoepitaxial AlN”, physica status solidi (a) **208**, 1520–1522 (2011).

[20] K. Kornitzer, T. Ebner, K. Thonke, R. Sauer, C. Kirchner, V. Schwegler, M. Kamp, M. Leszczynski, I. Grzegory, and S. Porowski, “Photoluminescence and reflectance spectroscopy of excitonic transitions in high-quality homoepitaxial GaN films”, Physical Review B **60**, 1471–1473 (1999).

[21] M. Leroux, N. Grandjean, B. Beaumont, G. Nataf, F. Semond, J. Massies, and P. Gibart, “Temperature quenching of photoluminescence intensities in undoped and doped GaN”, Journal of Applied Physics **86**, 3721–3728 (1999).

[22] I. Vurgaftman and J. R. Meyer, "Band parameters for nitrogen-containing semiconductors", Journal of Applied Physics **94**, 3675 (2003).

[23] L. Lymperakis, T. Schulz, C. Freysoldt, M. Anikeeva, Z. Chen, X. Zheng, B. Shen, C. Chèze, M. Siekacz, X. Q. Wang, M. Albrecht, and J. Neugebauer, "Elastically frustrated rehybridization: Origin of chemical order and compositional limits in InGaN quantum wells", Physical Review Materials **2**, 011601(R) (2018).

[24] Y. P. Varshni, "Temperature dependence of the energy gap in semiconductors", Physica **34**, 149–154 (1967).

[25] E. Rosencher and B. Vinter, Optoelectronics (Cambridge University Press, Cambridge, 2002).

[26] S.-H. Park, "Crystal orientation effects on electronic properties of wurtzite InGaN/GaN quantum wells", Journal of Applied Physics **91**, 9904 (2002).

[27] A. Hangleiter, F. Hitzel, S. Lahmann, and U. Rossow, "Composition dependence of polarization fields in GaInN/GaN quantum wells", Applied Physics Letters **83**, 1169–1171 (2003).

[28] N. Grandjean, B. Damilano, S. Dalmasso, M. Leroux, M. Laügt, and J. Massies, "Built-in electric-field effects in wurtzite AlGaN/GaN quantum wells", Journal of Applied Physics **86**, 3714–3720 (1999).

[29] M. Leroux, M. Laugt, J. Massies, and N. Grandjean, "Quantum confined Stark effect due to built-in internal polarization fields in Al,GaN/GaN quantum wells", Physical Review B **58**, R13 371 (1998).

[30] T. Miyoshi, S. Masui, T. Okada, T. Yanamoto, T. Kozaki, S.-i. Nagahama, and T. Mukai, "510–515 nm InGaN-Based Green Laser Diodes on c -Plane GaN Substrate", Applied Physics Express **2**, 062201 (2009).

[31] S. Lutgen, A. Avramescu, T. Lermer, D. Queren, J. Müller, G. Bruederl, and U. Strauss, "True green InGaN laser diodes", physica status solidi (a) **207**, 1318–1322 (2010).

[32] T. H. Ngo, B. Gil, B. Damilano, K. Lekhal, and P. De Mierry, "Internal quantum efficiency and Auger recombination in green, yellow and red InGaN-based light emitters grown along the polar direction", Superlattices and Microstructures **103**, 245–251 (2017).

[33] M. Glauser, C. Mounir, G. Rossbach, E. Feltin, J.-F. Carlin, R. Butté, and N. Grandjean, "InGaN/GaN quantum wells for polariton laser diodes: Role of inhomogeneous broadening", Journal of Applied Physics **115**, 233511 (2014).

[34] S. D. Lester, F. A. Ponce, M. G. Craford, and D. A. Steigerwald, "High dislocation densities in high efficiency GaN-based light-emitting diodes", Applied Physics Letters **66**, 1249–1251 (1995).

[35] Y. Narukawa, M. Ichikawa, D. Sanga, M. Sano, and T. Mukai, "White light emitting diodes with super-high luminous efficacy", Journal of Physics D: Applied Physics **43**, 354002 (2010).

[36] I. E. Titkov, S. Y. Karpov, A. Yadav, V. L. Zerova, M. Zulonas, B. Galler, M. Strassburg, I. Pietzonka, H. Lugauer, and E. U. Rafailov, "Temperature-Dependent Internal Quantum Efficiency of Blue High-Brightness Light-Emitting Diodes", IEEE Journal of Quantum Electronics **50**, 911–920 (2014).

[37] M. J. Davies, F. C.-P. Massabuau, P. Dawson, R. A. Oliver, M. J. Kappers, and C. J. Humphreys, "Effects of an InGaN prelayer on the properties of InGaN/GaN quantum well structures", physica status solidi (c) **11**, 710–713 (2014).

[38] S. Chichibu, T. Azuhata, T. Sota, and S. Nakamura, "Spontaneous emission of localized excitons in InGaN single and multiquantum well structures", Applied Physics Letters **69**, 4188–4190 (1996).

[39] Y. Narukawa, Y. Kawakami, S. Fujita, S. Fujita, and S. Nakamura, "Recombination dynamics of localized excitons in $In_{0.20}Ga_{0.80}N$- $In_{0.05}Ga_{0.95}N$ multiple quantum wells", Physical Review B **55**, R1938–R1941 (1997).

[40] Y.-H. Cho, G. H. Gainer, A. J. Fischer, J. J. Song, S. Keller, U. K. Mishra, and S. P. DenBaars, ""S-shaped" temperature-dependent emission shift and carrier dynamics in InGaN/GaN multiple quantum wells", Applied Physics Letters **73**, 1370 (1998).

[41] E. F. Schubert, Light-Emitting Diodes, (Cambridge University Press, Cambrige, 2006).

[42] W. Shockley, "The Theory of p-n Junctions in Semiconductors and p-n Junction Transistors", Bell System Technical Journal **28**, 435–489 (1949).

[43] S. M. Sze and M.-K. Lee, Semiconductor devices : physics and technology, (Wiley, Hoboken, N.J, 3rd ed., International student version, 2013).

[44] S. Sze and K. K. Ng, "LEDs and Lasers", in "Physics of Semiconductor Devices", pages 599–662, (John Wiley & Sons, Inc., Hoboken, NJ, USA, 2006).

[45] R. N. Hall, "Electron-Hole Recombination in Germanium", Physical Review **87**, 387–387 (1952).

[46] W. Shockley and W. T. Read, "Statistics of the Recombinations of Holes and Electrons", Physical Review **87**, 835–842 (1952).

[47] C. E. Dreyer, A. Alkauskas, J. L. Lyons, J. S. Speck, and C. G. Van de Walle, "Gallium vacancy complexes as a cause of Shockley-Read-Hall recombination in III-nitride light emitters", Applied Physics Letters **108**, 141101 (2016).

[48] A. Armstrong, A. R. Arehart, and S. A. Ringel, “A method to determine deep level profiles in highly compensated, wide band gap semiconductors”, Journal of Applied Physics **97**, 083529 (2005).

[49] H. P. Maruska and J. J. Tietjen, “The preparation and properties of vapor-deposited single-crystal-line GaN”, Applied Physics Letters **15**, 327–329 (1969).

[50] L. Liu and J. Edgar, “Substrates for gallium nitride epitaxy”, Materials Science and Engineering: R: Reports **37**, 61–127 (2002).

[51] K. Motoki, “Development of Gallium Nitride Substrates”, SEI Technical Review **70**, 28 (2010).

[52] Q. Dai, Q. Shan, J. Wang, S. Chhajed, J. Cho, E. F. Schubert, M. H. Crawford, D. D. Koleske, M.-H. Kim, and Y. Park, “Carrier recombination mechanisms and efficiency droop in GaInN/GaN light-emitting diodes”, Applied Physics Letters **97**, 133507 (2010).

[53] S. Nakamura, N. Iwasa, M. Senoh, and T. Mukai, “Hole Compensation Mechanism of p-Type GaN Films”, Japanese Journal of Applied Physics **31**, 1258 (1992).

[54] W. Götz, N. M. Johnson, J. Walker, D. P. Bour, H. Amano, and I. Akasaki, “Hydrogen passivation of Mg acceptors in GaN grown by metalorganic chemical vapor deposition”, Applied Physics Letters **67**, 2666–2668 (1995).

[55] J. Neugebauer and C. G. Van de Walle, “Hydrogen in GaN: Novel Aspects of a Common Impurity”, Physical Review Letters **75**, 4452–4455 (1995).

[56] T. Akasaka, H. Gotoh, T. Saito, and T. Makimoto, “High luminescent efficiency of InGaN multiple quantum wells grown on InGaN underlying layers”, Applied Physics Letters **85**, 3089 (2004).

[57] Y. Takahashi, A. Satake, K. Fujiwara, J. K. Shue, U. Jahn, H. Kostial, and H. T. Grahn, “Enhanced radiative efficiency in blue (In,Ga)N multiple-quantum-well light-emitting diodes with an electron reservoir layer”, Physica E **21**, 876–880 (2004).

[58] N. Otsuji, K. Fujiwara, and J. K. Sheu, “Electroluminescence efficiency of blue InGaN/-GaN quantum-well diodes with and without an n-InGaN electron reservoir layer”, Journal of Applied Physics **100**, 113105 (2006).

[59] N. Nanhui, W. Huaibing, L. Jianping, L. Naixin, X. Yanhui, H. Jun, D. Jun, and S. Guangdi, “Improved quality of InGaN/GaN multiple quantum wells by a strain relief layer”, Journal of Crystal Growth **286**, 209–212 (2006).

[60] J.-W. Ju, E.-S. Kang, H.-S. Kim, L.-W. Jang, H.-K. Ahn, J.-W. Jeon, I.-H. Leea, and J. H. Baek, “Metal-organic chemical vapor deposition growth of InGaN/GaN high power green light emitting diode: Effects of InGaN well protection and electron reservoir layer”, Journal of Applied Physics **102**, 053519 (2007).

[61] P. Törmä, O. Svensk, M. Ali, S. Suihkonen, M. Sopanen, M. Odnoblyudov, and V. Bougrov, "Effect of InGaN underneath layer on MOVPE-grown InGaN/GaN blue LEDs", Journal of Crystal Growth **310**, 5162–5165 (2008).

[62] Y. Xia, W. Hou, L. Zhao, M. Zhu, T. Detchprohm, and C. Wetzel, "Boosting Green GaInN/GaN Light-Emitting Diode Performance by a GaInN Underlying Layer", IEEE Transactions on Electron Devices **57**, 2639–2643 (2010).

[63] M. J. Davies, P. Dawson, F. C.-P. Massabuau, A. L. Fol, R. A. Oliver, M. J. Kappers, and C. J. Humphreys, "A study of the inclusion of prelayers in InGaN/GaN single- and multiple-quantum-well structures", physica status solidi (b) **252**, 866–872 (2015).

[64] A. M. Armstrong, B. N. Bryant, M. H. Crawford, D. D. Koleske, S. R. Lee, and J. J. Wierer, "Defect-reduction mechanism for improving radiative efficiency in InGaN/GaN light-emitting diodes using InGaN underlayers", Journal of Applied Physics **117**, 134501 (2015).

[65] J.-Y. Park, J.-H. Lee, S. Jung, and T. Ji, "InGaN/GaN-based green light-emitting diodes with an inserted InGaN/GaN-graded superlattice layer", physica status solidi (a) **213**, 1610–1614 (2016).

[66] X. Ni, Q. Fan, R. Shimada, U. Özgür, and H. Morkoç, "Reduction of efficiency droop in InGaN light emitting diodes by coupled quantum wells", Applied Physics Letters **93**, 171113 (2008).

[67] C. G. Dunn and E. F. Kogh, "Comparison of dislocation densities of primary and secondary recrystallization grains of Si-Fe", Acta Metallurgica **5**, 548–554 (1957).

[68] S. Nakamura, M. Senoh, N. Iwasa, S.-i. Nagahama, T. Yamada, and T. Mukai, "Superbright Green InGaN Single-Quantum-Well-Structure Light-Emitting Diodes", Japanese Journal of Applied Physics **34**, L1332–L1335 (1995).

[69] N. Sharma, P. Thomas, D. Tricker, and C. Humphreys, "Chemical mapping and formation of V-defects in InGaN multiple quantum wells", Applied Physics Letters **77**, 1274–1276 (2000).

[70] A. Hangleiter, F. Hitzel, C. Netzel, D. Fuhrmann, U. Rossow, G. Ade, and P. Hinze, "Suppression of Nonradiative Recombination by V-Shaped Pits in GaInN / GaN Quantum Wells Produces a Large Increase in the Light Emission Efficiency", Physical Review Letters **95**, 127402 (2005).

[71] H. Zhao, G. Liu, R. A. Arif, and N. Tansu, "Current injection efficiency induced efficiency-droop in InGaN quantum well light-emitting diodes", Solid-State Electronics **54**, 1119–1124 (2010).

[72] N. Okada, H. Kashihara, K. Sugimoto, Y. Yamada, and K. Tadatomo, "Controlling potential barrier height by changing V-shaped pit size and the effect on optical and electrical

properties for InGaN/GaN based light-emitting diodes", Journal of Applied Physics **117**, 025708 (2015).

[73] N. Nanhui, W. Huaibing, L. Jianping, L. Naixin, X. Yanhui, H. Jun, D. Jun, and S. Guangdi, "Enhanced luminescence of InGaN/GaN multiple quantum wells by strain reduction", Solid-State Electronics **51**, 860–864 (2007).

[74] T. Li, Q. Y. Wei, A. M. Fischer, J. Y. Huang, Y. U. Huang, F. A. Ponce, J. P. Liu, Z. Lochner, J.-H. Ryou, and R. D. Dupuis, "The effect of InGaN underlayers on the electronic and optical properties of InGaN/GaN quantum wells", Applied Physics Letters **102**, 041115 (2013).

[75] B. Gil, O. Briot, and R.-L. Aulombard, "Valence-band physics and the optical properties of GaN epilayers grown onto sapphire with wurtzite symmetry", Physical Review B **52**, R17028 (1995).

[76] K. Lorenz, N. Franco, E. Alves, I. M. Watson, R. W. Martin, and K. P. O'Donnell, "Anomalous Ion Channeling in AlInN / GaN Bilayers: Determination of the Strain State", Physical Review Letters **97**, 085501 (2006).

[77] C. Haller, J.-F. Carlin, G. Jacopin, D. Martin, R. Butté, and N. Grandjean, "Burying non-radiative defects in InGaN underlayer to increase InGaN/GaN quantum well efficiency", Applied Physics Letters **111**, 262101 (2017).

[78] T. Kawashima, H. Yoshikawa, S. Adachi, S. Fuke, and K. Ohtsuka, "Optical properties of hexagonal GaN", Journal of Applied Physics **82**, 3528–3535 (1997).

[79] J. F. Muth, J. H. Lee, I. K. Shmagin, R. M. Kolbas, H. C. Casey, B. P. Keller, U. K. Mishra, and S. P. DenBaars, "Absorption coefficient, energy gap, exciton binding energy, and recombination lifetime of GaN obtained from transmission measurements", Applied Physics Letters **71**, 2572–2574 (1997).

[80] G. Rossbach, J. Levrat, G. Jacopin, M. Shahmohammadi, J.-F. Carlin, J.-D. Ganière, R. Butté, B. Deveaud, and N. Grandjean, "High-temperature Mott transition in wide-band-gap semiconductor quantum wells", Physical Review B **90**, 201308(R) (2014).

[81] V. Fiorentini, F. Bernardini, F. Della Sala, A. Di Carlo, and P. Lugli, "Effects of macroscopic polarization in III-V nitride multiple quantum wells", Physical Review B **60**, 8849–8858 (1999).

[82] M. Pristovsek, "Wavelength limits for InGaN quantum wells on GaN", Applied Physics Letters **102**, 242105 (2013).

[83] M. Dworzak, T. Stempel, A. Hoffmann, G. Franssen, S. Grzanka, T. Suski, R. Czernecki, M. Leszczynski, and I. Grzegory, "Luminescence Efficiency of InGaN/GaN Quantum Wells on Bulk GaN Substrate", Materials Research Society Symposium Proceeding **892**, 825 (2006).

[84] R. Butté, J.-F. Carlin, E. Feltin, M. Gonschorek, S. Nicolay, G. Christmann, D. Simeonov, A. Castiglia, J. Dorsaz, H. J. Buehlmann, S. Christopoulos, G. Baldassarri Höger von Högersthal, A. J. D. Grundy, M. Mosca, C. Pinquier, M. A. Py, F. Demangeot, J. Frandon, P. G. Lagoudakis, J. J. Baumberg, and N. Grandjean, "Current status of AlInN layers lattice-matched to GaN for photonics and electronics", Journal of Physics D: Applied Physics **40**, 6328–6344 (2007).

[85] M. Hiroki, Y. Oda, N. Watanabe, N. Maeda, H. Yokoyama, K. Kumakura, and H. Yamamoto, "Unintentional Ga incorporation in metalorganic vapor phase epitaxy of In-containing III-nitride semiconductors", Journal of Crystal Growth **382**, 36–40 (2013).

[86] E. Taylor, M. Smith, T. Sadler, K. Lorenz, H. Li, E. Alves, P. Parbrook, and R. Martin, "Structural and optical properties of Ga auto-incorporated InAlN epilayers", Journal of Crystal Growth **408**, 97–101 (2014).

[87] K. Ikeyama, Y. Kozuka, K. Matsui, S. Yoshida, T. Akagi, Y. Akatsuka, N. Koide, T. Takeuchi, S. Kamiyama, M. Iwaya, and I. Akasaki, "Room-temperature continuous-wave operation of GaN-based vertical-cavity surface-emitting lasers with n-type conducting AlInN/GaN distributed Bragg reflectors", Applied Physics Express **9**, 102101 (2016).

[88] G. Perillat-Merceroz, G. Cosendey, J.-F. Carlin, R. Butté, and N. Grandjean, "Intrinsic degradation mechanism of nearly lattice-matched InAlN layers grown on GaN substrates", Journal of Applied Physics **113**, 063506 (2013).

[89] K. Muraki, S. Fukatsu, Y. Shiraki, and R. Ito, "Surface segregation of In atoms during molecular beam epitaxy and its influence on the energy levels in InGaAs/GaAs quantum wells", Applied Physics Letters **61**, 557–559 (1992).

[90] N. A. Kaufmann, L. Lahourcade, B. Hourahine, D. Martin, and N. Grandjean, "Critical impact of Ehrlich–Schwöbel barrier on GaN surface morphology during homoepitaxial growth", Journal of Crystal Growth **433**, 36–42 (2016).

[91] M. S. Minsky, S. B. Fleischer, A. C. Abare, J. E. Bowers, E. L. Hu, S. Keller, and S. P. Denbaars, "Characterization of high-quality InGaN/GaN multiquantum wells with time-resolved photoluminescence", Applied Physics Letters **72**, 1066–1068 (1998).

[92] S. F. Chichibu, H. Marchand, M. S. Minsky, S. Keller, P. T. Fini, J. P. Ibbetson, S. B. Fleischer, J. S. Speck, J. E. Bowers, E. Hu, U. K. Mishra, S. P. DenBaars, T. Deguchi, T. Sota, and S. Nakamura, "Emission mechanisms of bulk GaN and InGaN quantum wells prepared by lateral epitaxial overgrowth", Applied Physics Letters **74**, 1460–1462 (1999).

[93] A. Armstrong, T. A. Henry, D. D. Koleske, M. H. Crawford, and S. R. Lee, "Quantitative and depth-resolved deep level defect distributions in InGaN/GaN light emitting diodes", Optics Express **20**, A812 (2012).

[94] S. Keller, S. B. Fleischer, S. F. Chichibu, J. E. Bowers, U. K. Mishra, and S. P. DenBaars, “Effect of the Confinement Layer Design on the Luminescence of InGaN/GaN Single Quantum Wells”, physica status solidi (b) **216**, 269–272 (1999).

[95] S. K. Shee, Y. Kwon, J. Lam, G. Gainer, G. Park, S. Hwang, B. Little, and J. Song, “MOCVD growth, stimulated emission and time-resolved PL studies of InGaN/(In)GaN MQWs: well and barrier thickness dependence”, Journal of Crystal Growth **221**, 373–377 (2000).

[96] E. C. Young, N. Grandjean, T. E. Mates, and J. S. Speck, “Calcium impurity as a source of non-radiative recombination in (In,Ga)N layers grown by molecular beam epitaxy”, Applied Physics Letters **109**, 212103 (2016).

[97] A. Saxler, D. Walker, P. Kung, X. Zhang, M. Razeghi, J. Solomon, W. C. Mitchel, and H. R. Vydyanath, “Comparison of trimethylgallium and triethylgallium for the growth of GaN”, Applied Physics Letters **71**, 3272–3274 (1997).

[98] N. Grandjean, J. Massies, F. Semond, S. Y. Karpov, and R. A. Talalaev, “GaN evaporation in molecular-beam epitaxy environment”, Applied Physics Letters **74**, 1854–1856 (1999).

[99] D. D. Koleske, A. E. Wickenden, R. L. Henry, J. C. Culbertson, and M. E. Twigg, “GaN decomposition in H_2 and N_2 at MOVPE temperatures and pressures”, Journal of Crystal Growth **223**, 466–483 (2001).

[100] M. Lannoo, Point defects in semiconductors I.Theoretical aspect, (Springer-Verlag, Berlin, 2012).

[101] J. Yang, D. G. Zhao, D. S. Jiang, P. Chen, Z. S. Liu, L. C. Le, X. J. Li, X. G. He, J. P. Liu, S. M. Zhang, H. Wang, J. J. Zhu, and H. Yang, “Investigation on the compensation effect of residual carbon impurities in low temperature grown Mg doped GaN films”, Journal of Applied Physics **115**, 163704 (2014).

[102] N. Okada, K. Tadatomo, K. Yamane, H. Mangyo, Y. Kobayashi, H. Ono, K. Ikenaga, Y. Yano, and K. Matsumoto, “Performance of InGaN/GaN light-emitting diodes grown using NH_3 with oxygen-containing impurities”, Japanese Journal of Applied Physics **53**, 081001 (2014).

[103] S.-N. Lee, H. S. Paek, J. K. Son, H. Kim, K. K. Kim, K. H. Ha, O. H. Nam, and Y. Park, “Effects of Mg dopant on the degradation of InGaN multiple quantum wells in AlInGaN-based light emitting devices”, Journal of Electroceramics **23**, 406–409 (2008).

[104] J.-X. Shen, D. Wickramaratne, C. E. Dreyer, A. Alkauskas, E. Young, J. S. Speck, and C. G. Van de Walle, “Calcium as a nonradiative recombination center in InGaN”, Applied Physics Express **10**, 021001 (2017).

[105] D. Wickramaratne, J.-X. Shen, C. E. Dreyer, M. Engel, M. Marsman, G. Kresse, S. Marcinkevičius, A. Alkauskas, and C. G. Van de Walle, “Iron as a source of efficient Shockley-Read-Hall recombination in GaN”, Applied Physics Letters **109**, 162107 (2016).

[106] S. Chichibu, T. Azuhata, T. Sota, and S. Nakamura, “Luminescences from localized states in InGaN epilayers”, Applied Physics Letters **70**, 2822–2824 (1997).

[107] S. Heikman, S. Keller, T. Mates, S. DenBaars, and U. Mishra, “Growth and characteristics of Fe-doped GaN”, Journal of Crystal Growth **248**, 513–517 (2003).

[108] Y. Tokuda, Y. Matsuoka, H. Ueda, O. Ishiguro, N. Soejima, and T. Kachi, “DLTS study of n-type GaN grown by MOCVD on GaN substrates”, Superlattices and Microstructures **40**, 268–273 (2006).

[109] M. S. Daw and D. L. Smith, “Vacancies near semiconductor surfaces”, Physical Review B **20**, 5150 (1979).

[110] C. G. Van de Walle and J. Neugebauer, “First-principles calculations for defects and impurities: Applications to III-nitrides”, Journal of Applied Physics **95**, 3851–3879 (2004).

[111] J. Neugebauer and C. G. Van de Walle, “Gallium vacancies and the yellow luminescence in GaN”, Applied Physics Letters **69**, 503–505 (1996).

[112] J. L. Lyons and C. G. Van de Walle, “Computationally predicted energies and properties of defects in GaN”, npj Computational Materials **3**, 12 (2017).

[113] M. Ilegems and H. Montgomery, “Electrical properties of n-type vapor-grown gallium nitride”, Journal of Physics and Chemistry of Solids **34**, 885–895 (1973).

[114] Z. Xie, Y. Sui, J. Buckeridge, C. R. A. Catlow, T. W. Keal, P. Sherwood, A. Walsh, M. R. Farrow, D. O. Scanlon, S. M. Woodley, and A. A. Sokol, “Donor and Acceptor Characteristics of Native Point Defects in GaN”, arXiv:1803.06273 [cond-mat] (2018), arXiv: 1803.06273.

[115] K. Rapcewicz, M. Buongiorno Nardelli, and J. Bernholc, “Theory of surface morphology of wurtzite GaN (0001) surfaces”, Physical Review B **56**, R12725–R12728 (1997).

[116] M. E. Bartram and J. R. Creighton, “GaN CVD Reactions: Hydrogen and Ammonia Decomposition and the Desorption of Gallium”, MRS Internet Journal of Nitride Semiconductor Research **4**, 369–374 (1999).

[117] S. Nakamura, Y. Harada, and M. Seno, “Novel metalorganic chemical vapor deposition system for GaN growth”, Applied Physics Letters **58**, 2021–2023 (1991).

[118] S. Limpijumnong and C. Van de Walle, “Diffusivity of native defects in GaN”, Physical Review B **69**, 035207 (2004).

[119] T. Obata, J.-i. Iwata, K. Shiraishi, and A. Oshiyama, “First principles studies on In-related nitride semiconductors”, Journal of Crystal Growth **311**, 2772–2775 (2009).

[120] T. V. Bezyazychnaya, D. M. Kabanau, V. V. Kabanov, Y. V. Lebiadok, A. G. Ryabtsev, G. I. Ryabtsev, V. M. Zelenkovskii, and S. K. Mehta, “Influence of vacancies on indium atom distribution in InGaAs and InGaN compounds”, Lithuanian Journal of Physics **55**, 10–16 (2015).

[121] A. Uedono, T. Watanabe, S. Kimura, Y. Zhang, M. Lozac'h, L. Sang, S. Ishibashi, N. Oshima, R. Suzuki, and M. Sumiya, "Vacancy-type defects in $\mathrm{In}_x\mathrm{Ga}_{1-x}\mathrm{N}$ grown on GaN templates probed using monoenergetic positron beams", Journal of Applied Physics **114**, 184504 (2013).

[122] S. F. Chichibu, A. Uedono, K. Kojima, H. Ikeda, K. Fujito, S. Takashima, M. Edo, K. Ueno, and S. Ishibashi, "The origins and properties of intrinsic nonradiative recombination centers in wide bandgap GaN and AlGaN", Journal of Applied Physics **123**, 161413 (2018).

[123] D. Koleske, S. Lee, M. Crawford, K. Cross, M. Coltrin, and J. Kempisty, "Connection between GaN and InGaN growth mechanisms and surface morphology", Journal of Crystal Growth **391**, 85–96 (2014).

[124] T. Matsuoka, "Calculation of unstable mixing region in wurtzite $\mathrm{In}_{1-x-y}\mathrm{Ga}_x\mathrm{Al}_y\mathrm{N}$", Applied Physics Letters **71**, 105–106 (1997).

[125] J.-F. Carlin and M. Ilegems, "High-quality AlInN for high index contrast Bragg mirrors lattice matched to GaN", Applied Physics Letters **83**, 668–670 (2003).

Camille Haller-Tardy

18.07.1989
Avenue Haldimand 95A
1400 Yverdon-Les-Bains
Tél : +4179 963 28 41
Mail : camille.haller@epfl.ch

Professional Experiences

Ecole polytechnique fédérale de Lausanne, Advanced semiconductors for photonics and electronics laboratory	PhD Student – Metal organic vapor phase epitaxy (MOVPE) growth, spectroscopy, LED characterization	December 2015 - Present
Alpes Lasers SA	Junior Scientist - Data analyses, laboratory work, laboratory management, reporting for customer	October 2014 – November 2015
	Master thesis - Simulation, design and measurement of widely tunable quantum cascade laser based on Vernier effect	February 2014 – September 2014
	Internship - Construction of an experimental set-up to test quantum cascade laser, Analyze of noise measurement with statistical tools	September 2014 – January 2014
Denstply Maillefer	Student Job - R&D Department : Stress test, Literature research, Solidworks	August 2012 – September 2012
Medos International	Student Job - Purchasing Department - entry and management of purchase orders on the JDE software, mailing	July 2010

Education

Master in Applied Physics	Ecole polytechnique fédérale de Lausanne	2012 - 2014
Bachelor in Physics	Ecole polytechnique fédérale de Lausanne	2008-2012
Maturité Gymnasiale in Biology – Chemistry	Lycée Denis de Rougemont, Neuchâtel	2005-2008

Skills

Languages – French (mother tongue), English (fluent)

Software – Solidworks, Microsoft Office, KiCAD, JD Edwards

Programming – Python, C++, Matlab, R, Latex, Labview

Main Publications

C. Haller, J.-F. Carlin, M. Mosca, M. D. Rossell, R. Erni, and N. Grandjean. *InAlN underlayer for near ultraviolet InGaN based light emitting diodes*, Appl. Phys. Express **12**, 034002 (2019)

C. Haller, J.-F. Carlin, G. Jacopin, W. Liu, D. Martin, R. Butté, and N. Grandjean. *GaN surface as the source of non-radiative defects in InGaN/GaN quantum wells*, Appl. Phys. Lett. **113**, 111106 (2018)

C. Haller, J.-F. Carlin, G. Jacopin, D. Martin, R. Butté, and N. Grandjean. *Burying non-radiative defects in InGaN underlayer to increase InGaN/GaN quantum well efficiency*, App. Phys. Lett. **111**, 262101 (2017)

M. Malinverni, **C. Tardy**, M. Rossetti, A. Castiglia, M. Duelk, C. Vélez, D. Martin and N. Grandjean. *InGaN laser diode with metal-free laser ridge using n+-GaN contact layers,* Appl. Phys. Express **9**, 6 (2016)

A. Bismuto, Y. Bidaux, **C. Tardy**, R. Terazzi, T. Gresch, J. Wolf, S. Blaser, A. Muller, and J. Faist. *Extended tuning of mid-ir quantum cascade lasers using integrated resistive heaters,* Opt. Express **20**, 29715 (2015)

Y. Bidaux, A. Bismuto, **C. Tardy**, R. Terazzi, T. Gresch, J. Wolf, S. Blaser, A. Muller, and J. Faist. *Extended and quasi-continuous tuning of quantum cascade lasers using superstructure gratings and integrated heaters,* Appl. Phys. Lett. **107**, 221108 (2015)

S. Schilt, L. Tombez, **C. Tardy**, A. Bismuto, S. Blaser, R. Maulini, R. Terazzi, M. Rochat and T. Südmeyer. *An experimental study of noise in mid-infrared quantum cascade lasers of different designs,* Appl. Phys. B **119**, 189 (2015)

Conferences

International Workshop on Nitride Semiconductors (IWN), Kanazawa, November 2018, Oral presentation, Late News, *InAlN underlayer for high-efficiency near UV LEDS*

International Workshop on Nitride Semiconductors (IWN), Kanazawa, November 2018, Poster presentation, *Efficiency of InGaN/GaN quantum wells: The role of indium atoms in the capture of point defects*

International Conference on Nitride Semiconductors (ICNS), Strasbourg, July 2017, Poster presentation, *The role of InGaN interlayer on InGaN/GaN quantum well efficiency*

Compound Semiconductor Workshop (CSW), Berlin, Mai 2017, *Oral presentation, Investigation of InGaN superlattices on the efficiency of InGaN/GaN quantum wells*

International Workshop on Nitride Semiconductors (IWN), Orlando, October 2016, Poster presentation, *Comparison of the Optical Confinement Between Standard and Lateral Top Contact Laser Diodes*

Miscellaneous Work Experience

Teaching assistant at EPFL - General Physics for bachelor student	February 2016 – Present
Students' representative in the teaching commission at EPFL	2009 – 2013
Secretary of *Les Irrotationnels* (Physics section association at EPFL)	2010 – 2012

Ce document a été imprimé au Centre d’impression EPFL,
imprimerie climatiquement neutre, certifiée myClimate.